UNIVERSITY of CALIFORNIA
Santa Barbara

Interplay of quantum confinement, electron-electron interactions, and terahertz radiation in InGaAs quantum posts and GaAs quantum wells

A dissertation submitted in partial satisfaction of the
requirements for the degree of

Doctor of Philosophy

in

Physics

by

Christopher Michael Morris

Committee in charge:

Professor Mark S. Sherwin, Chair
Professor Elizabeth Gwinn
Professor Leon Balents
Professor Pierre M. Petroff

September 2011

The dissertation of Christopher Michael Morris is approved:

Professor Elizabeth Gwinn

Professor Leon Balents

Professor Pierre M. Petroff

Professor Mark S. Sherwin, Chair

University of California, Santa Barbara

September 2011

Interplay of quantum confinement, electron-electron interactions, and terahertz radiation in InGaAs quantum posts and GaAs quantum wells

Acknowledgments

First, I would like to thank my advisor Mark Sherwin. He has been incredibly supportive and patient for the past six years, and he has been someone I have truly enjoyed working with. I would also like to thank Pierre Petroff, who I had the pleasure of working closely with on the quantum post project. Additionally, I would like to thank my other committee members, Leon Balents and Beth Gwinn, as well as Jim Allen who was on my advancement committee.

I have had the opportunity to work with some really great people in lab. To Dominik, thank you for all your support and for being such a great mentor. Thank you also to all the grad students and postdocs I worked with: Dan, Ben, Devin, Jannis, Wendy, Christian, Sangwoo, Cristo, Vinh, Ethan, Gernot, and all the others. I would like to thank Tuan, Jun, and Hyochul for their great quantum post sample growth, and Shawn Mack for his growth of the period doubling quantum well. The development of the quantum post samples took many hours at the MBE, and the project wouldn't have worked without them.

At Los Alamos, Rohit and Toni were great to work with as advisors. Jinho and Diyar, thank you for your late nights in the lab working on ultrafast quantum post spectroscopy. I would like to thank the staff in the clean room, ITST,

and the machine shop as well for their support. Also, I'd like to thank Dave and Jerry for keeping the FEL running and helping me out with it. Thank you especially to all my friends in physics and to everyone on the UCSB Triathlon team who have been such a great group of people to have around me for the last six years.

Finally, I would like to thank my parents, who have always been extremely supportive of my career in science, and without whom none of this would have been possible.

Curriculum Vitae

Christopher Michael Morris

Education

2011	Ph.D. in Physics, University of California, Santa Barbara
2009	M.A. in Physics, University of California, Santa Barbara
2005	B.S. in Engineering Physics, Cornell University

Publications

" Terahertz Ionization of Highly-Charged Quantum Posts in a Perforated Electron Gas" C. M. Morris, D. Stehr, H. C. Kim, T. A. Truong, C. Pryor, P. M. Petroff, M. S. Sherwin, *Submitted, 2010*

"High-performance fiber-laser-based terahertz spectrometer" D. Stehr, C. M. Morris, C. Schmidt, and M. S. Sherwin, Optics Letters **35**, 3799 (2010).

"Ultrafast carrier capture in InGaAs quantum posts" D. Stehr, C. M. Morris, D. Talbayev, M. Wagner, H. C. Kim, A. J. Taylor, H. Schneider, P. M. Petroff, and M. S. Sherwin, Applied Physics Letters **95**, 251105 (2009).

"Growth and optical properties of self-assembled InGaAs quantum posts" H.J. Krenner, C. Pryor, J. He, J.P. Zhang, Y. Wu, C.M. Morris, M.S. Sherwin, and P.M. Petroff, Physica E **40**, 1785 (2008).

"Growth, Structural, and Optical Properties of Self-Assembled (In,Ga)As Quantum Posts on GaAs" J. He, H. J. Krenner, C. Pryor, J. P. Zhang, Y. Wu, D. G. Allen, C. M. Morris, M. S. Sherwin, and P. M. Petroff, Nano Letters **7**, 802 (2007).

"Mechanical Properties of Thin GDP Shells Used as Cryogenic Direct Drive Targets at OMEGA" A. Nikroo, D. G. Czechowicz, K. C. Chen, M. Dicken, C. Morris, R. Andrews, A. Greenwood, and E. Castillo, Fusion Science and Technology **45**, 229 (2004).

Abstract

Interplay of quantum confinement, electron-electron interactions, and terahertz radiation in InGaAs quantum posts and GaAs quantum wells

by

Christopher Michael Morris

Electron-electron interactions in semiconductor heterostructures are typically much weaker than the quantized energy spacings between their states. For materials with unusually small level spacings in the terahertz frequency range, however, these Coulomb interaction energies become comparable and can result in unique effects. Here, several systems are investigated in which these interactions play a major role.

InGaAs quantum posts are nanostructures with terahertz conduction level spacings. They are approximately cylindrical in shape, with heights in the range of 10-60 nm and diameters of ~30 nm, and are embedded in an InGaAs quantum well of the same height. Here, the terahertz absorption of quantum posts is investigated when they contain their maximum allowable number of

electrons. At this point, strong Coulomb repulsion in the posts prevents further charging, and the surrounding well is charged. Theoretical calculations show that absorption in this state is due to the "ionization" of charge from electronic states in the quantum posts to states in the surrounding quantum well. This ionizing transition, which otherwise would occur in the mid-IR band, is shifted to terahertz frequencies only because of a strong modification of the effective band structure of the quantum post and quantum well when highly charged. Ionization of these artificial atoms surrounded by an electron gas has no known analogue in atomic physics.

The use of quantum posts for quantum cascade lasers is also investigated. Quantum posts are integrated as the active region in a single period cascade structure. The UCSB Free Electron Laser, an intense quasi-CW source of terahertz radiation, is used to induce a resonant photocurrent as a method of characterization of charge injection and extraction in these structures.

Additionally, ultrafast spectroscopic techniques are used to determine the carrier capture times of quantum posts. Dynamics of charge pumped directly into the posts is also investigated, resulting in time and pump wavelength dependent absorption behavior that show complex charge dynamics.

Finally, the response of asymmetric quantum wells to intense terahertz fields

is investigated, with a goal of finding a period-doubling bifurcation in the electromagnetic response. Period doubling is expected to occur in this system due to the strong Coulomb interaction of charge in the asymmetric well, which introduces nonlinearity into the equations of motion. Extensive simulations are performed to model the period doubling emission response, and an optimal well design is found. Experimental investigations of this effect in real samples are performed with the Free Electron Lasers at UCSB and in Dresden.

Contents

Chapter 1

Introduction and Basic Intersubband Physics

In condensed matter physics, the terahertz frequency range (for us 100 GHz - 10 THz) can provide a wealth of information about the complex processes that occur in many solid materials. A wide variety of techniques have been developed to probe solids in the terahertz range in an effort to understand the processes dictating their material properties. Here, we investigate the physics of several semiconductor heterostructures specially designed to have terahertz energy spacings.

One of the most interesting properties of heterostructures with terahertz energies is that the energy scales due to confinement and those due to Coulomb interactions between electrons are nearly identical. Effects that can usually be ignored for heterostructures with larger energy scales now dictate the behavior,

creating unique effects only possible in this energy range. In Chapters 2-4, the physics of quantum post nanostructures are investigated. Confinement of charge within these nanostructures alters their confining potential and produces a solid state analogue to the ionization of charge from atoms. Chapters 5 and 6 detail the search for experimental signatures of subharmonic emission possible in asymmetric quantum wells, a nonlinearity brought about entirely by the strong interaction of charge within the well.

1.1 Quantum wells

1.1.1 Basic physics

In a crystalline material with a regular potential, the wave functions can be written using the well known Bloch functions:

$$\psi_{nk}(\mathbf{r}) = e^{i\mathbf{k}\cdot\mathbf{r}} u_{nk}(\mathbf{r}) \tag{1.1}$$

The quantum number n denotes the energy band of the wave function. Energies of these bands differ from material to material due to the different potential energies of the atoms forming the crystal lattice. The differences in band energies between different materials make it possible to artificially

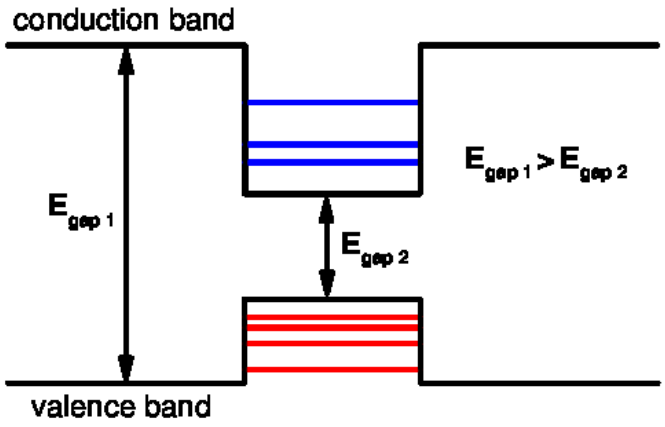

Figure 1.1: A simple picture of a quantum well potential energy with valence and conduction bands, formed by placing a low band gap material between two layers of higher band gap material. An example would be a layer of GaAs between two layers of AlGaAs.

engineer potentials by placing different materials next to each other. When a material with a low band gap is placed in a higher band gap material, the result is a confining potential for the charge existing in that band (Figure 1.1).

The simplest version of this is the infinite square well, familiar to anyone who has taken undergraduate level quantum mechanics. The band gap of the surrounding material is assumed to be infinite, impossible in a real material, but often an excellent approximation. Looking at a single band (within this

work, always the conduction band), for a well of width L, extending from $z = 0$ to $z = L$, the wave functions and energies take the form:

$$E_n = \frac{n^2 \hbar^2 \pi}{2m^* L^2} \tag{1.2}$$

$$\psi_n = \sqrt{\frac{2}{L}} \sin\left(\frac{n\pi z}{L}\right) \tag{1.3}$$

Of course, these are just the energies due to the confinement in the z-direction, and the freedom of charge to move in the x-y plane of the quantum well creates a continuous range of energies. If charge is then introduced to the well through doping, charge occupies these conduction subbands according to the density of states and the Fermi distribution function.

The density of states for a system with one confined and two free dimensions is given by the expression [1]:

$$N_{2D} = \frac{m}{\pi \hbar^2} \tag{1.4}$$

This two dimensional density of states is unique in that it is independent of energy. Of course, this is just the available states for electrons. The Fermi distribution function is then used to determine how electrons are distributed

in these states at a given temperature for a given Fermi energy.

$$f(E) = \left[\frac{1}{\exp\left(\left(E - E_F\right)/k_B T\right) + 1}\right] \tag{1.5}$$

In order to find the total electron density in a band, one then must integrate the density of states times the fractional filling of the states over all possible energies.

$$n_{2D} = \int_0^\infty N_{2D} f\left(E\right) dE = \int_0^\infty \frac{m}{\pi\hbar^2} \frac{1}{\exp\left(\left(E - E_F\right)/k_B T\right) + 1} dE \tag{1.6}$$

$$n_{2D} = \frac{m k_B T}{\pi\hbar^2} \ln\left(1 + \exp\left(E_F/k_B T\right)\right) \tag{1.7}$$

This expression for the densities in the occupied subbands is accurate even for wells with finite confining potentials.

For the wave functions and energies of real wells, many situations will require a more accurate solution of the energy eigenstates and wave functions. For a single particle, an analytic solution of the Schrodinger equation can still be obtained for a simple well with finite potentials. However, to calculate the wave functions and eigenenergies for more complicated wells with charge in them, numerical solutions must be used. To do this, an iterative approach is

used. First the Schrodinger equation is solved for the basic wave functions of the well containing no charge.

$$-\frac{\hbar^2}{2m^*}\frac{\partial^2}{\partial z^2}\psi_i\left(z\right)+V(z)\psi_i\left(z\right)=E_i\psi_i\left(z\right) \tag{1.8}$$

The wave functions are then used to calculate a new potential due to the distribution of charge within the well, using the Poisson equation:

$$\frac{\partial^2 V_{e-e}}{\partial z^2}=-\frac{4\pi e^2}{\epsilon}\sum_i N_i|\psi_i\left(z\right)|^2 \tag{1.9}$$

Where the total potential energy now consists of two terms:

$$V\left(z\right)=V_0\left(z\right)+V_{e-e}\left(z\right) \tag{1.10}$$

The first term V_0 describes the original potential energy due to the band structure of the well material, and V_{e-e} is the modification to the potential that the electrostatic forces of the electrons in the well produce. This numerical solution for the new charge distribution and resulting potential addition V_{e-e} gives a modified total potential, and the wave functions for this new potential must be solved using (1.8). An iterative process is run between the two equations until the solution for the potential and eigenstates/energies reaches

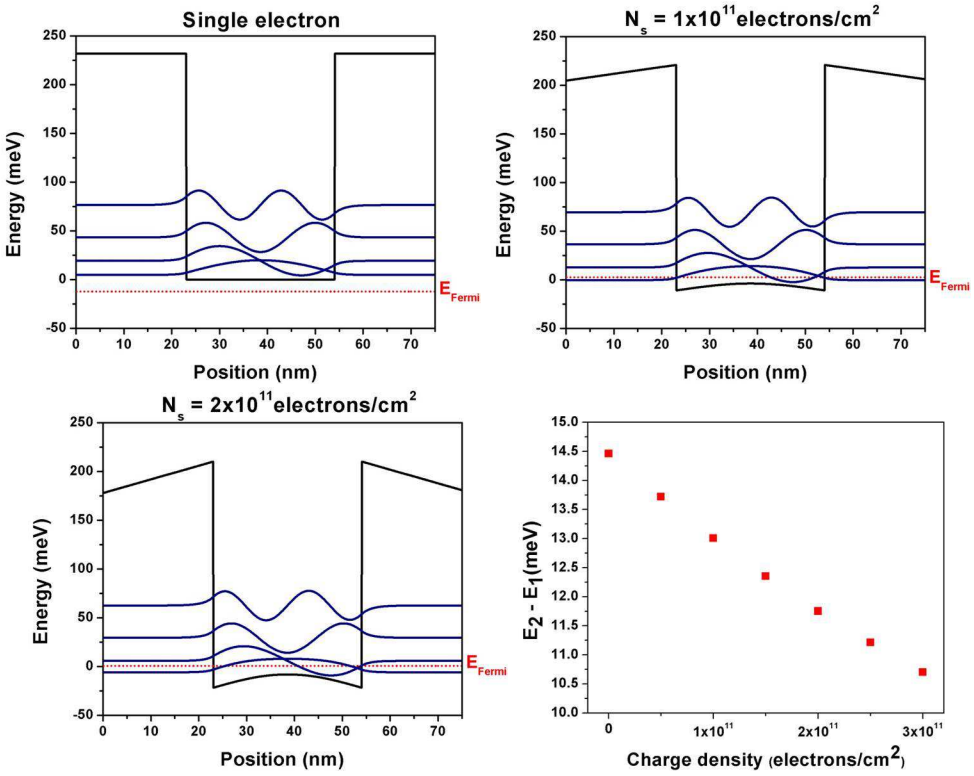

Figure 1.2: Wave functions and the well potential for increasing charge densities. As the charge is increased, the energy between the ground and first excited states decreases.

a steady state. The effect of increasing charge density in a well on both the wave functions and resulting energies is shown in Figure 1.2.

For a more complicated set of wave functions and energies such as those in Figure 1.2, the wave functions can still be split into complicated wave functions in the z direction, $\phi_n(z)$, and plane waves in the x-y directions, $e^{i\mathbf{k}\cdot\mathbf{r}}$. The energy of an electron in the n^{th} subband and with in-plane momentum $\mathbf{k}_\perp = (k_x, k_y)$

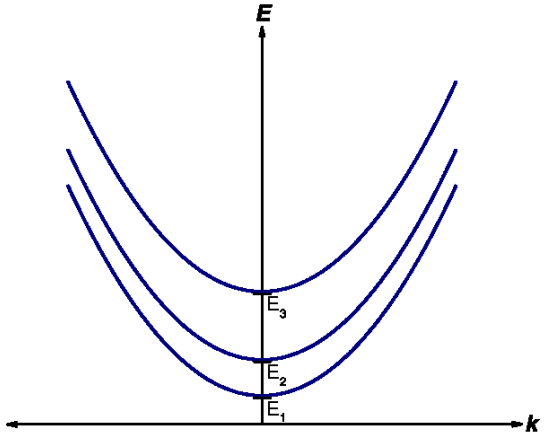

Figure 1.3: Quantum well subbands, with parabolic dispersion from the in-plane freedom of motion and energy levels from the z quantization.

is then given by:

$$E_{k_x,k_y,n} = \hbar(k_x^2 + k_y^2)/2m^* + E_n \tag{1.11}$$

with wave functions given by:

$$f_n = C\phi\,(z)\, e^{i\mathbf{k}\cdot\mathbf{r}} \tag{1.12}$$

where n denotes the subband, C is a constant to normalize the wave functions, and the subband energies E_n are found by solving (1.8) and (1.9). This gives a parabolic dispersion relation with bands as shown in Figure 1.3.

1.1.2 Intersubband absorption

In the single electron model, filled states of the quantum well will absorb light that is resonant with the energy spacing to the next excited state, causing a transition of an electron in a lower subband to an excited subband. To look more carefully at this transition, we can first look at Fermi's golden rule for the transition rate between two states, in the electric dipole approximation (the wavelength of light is much large than the extent of the states):

$$W_{if} = \frac{2\pi}{\hbar} \frac{e^2 E_0^2}{4m^{*2}\omega^2} \left|\langle i|\mathbf{e}\cdot\mathbf{p}|f\rangle\right|^2 \delta\left(E_f - E_i - \hbar\omega\right) \tag{1.13}$$

where E_0 is the electric field amplitude of the exciting wave, $|i\rangle$ and $|f\rangle$ are the initial and final state wave functions, $\mathbf{e}$ is the polarization vector of the electric field, E_f and E_i are the final and initial subband energies, and $\mathbf{p}$ is the quantum mechanical momentum operator.[2] Assuming the photon energy is resonant with the subband spacing ($E_f - E_i = \hbar\omega$), the main term determining for which state combinations absorption will occur is $\left|\langle i|\mathbf{e}\cdot\mathbf{p}|f\rangle\right|^2$. It has been shown that for quantum well systems, this expands into two terms,

$$\langle i|\mathbf{e}\cdot\mathbf{p}|f\rangle = \mathbf{e}\cdot\langle u_\nu|\,\mathbf{p}\,|u_{\nu'}\rangle\,\langle f_n|f_{n'}\rangle + \mathbf{e}\cdot\langle u_\nu|\,u_{\nu'}\rangle\,\langle f_n|\mathbf{p}|f_{n'}\rangle \tag{1.14}$$

related to the interband (conduction to valence) and intersubband (between states in the conduction band), with ν denoting bands, and n denoting subbands.

Writing the intersubband integral explicitly using (1.12) for the form of f_n, we get:

$$\langle f_n \left| \mathbf{e} \cdot \mathbf{p} \right| f_{n'} \rangle = C^2 \int d^3r \, e^{i\mathbf{k}_\perp \cdot \mathbf{r}} \phi_n^* (z) \, (\mathbf{e} \cdot \mathbf{p}) \, e^{i\mathbf{k}_\perp' \cdot \mathbf{r}} \phi_{n'} (z) \tag{1.15}$$

The x and y terms of $\mathbf{e} \cdot \mathbf{p} = \sum_j \hat{e_j} \left(-i\hbar \frac{\partial}{\partial x_j} \right)$ will both leave $\phi_{n'}$ undifferentiated , making its integral with the orthogonal ϕ_n zero (unless $n = n'$). In the case $n = n'$, a non-zero value for the integral is possible only if $\mathbf{k}_\perp = \mathbf{k}_\perp'$, since otherwise an oscillating exponential term $\exp\left(-i\left(\mathbf{k}_\perp - \mathbf{k}_\perp'\right) \cdot \mathbf{r}\right)$ is left, which will average to zero. This also means that even for the surviving z term, the initial and final $\mathbf{k}_\perp$ must be the same. Additionally, the fact that just the p_z term survives means that only radiation polarized along the growth direction will be able to produce an intersubband absorption, a selection rule important for the measurements carried out in this work.

1.1.3 Depolarization shift

While (1.8) and (1.9) give the correct intersubband energy spacing and wave functions, the observed intersubband absorption actually occurs at a higher frequency due to the depolarization shift. This is due to the fact that the actual absorption is a collective charge excitation, not a single electron excitation. Essentially, the charge in the well dynamically screens the effect of the infrared excitation field, which in turns shifts the absorption frequency. Allen *et. al.* [3] calculated this effect, and found that the shifted absorption energy is described by:

$$\tilde{E}_{12} = E_{12}\sqrt{1 + \alpha\frac{N_1 - N_2}{N_s}} \tag{1.16}$$

where N_1 and N_2 are the sheet charge densities in the first and second quantum well subbands, $N_s = N_1 + N_2$ is the total sheet charge density, $\tilde{E}_{12}$ (E_{12}) is the depolarization shifted (bare) intersubband frequency, and α is the depolarization parameter. This factor $\alpha = 8\pi e^2 N_s S_{1010}/\kappa\omega_{10}$, where S_{1010} is an integral over the wave functions, κ is the dielectric constant (~ 13 for GaAs), and ω_{10} is the bare intersubband frequency. The effect grows as the sheet density increases and is more pronounced for smaller ω_{10}. For mid-infrared

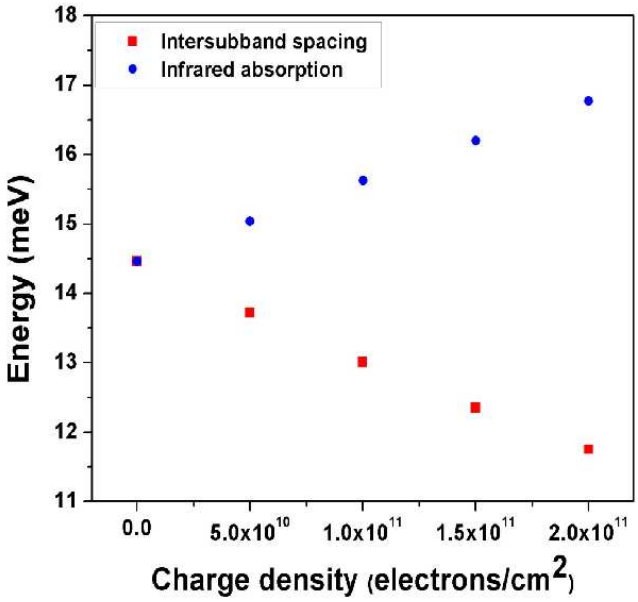

Figure 1.4: The depolarization shift for a 40 nm quantum well. It pushes the infrared absorption frequency higher in energy than the actual intersubband spacing.

quantum wells the effect is negligible, but in the terahertz the shift can become a large fraction of the intersubband energy and cannot be ignored.

The next logical step beyond the quantum well is the introduction of further confinement. Systems with two-confined dimensions are known as quantum wires, and introducing a third dimension of confinement produces a quantum dot.

1.2 Quantum dots

Quantum dots have excited considerable interest since their inception due to their ability to function as artificial atoms.[4] Unlike real atoms, their optoelectronic properties can be engineered through materials selection and geometry, allowing for production of dots with properties suited to their application. As in atoms, discrete energy levels are formed for confined carriers. However, due to their significantly increased size, their energy levels are usually much more closely spaced. Coulomb effects play a more important role in these structures as their dimensions grow larger and the Coulomb energy scales become a significant fraction of the intersublevel energy spacing. Considerable study has gone into the way in which electrons fill and interact in quantum dots, and their corresponding infrared and optical spectroscopic properties.[5, 6, 7, 8, 9]

The quantum dots studied here are based on InAs self-assembled quantum dots. Their growth process is detailed in Figure 1.5. Monolayers of InAs are successively grown on a GaAs substrate. Due to the lattice mismatch between InAs and GaAs (Indium is a bigger atom than Gallium), after a few monolayers it becomes energetically favorable for the InAs atoms to redistribute themselves to form small islands on the GaAs, quantum dots. These dots have a lower

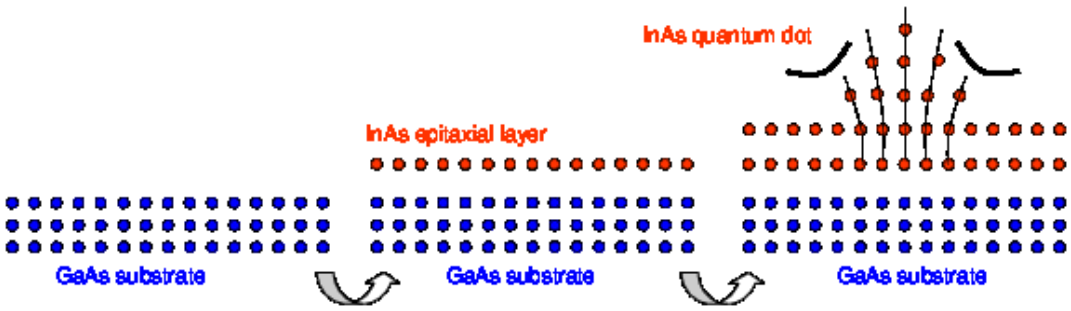

Figure 1.5: Growth process for InAs quantum dots.

band gap than the surrounding GaAs, and as for quantum wells they confine charge, but three dimensionally. They are roughly shaped like a pancake, with diameters of ~ 30 nm and heights of ~ 5 nm.

As in quantum wells, bound states for charge are formed in the quantum dots. The simplest model for a quantum dot is just a three dimensional version of the particle in a box. Assuming a rectangular box with sides L_x, L_y, L_z the energies and wave functions become:

$$E_{n_x,n_y,n_z} = \frac{\hbar^2\pi}{2m^*}\left(\frac{n_x^2}{L_x^2} + \frac{n_y^2}{L_y^2} + \frac{n_z^2}{L_z^2}\right) \tag{1.17}$$

$$\psi_{n_x,n_y,n_z} = \sqrt{\frac{8}{L_xL_yL_z}}\sin\left(\frac{n_x\pi x}{L_x}\right)\sin\left(\frac{n_y\pi y}{L_y}\right)\sin\left(\frac{n_z\pi z}{L_z}\right) \tag{1.18}$$

The largest dimension of the dot, L_x, L_y, or L_z determines the energy

spacing between the lowest two levels. This becomes important when making the transition to quantum posts. For quantum dots, the largest dimension is in the radial dimension, and the lowest energy states are controlled by this dimension. This radius is difficult to change outside of a narrow range, setting a limit on the size tunability of the lowest energy states. More complicated models of the energy states in quantum dots are used in practice, with most actual calculations of energies being done numerically, but they are beyond what is necessary here.

1.3 Quantum posts: a new nanostructure

The quantum post is a nanostructure based on quantum dots in the InGaAs materials system. Quantum posts are roughly cylindrical in shape and have diameters similar to quantum dots ($\sim$ 30 nm). While the heights of typical quantum dots are ~ 5 nm, quantum posts have been grown with heights of up to 60 nm. This height is controlled with nanometer precision during growth. If they are sufficiently tall, their lowest energy levels can be controlled directly by selection of their height [10, 11] rather than being defined by the radial confinement as in quantum dots, as (1.17) suggests.[12] This produces an energy

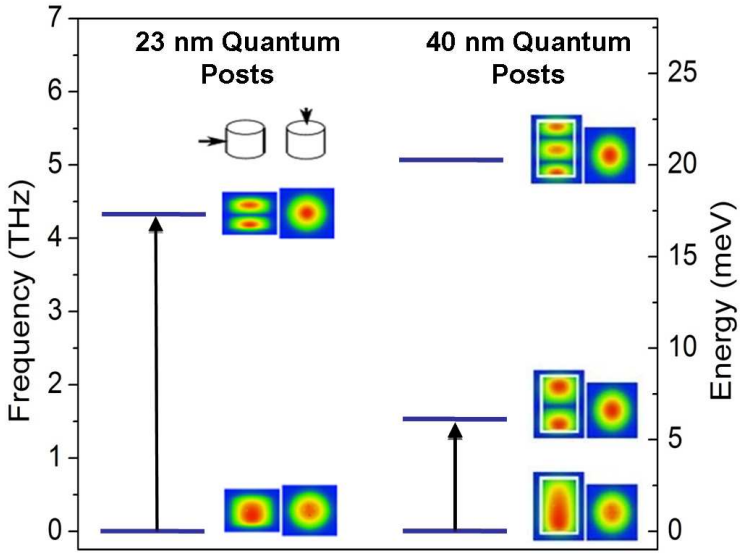

Figure 1.6: Calculated intersublevel spacings for quantum posts of two different heights. Taller quantum posts produce smaller level spacings. Calculations by Craig Pryor. [10]

level structure with spacings that are tunable from the MIR to FIR depending on the height of the post. Calculated energies for posts of two different heights are shown in Figure 1.6.

Their increased height also increases the buildup of Indium lattice mismatch strain, which significantly alters the energetic depth of quantum posts compared to dots. Quantum posts are offset from the GaAs conduction band edge by only 120 meV, shallower than dots of similar Indium content, which are offset by $\sim$ 300 meV.[13, 14, 15] A final important difference between the two is that the

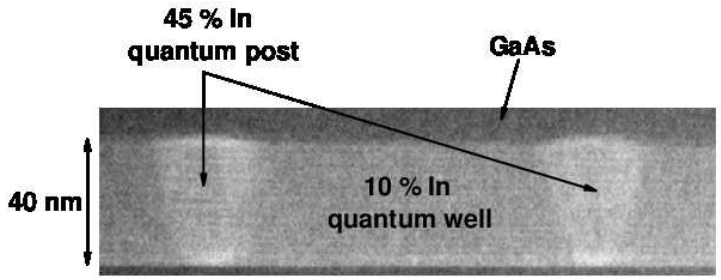

Figure 1.7: TEM image showing two quantum posts embedded in the 10% indium quantum well. [10]

quantum posts are embedded in an energetically shallower InGaAs quantum well matrix of the same physical height as the posts. This quantum well is similar to the wetting layer in quantum dots and is an unavoidable byproduct of the post growth process. Like the wetting layer it acts as a charge trap, but it is far thicker, and its spectral and charge transport properties are accordingly different.[16]

The growth of the quantum posts is essentially a repeated layer structure of quantum dots. A seed layer of InAs quantum dots is grown at a density of $1x10^{10}/cm^2$ to serve as nucleation centers for the post structures. After this, repetitions of 7 monolayers of GaAs and 1 monolayer of InAs are grown, with a 60 second wait time after each layer of GaAs or InAs. This wait time gives the system time to come to equilibrium. The GaAs layer moves away from the strain center at the dot, leaving its peak exposed, and the InAs layer

selectively moves onto the top of the now exposed dot layer, forming another quantum dot directly in contact with the first. This growth forms a fairly homogenous columnar structure after intermixing occurs during the growth. The heights of these structures are directly controlled via the number of repetitions of the GaAs/InAs layers. Energy dispersive x-ray analysis has been performed on posts, and it is found that after intermixing, the post composition is $In_{0.45}Ga_{0.55}As$, while the surrounding quantum well is $In_{0.1}Ga_{0.9}As$.

Chapter 2

Terahertz Absorption of InGaAs Quantum Posts

Here, an investigation of terahertz absorption due to electrons confined in quantum post and quantum well nanostructures is presented. The original goal of the project was to observe single electron transitions from ground to excited states in the conduction band of quantum posts. As mentioned in in Section 1.3, the three dimensional confinement of charge in the posts reduces the phase space available to electrons occupying their states. This should increase their lifetimes over their quantum well analogues, where confinement is only in a single direction, by reducing coupling to non-radiative decay mechanisms. A reduced coupling makes them attractive for possible incorporation as the active region of devices such as quantum cascade lasers. The first step was to determine the energy level structure of the posts, which had already been calculated

to be in the terahertz range for the heights available by MBE growth.

However, as the project evolved, it was found that controllably loading single electrons into the large number of posts necessary to observe terahertz transitions presented a number of problems. In the end, spectroscopic measurements of quantum post samples where electrons inhabit both the quantum posts and the surrounding quantum well were performed. While this was not the original goal of the project, the results proved to form a very interesting physical picture. In the interpretation of the absorption of the structures, single particle calculations were found to be insufficient to explain energy level structure of the quantum posts and the observed spectroscopic behavior. Full calculations with many interacting electrons were performed to predict the shift of the post energy levels due to the Coulomb blockade and to understand the electronic filling of the posts and surrounding quantum well. The energetically shallow nature of the posts and surrounding matrix quantum well means that both can be charged at the same time. Significant Coulomb interactions between electrons in the posts and electrons in the matrix quantum well play an important role in the electronic structure of the system. Consequently, the absorption measurements along with the energy level calculations led to a picture where the normal two dimensional electron gas present in the quantum well is

perforated by highly charged quantum posts that can locally alter the density of electrons in the well.[17, 18, 19]

Both the capacitance measurements and voltage dependent absorption measurements in Section 2.3 were taken at 10 K , close to the zero-temperature limit for these samples where the thermal energy (k_BT = 0.86 meV) is much less than the energy of the THz transitions being studied (3 THz = 12.9 meV)

2.1 Sample

The design used for the samples in the final experiments in this chapter was relatively simple, but the development to the final structure took several iterations. The sample design is modeled after samples used in experiments on conventional InAs quantum dots.[20] The basic design principle is to use a DC bias voltage to selectively fill successive energy levels in the quantum posts. This has previously been accomplished in quantum dots and studied extensively. However, in quantum posts this proved more difficult. Their more closely spaced energy levels and high level of inhomogeneous broadening proved to make it impossible to resolve electronic loading of individual energy levels within posts using the large sample pads necessary for the terahertz absorption

experiments.

The basic design in all versions of the sample uses a MISFET (Metal Insulator Semiconductor Field Effect Transistor) structure.[21] This is shown schematically in Figure 2.1. An insulating region containing the active region of the sample (in this section, a layer of quantum posts or a reference quantum well) is placed between a heavily doped back contact and an aluminum Schottky gate at the top. The heavily doped back gate pins the Fermi level in the conduction band. An AlGaAs barrier between the Schottky and back gates is added to reduce leakage current between the two contacts. A structure like this can be used as a transistor if two contacts are placed on opposite sides of the Schottky contact. The Schottky contact can then be used as a gate controlling current flowing between the two back contacts (source and drain). Here, the sample is processed such that a single back contact is used, so that current is not flowing in the back contact during measurements, there is merely a bias between the Schottky contact and the back gate. This causes the device to function as a diode. A bias can be applied between the back gate and the Schottky contact, simultaneously altering the electric field in the active region and modifying its charge density. This effect can be seen in Figure 2.2 for the final sample design.

As bias is applied, the actual change in voltage at the active region must be calculated by taking into account the built-in Schottky barrier and the effect of the lever arm. The Schottky voltage in our samples was ~ 0.7 V. This means that the effective voltage at the surface in Figure 2.1 is $V_{surface} = V_{Schottky} - V_{applied}$, where $V_{applied}$ is defined at the top contact relative to the back contact sitting as a ground. At the active region, the distance from the surface reduces the total change in voltage to $(t_{barrier}/t_{total})\, V_{surface}$, where the factor $(t_{barrier}/t_{total})$ is known as the lever arm. This lever arm is an important factor when analyzing the capacitance of the sample in Section 2.2.

In the design of the quantum posts, there were three main sample design iterations. In the first sample design, the structure from earlier works[20] with quantum dots was copied nearly exactly. This used a relatively short 25 nm tunneling barrier. However, absorption measurements using this design did not show any evidence of absorption from quantum posts. The electric field at which the posts load is determined directly by the distance $t_{barrier}$, and calculations[22] suggested that at this electric field the single electron transitions would in fact be Stark shifted out of the detection range of the absorption experiment.

To solve this problem, in the next sample iteration the tunneling barrier

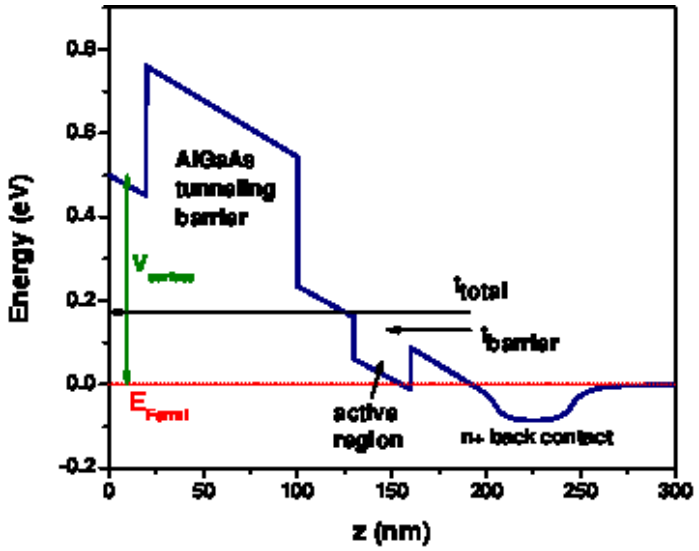

Figure 2.1: General conduction band structure of the MISFET samples.

distance was significantly increased to 45 nm. This flattens the bands significantly when the quantum posts begin to load with electrons. Additionally, the total thickness of the sample was increased to keep the lever arm approximately the same. However, the voltage at which the quantum posts loaded was now close to the forward bias breakdown voltage of the diode structure, which made the capacitance of the sample difficult to measure.

In the final sample design iteration, a delta-doped layer was added to the GaAs spacer between the active region and the AlGaAs barrier, to decrease the voltage at which the quantum posts began to load with electrons. This

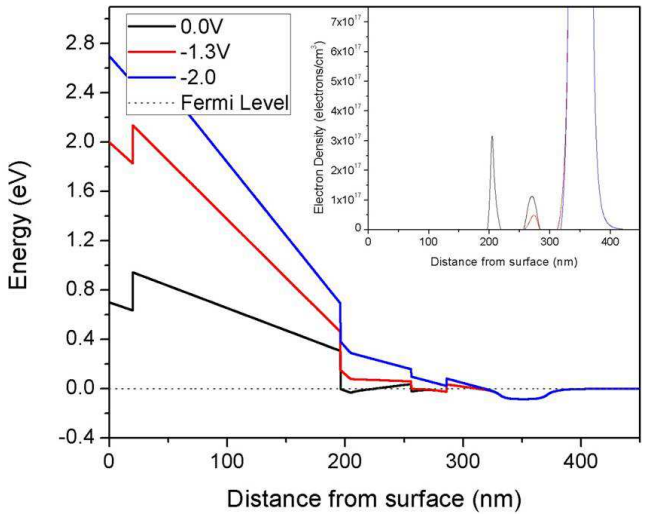

Figure 2.2: Sample band diagram at several voltages. The inset shows the associated charge densities as the active region, and then the modulation doped region fill with charge.

proved to give terahertz absorption that could be attributed to the quantum posts (Section 2.3). The sample band diagram is shown in Figure 2.2 for several bias voltages, along with the charge density. The final sample structure was as follows: A 40 nm heavily n-doped region ($2x10^{18}$electrons/cm^3) serves as the back gate for the structure. Next a 45 nm GaAs layer is grown, to act as a barrier between the n-doped layer and the quantum posts. The quantum posts are grown on top of this GaAs layer at a density of $1x10^{10}$/cm^2. For the final sample design, quantum posts with 12 dot repetitions were grown, resulting in a total post height of 30 nm. After the post layer is completed, a 60 nm GaAs

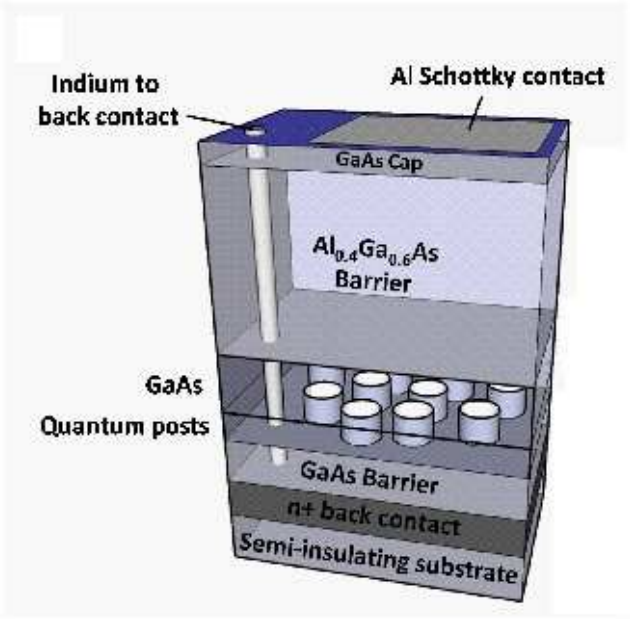

Figure 2.3: Schematic of the structure of the sample, showing the various layers. [17]

layer is deposited, followed by a 176 nm $Al_{0.4}Ga_{0.6}As$ barrier to reduce current across the sample, and a 20 nm capping GaAs layer. A delta doping layer ($6x10^{11}$electrons/cm^2) is placed in the 60 nm GaAs spacer, 50 nm from the active layer, to allow the active layer to fill before current is drawn across the sample. A 300 nm aluminum layer is evaporated on the surface of the sample, forming the Schottky gate. Indium metal is annealed to contact the back gate.

For the samples investigated here, only a single active layer containing quantum posts is grown. As Section 1.3 details, the quantum posts and surrounding

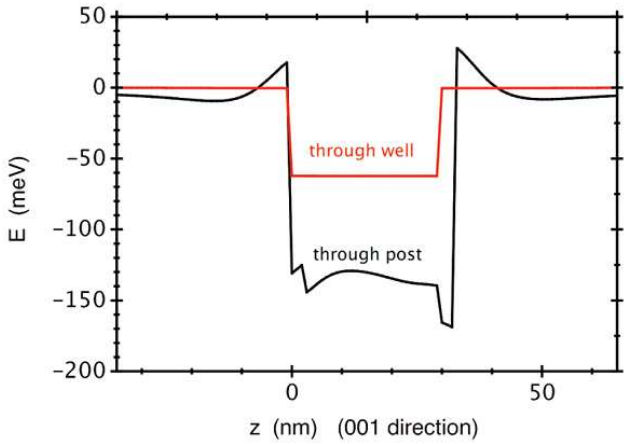

Figure 2.4: Band diagram in the z-direction for the quantum posts and quantum well. [17]

quantum well matrix are of approximately the same height. In the 30 nm tall quantum posts investigated here, the vertical confinement defines the smallest level spacing. Thus, the energy spacings between conduction subbands of the quantum well matrix are similar to the energy spacings between conduction-band levels arising from vertical confinement in the quantum posts. To distinguish between effects occurring in the quantum well and those occurring due to the presence of the quantum posts, we compare experimental results on a sample containing a layer of 30 nm high quantum posts with results from a reference sample that contains a 30 nm $In_{0.1}Ga_{0.9}As$ quantum well with no posts. The reference quantum well resembles the matrix of the quantum post sample.

2.2 Capacitance

Capacitance-voltage spectroscopy was used to measure the charging of the sample.[23] For a simple parallel plate capacitor, the capacitance is simply given by $C = \epsilon A/d$, where ϵ is the dielectric constant of the sample, A is the area of the capacitor plates, and d is the distance between the plates. For the samples studied here, there are most often large sheets of charge, so this model is very useful in understanding the capacitive behavior. Initially, before any charging of the active region of the structure, the capacitance between the heavily doped back gate and the aluminum front gate is measured. When charge tunnels into a structure closer to the back gate, the distance between the aluminum front gate and the closest charged layer decreases (reducing d), in turn increasing the capacitance. By monitoring the capacitance at different DC biases, charge moving from a back gate layer to another part of the sample structure can be detected, as illustrated in Figure 2.5.

2.2.1 Technique

To measure the capacitance, the sample is biased with a DC voltage and a small AC signal.

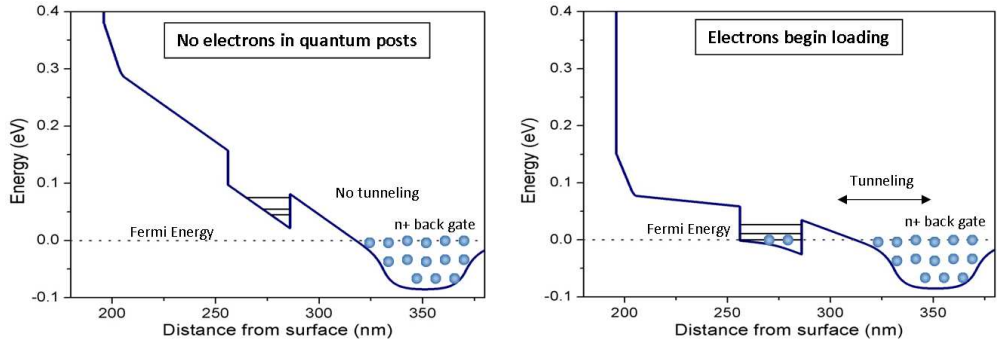

Figure 2.5: The sample before charging (left) and after charging (right). (Left) At large negative biases, the active region of the sample is above the Fermi level, and electrons cannot tunnel into the active region. The capacitance measured here is between the gate and the back contact. (Right) As the bias is increased, the energy of states in the active region become resonant with the Fermi level, and tunneling into the region occurs. This results in a corresponding increase in capacitance.

$$V_{Applied} = V_{DC} + V_{AC}\, cos\,(\omega t) \tag{2.1}$$

V_{DC} is used to tilt the band structure, modifying the electric field and charging of the active region, as shown in Figure 2.2. The small AC voltage is used to measure the capacitance at V_{DC}. The impedance of a capacitor in response to an AC voltage is given by $Z_{cap} = 1/i\omega C$. Using Ohm's Law, one can see that the AC current response will be directly related to the capacitance

$$I\,(\omega) = \frac{V\,(\omega)}{Z\,(\omega)} = V\,(\omega)\, i\omega C \tag{2.2}$$

The AC current response is thus used as a direct measurement of the sample capacitance. In practice, a DC voltage from a Keithley 2400 SourceMeter is added to a small AC voltage ($\sim$ 2 mV peak to peak) from the internal reference sine wave of an SRS 830 lock-in amplifier using a special isolating circuit. This combined voltage is then applied to the sample. The sample's current response to the AC voltage is sent to a transimpedance amplifier where it is converted to a voltage, which is then measured by the lock-in. The out-of-phase current response corresponds to the capacitance of the sample. In order to determine the magnitude of the capacitance measured, a reference capacitor placed within the isolating circuit is first measured, which accomplishes two things. First, it establishes the correct phase for the lock-in when measuring purely capacitive signals (including possible additions to the phase due to the internal amplification in the circuit). Second, it gives a measured signal magnitude for a known capacitance, which works as a calibration to determine the magnitude of the measured sample capacitance. This second feature is important when using the capacitance to determine to the charge in the sample.

Care must be taken when choosing the magnitude of this AC voltage. Its size directly determines the level of the signal response, as can be seen from (2.2). If there is a certain inherent level of noise in the measurement, choosing

a bigger AC amplitude can be used to improve signal to noise. However, the bigger the AC amplitude, the more of the capacitance curve that is sampled by the AC waveform, and the more the capacitive features are washed out. This means the amplitude of the AC voltage must be chosen to be smaller than the voltage resolution that is desired in the measurement. With the measurements presented here, the area of the gated area was large to improve the terahertz absorption, so the signal level was well above the noise even for small AC voltages, so the achievable voltage resolution was not a limiting factor in the measurements.

Once the capacitance has been measured, the charge can easily be determined, using

$$dQ = C\left(V\right) dV \rightarrow Q = \int C\left(V\right) dV \tag{2.3}$$

Most often, the relevant figure is the areal charge density, which is easily calculated since the size of the top contact is known. Specific examples are shown in the following section for the quantum post samples.

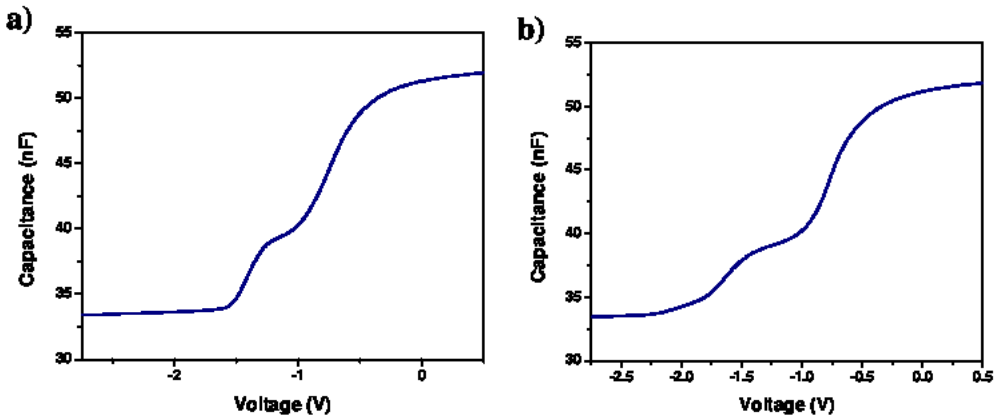

Figure 2.6: Capacitance of the quantum well (a) and quantum post sample (b).

2.2.2 Sample Capacitance and Interpretation

Figure 2.6 shows the capacitance spectra of the quantum well and quantum post samples. The two capacitance curves look similar, except for a small extra feature in the quantum post sample starting at -2.0 V. In order to understand the capacitive behavior of the two samples, simulations of the sample band structure and resulting capacitance were performed as a function of bias voltage. The simulations were performed using Greg Snider's one dimensional Schrödinger-Poisson solver.[24] The results of the quantum well sample simulation are shown in Figure 2.7. While the curves do not line up exactly, they serve the purpose of understanding the sample band structure as a function of voltage, and understanding what charging state the three main capacitive

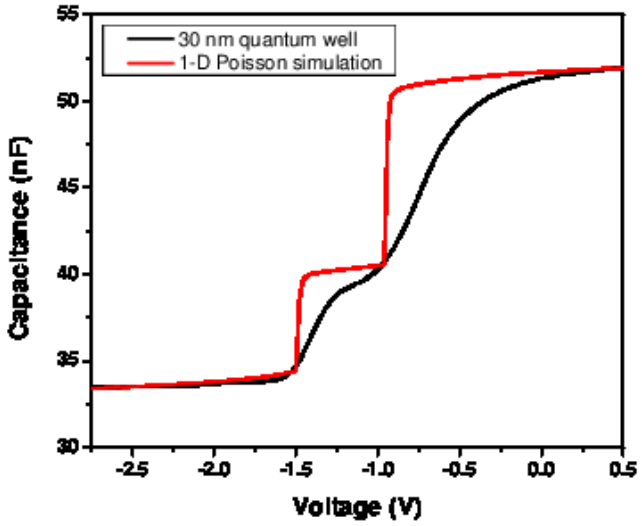

Figure 2.7: Modeling curve for the quantum well sample capacitance.

regions correspond to.

In the quantum well, below -1.5 V the conduction band of the active layer remains above the Fermi level, and the active region is uncharged. This corresponds to the blue curve in Figure 2.2. As the voltage is increased above -1.5 V, the lowest subband of the quantum well reaches the Fermi level, leading to the electronic filling of the quantum well. This increases the capacitance by reducing the distance between the front gate and the leading edge of the charge distribution. The band diagram for this state is shown in red in Figure 2.2. As the bias voltage is further increased above -0.75 V, the delta-doped region

of the sample reaches the Fermi level and begins to fill with electrons, causing another step-like increase in the capacitance, reflected in the black curve of Figure 2.2.

The capacitance spectrum of the quantum post sample (Figure 2.6b) is similar to that of the quantum well. The two rises found in the quantum well reference sample are present, again caused by electronic filling of the quantum well matrix and delta doped region. As mentioned above, at -2.0 V there is an additional capacitance increase associated with the onset of charging in the quantum posts. Due to their higher indium content, the posts are energetically deeper than the quantum well, and their bound states reach the Fermi level and begin to fill at lower voltages.

Integration of the capacitance curves was performed to determine the charge density in the quantum posts and quantum well. To determine the charge density in the quantum well reference sample, the capacitance was integrated as shown in Figure 2.8. The 1-D Poisson simulations showed that it is only in this voltage range that the well is charging. After, the charge density in the well stays essentially the same, and all the charge entering the sample goes to the modulation doped region. The total capacitance in this region must be used, as the charge layer in the quantum well covers the entire area of the

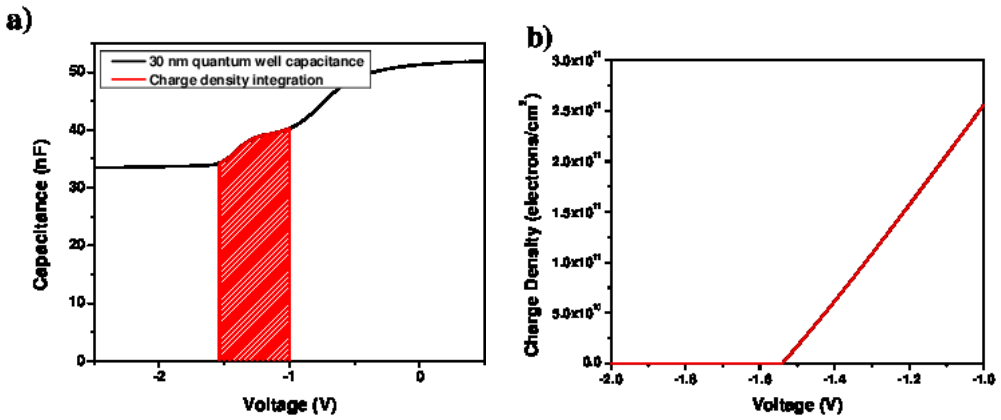

Figure 2.8: (a) Integration of the capacitance of the reference quantum well sample to obtain the charge density. (b) Extracted charge density in the well as a function of the applied bias.

sample under the front gate, essentially becoming the closest parallel plate in the capacitor.

Interpretation of the quantum post capacitance was slightly more complicated. Figure 2.9b shows the region that was integrated to obtain the charge in the well, the same as in the reference well. The region beginning at -2.0 V must be associated with charging of the posts directly, since it is absent in the reference well. In this region where only the posts have begun to fill with electrons, however, most of the capacitance of the sample is still due to the large background caused by the back gate. The quantum posts are just a small perturbation on top of this, and to take into account their capacitance, the

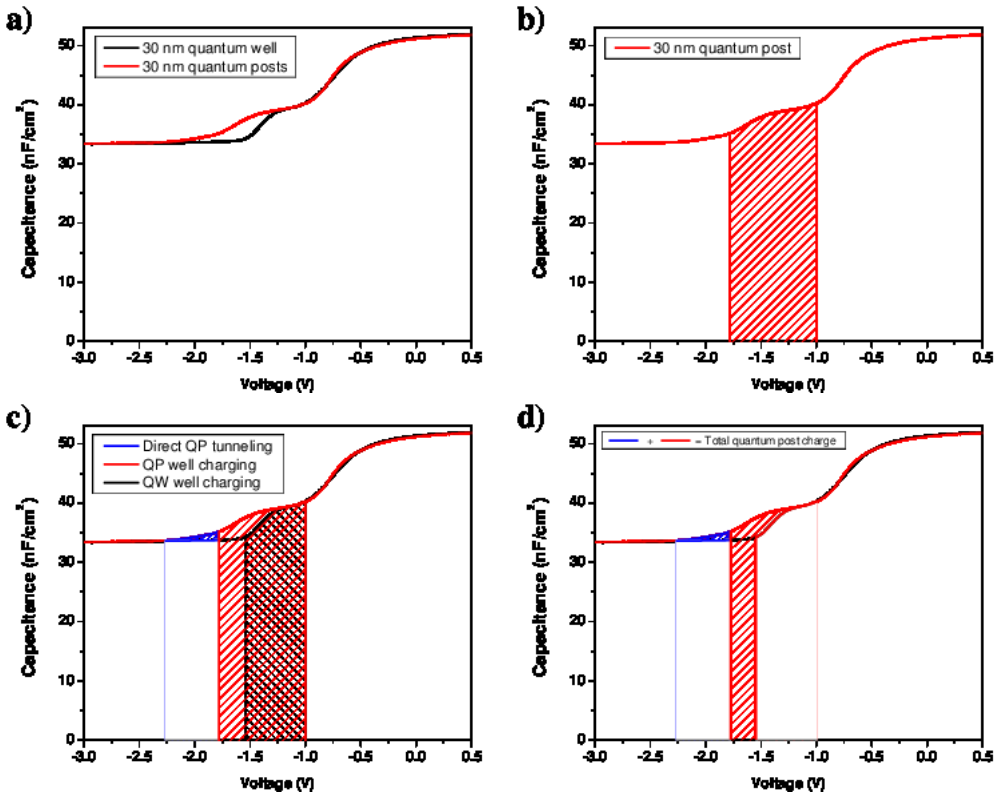

Figure 2.9: The charge integration process for the quantum post sample, described in the text.

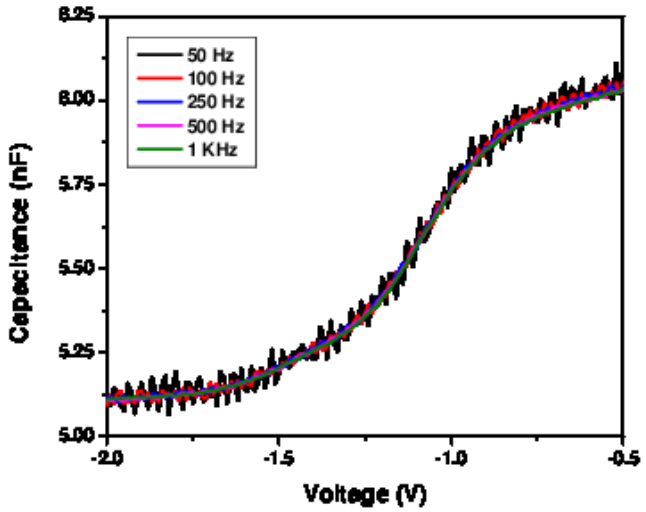

Figure 2.10: Frequency dependence of the direct tunneling region of the quantum post capacitance.

background must first be subtracted. However, integration of the capacitance in this region between -2.0 and -1.5 V reveals that the posts have only filled with 2.5×10^9electrons/cm^2, significantly less than their areal density. This indicates that direct tunneling across the barrier layer into the quantum posts is inefficient. Decreasing the frequency of the oscillating voltage in the CV measurement shows no increase in the electronic filling down to 50 Hz, indicating that the limiter to direct tunneling is coming from increased filling being energetically unfavorable at this voltage, not from the oscillating voltage being faster than the tunneling time constant (Figure 2.10) This behavior is not fully understood.

However, as the first subband in the well reaches the Fermi level, charge is able to efficiently transfer into the well. If the two curves from the quantum post and quantum well reference sample are overlaid, it can be seen that the quantum well region of the quantum post sample appears to be charging over a larger voltage range (Figure 2.9c). Energetically they should match each other, so the charge must be tunneling into the well, and then dropping into the posts in this region.[25] By subtracting the number of electrons in the quantum well of the reference sample from the number of electrons in the quantum well matrix of the post sample, the number of electrons in the posts can be extracted (Figure 2.9d). Comparison of the two capacitance curves shows that the post electron density is $6x10^{10}$electrons/cm^2, or 6 electrons per post by the time the modulation doped region begins to fill at -0.75 V.

2.3 Absorption

To investigate the terahertz electronic resonances of the quantum posts, the voltage and temperature dependent absorption spectra of the quantum well reference and the quantum post samples were compared. With the known electron distribution from the capacitance, these measurements can be used to

determine what is happening in the sample at different charge densities.

2.3.1 Experimental Setup

The terahertz absorption spectra were taken using Fourier transform infrared (FTIR) spectroscopy with a Bruker IFS66v FTIR. A mercury arc lamp is used as a broadband black body source of terahertz light. This is sent through a scanning arm Michelson interferometer and then through the sample. The transmitted light is detected by a 4.2 Kelvin Si composite bolometer. A square wave voltage at 250 Hz is applied to the sample, alternating the charge state of the active layer between -3.0 V (a voltage where no charge has tunneled into the posts or well) and the voltage being investigated. This modulates the absorption of the sample, which is detected by a lock-in amplifier. The scanning arm of the interferometer steps through its range and the resulting interferogram is Fourier-transformed to an absorption spectrum.

By locking-in to the modulated absorption a background-free measurement is obtained. Since the voltage is alternating between a charged and fully uncharged state in the structure, the absorption is directly measured, rather than the derivative of the absorption. Changing the high voltage of the square wave

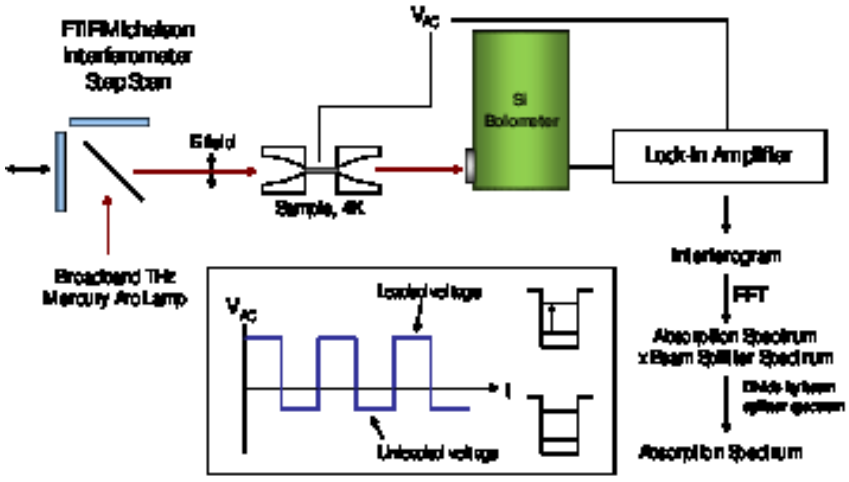

Figure 2.11: Experimental setup for the terahertz absorption of quantum posts.

for each scan gives the absorption as a function of voltage. To normalize out the frequency response of the spectrometer and detector, a reference transmission spectrum is taken at -3.0 V, a voltage where the active layer is depleted. Each modulated absorption spectrum is divided by this reference, to extract the true absorption of the sample. Experiments presented here always probe an ensemble of approximately $2.5 \text{x} 10^9$ posts.

2.3.2 Voltage Dependence

The absorption measurements in this section were all taken at 10 Kelvin. The absorption as a function of voltage for the quantum well reference and quantum post samples are shown in Figure 2.12, along with the associated capacitance curves.

When the quantum well reference sample (Figure 2.12a) begins to load at -1.5 V, a single absorption line appears near 5 THz. It is Stark shifted by the DC electric field to a frequency that is significantly higher than the bare intersubband frequency for the well. As the voltage is further increased, the DC electric field at the well decreases (Fig. 2.12a, inset), and the absorption red-shifts strongly as the magnitude of the DC Stark effect decreases. Self-consistent simulations including the dynamic electron-electron interaction in the random phase approximation[26] (depolarization shift) match these observed transition energies at the well electron density derived from the capacitance data ($\sim$ 2.4x10^{11} electrons/cm^2).[27] These simulations show that this corresponds to absorption from the lowest quantum well subband to the first excited subband. As the charge density in the well increases, a second peak is observed near 4.6 THz, starting near -0.25 V. Quantum mechanical selec-

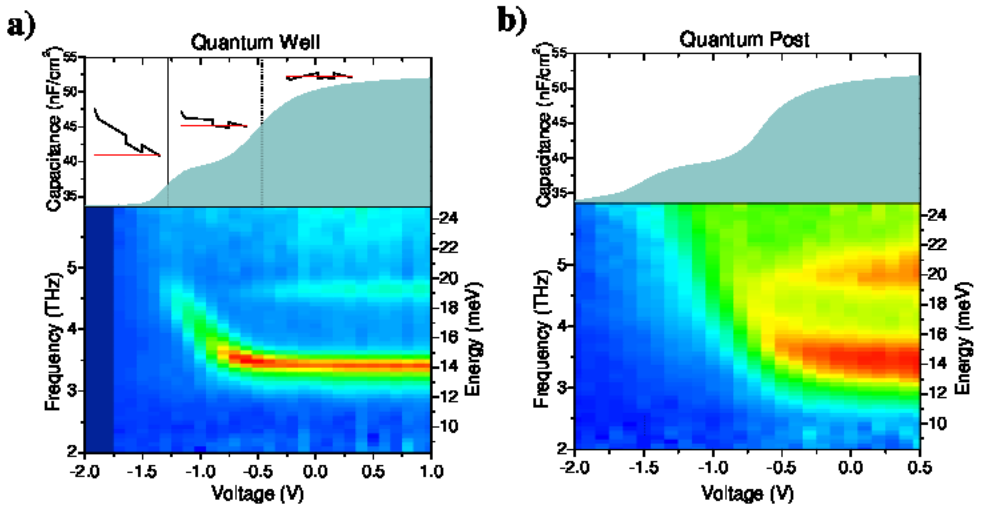

Figure 2.12: Voltage dependent absorption of the quantum posts and quantum well. (a) The quantum well shows two distinct absorption lines, associated with intersubband transitions from the ground to first excited state (14 meV line) and the first to second excited state (19 meV line). (b) In the quantum post sample, the same two absorption lines are present, but additionally there is a large background absorption, associated with a transition involving the quantum posts. [17]

tion rules forbid the ground to second excited state transition, and theoretical calculations predict the first to second excited state transition to occur at this frequency, and the second peak is associated with this transition.

Since the posts are energetically deeper than the well in the reference sample, they begin to load at -2 V rather than -1.5 V. The Stark shift at this voltage is so large that it pushes the frequency of the post transition above 6 THz, where phonon absorption makes the sample opaque to THz light. The

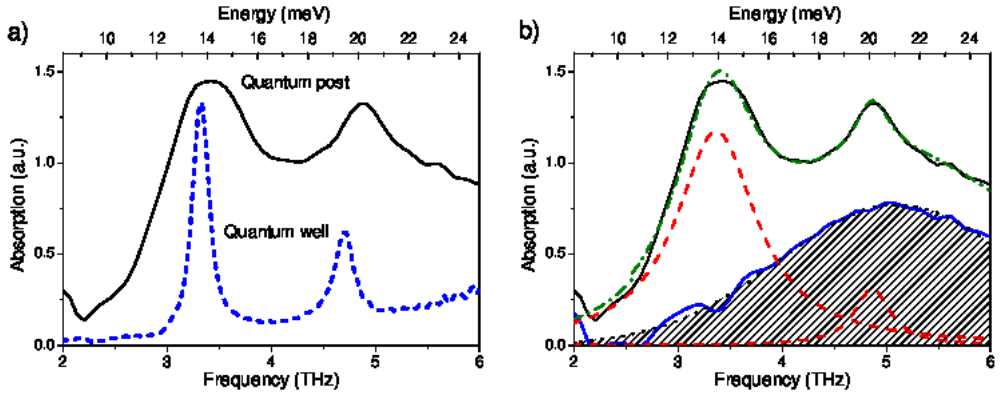

Figure 2.13: (a) Quantum post and quantum well absorption at 0.5 volts. (b) An additional underlying absorption is present in the quantum post sample, associated with an absorption involving the quantum posts. The black line is the original absorption, with the green dot-dash line being the total fit. The Lorentzian fits for the quantum well absorption are red dashed lines, and the fit for the quantum post absorption is shown in blue, with black has marks under it. [17]

features of the quantum post sample absorption seen in Figure 2.12b are similar to those in the quantum well reference sample. Two peaks are observed, corresponding to the same transitions in the quantum well region. However, it can be seen that there is a large additional background absorption in the quantum post sample that is not present in the quantum well reference.

Absorption spectra were investigated in detail at 0.5 V, when the charge in each active region is nearly independent of voltage and the quantum well and quantum posts are close to flat-band (zero electric field) conditions. The quantum well spectrum (Figure 2.13a) shows the two clear peaks at 14 and

19 meV discussed earlier, as well as a linear background absorption starting at 10 meV. The origin of the linear background absorption is unclear, although it may be associated with TO phonon absorption in InAs, or possibly weak bound to continuum absorption from a filled subband of the well. The absorption of the quantum post sample shows the two peaks characteristic of the quantum well reference sample, which are assigned to the quantum well matrix surrounding the posts. In addition, there is a large underlying absorption that is absent in the quantum well sample, which is assigned to transitions involving the posts. Figure 2.13b shows a deconvolution of the spectrum in which the two Lorentzian peaks due to the quantum well transitions and the linear background are subtracted. The remaining absorption is fit with a Gaussian line-shape, the expected absorption line-shape for a transition dominated by inhomogeneity as in quantum dots. The simplest assignment of the Gaussian line would be to single-electron transitions between sublevels of the quantum posts, which are at THz frequencies. However, the capacitance measurements in Section 2.2 show that the posts have accepted their maximum number of electrons and the well has started to fill. This leaves all intersublevel transitions within the posts Pauli-blocked. This leaves the question of the origin of the post absorption. To understand this, temperature dependent absorption

measurements were performed.

2.3.3 Temperature Dependence

To further investigate and clarify the origin of the quantum post related absorption, temperature dependent absorption measurements were performed on both samples. The post states are energetically deeper below the Fermi level than the well states, and as such should have a different temperature dependent filling fraction. Figures 2.14 (a) and (b) show the temperature dependent absorption of the quantum well and quantum post sample at a voltage of 0.5 V, where conduction band states in the posts are full, and both the first and second subbands of the quantum well have begun to fill. As in the voltage dependence, Lorentzian fits of the quantum well absorption and Gaussian fits of the quantum post absorption were performed at each temperature, and the transition strengths derived from the fits are plotted in the top panel of Figure 2.14. Self-consistent calculations were used to predict the quantum well absorption strengths based on the transition oscillator strengths and the electronic filling of the well, with the results shown as solid lines. As expected in the quantum well, the first subband quickly depopulates with increasing tem-

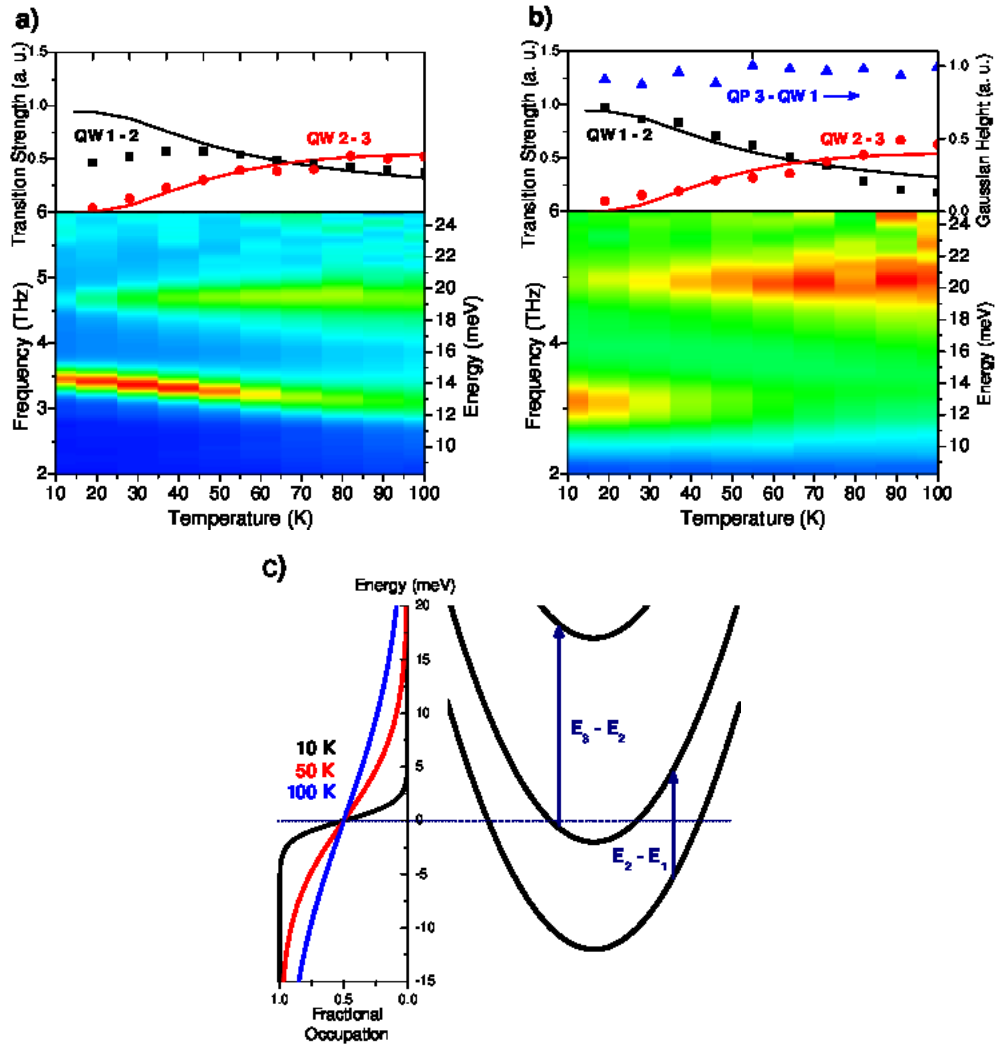

Figure 2.14: Temperature dependent absorption spectra of the reference quantum well (a) and quantum post (b) samples. In the top panels of each, fits of the Lorentzian quantum well absorptions and Gaussian quantum post absorptions are shown as dots, with the calculated strengths shown as solid lines. (c) Band structure of the quantum well energy levels, along with the temperature dependent filling fractions calculated according to the Fermi distribution and the constant density of states for a quantum well. [17]

perature, and a corresponding decrease in absorption is seen from the ground to first excited subband transition. The slight mismatch in the quantum well between the predicted and measured transition strength at low temperatures for the ground to first excited subband transition is not understood, but the good match at higher temperatures indicates that thermal depopulation of the states is occurring as would be expected based on the Fermi distribution. The population of the second subband increases with temperature, and correspondingly the absorption from the first to second excited subband gains strength. The underlying Gaussian transition is nearly unaffected by the temperature increase, consistent with an energy level that is deeper below the Fermi level than the quantum well subbands, implying the involved energy level must be in the posts.

Additionally, many-body effects (the depolarization shift) change as the temperature is increased in the quantum well sample. As the temperature increases, the population N_1 decreases while N_2 increases, which decreases the total factor shifting the transition energy in 1.16, thus decreasing the depolarization shift.[28] As the temperature increases in the quantum well sample, the ground to first excited state energy shifts towards its bare transition energy.

While the temperature dependent measurements have confirmed that the

transition is starting from a post level, which should not depopulate in the same way as a quantum well level, the exact transition occurring is still unclear. For this, theoretical calculations were performed by Craig Pryor at the University of Iowa.

2.3.4 A Perforated Electron Gas

To identify the involved states, eight band k·p calculations of the 30 nm quantum post bound states and their energies were performed as a function of the number of electrons in the posts.[29, 30, 31] As found experimentally from the capacitance, the calculations predict that the charging energy from the Coulomb blockade prevents more than 6 electrons from occupying each post. Although the quantum posts are physically much larger than quantum dots, the total charge they can hold is found to be similar because of their smaller band offset.

With 6 electrons in a post, the calculated strongest transition is from the filled third conduction band level to an unoccupied higher post level as shown in Figure 2.15. The associated transition energy is 20.5 meV, matching very well with the observed value of 21 meV found for the background Gaussian.

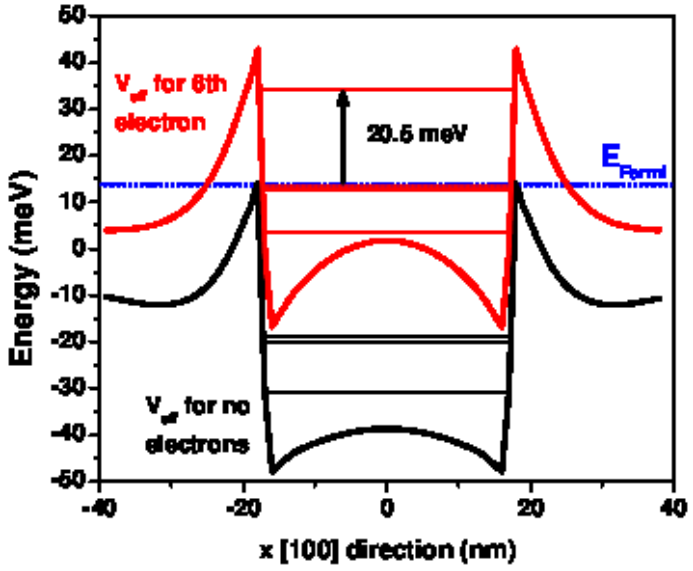

Figure 2.15: Theoretical calculation of the band structure in the x-y plane of the quantum well matrix, tracing through a post. As the post charges with electrons, the band structure is highly dependent on the electron number, as can be seen for the calculated states for 0 electrons and 6 electrons. The observed transition centered around 20.5 meV is shown. [17]

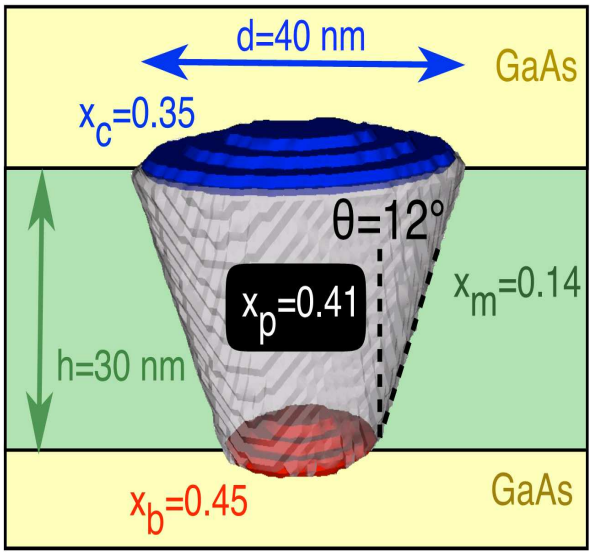

Figure 2.16: Nominal parameters used in the calculation of the post band structure. Parameters were determined by TEM and EDX, as well as photoluminescence measurements. The regions at the top and bottom of the post form small quantum dots with Indium content slightly different than the main structure of the post. In addition, the post slowly expands in diameter as it is grown higher. Also taken into account in the calculations is the slight ellipticity of the post, with the diameter in the (110) direction ~20% larger than the diameter in the (1-10) direction.

Electrons from the third level absorb a terahertz photon and transition to the excited state, then scatter into the lowest subband of the quantum well. This is reminiscent of the transition used in quantum dot infrared photodetectors (QDIPs) and quantum dot-in-a-well photodetectors (DWELLs), but with significantly reduced energies.[32, 33]

The inhomogeneity of the posts leads to the spread in transition energies

seen in the Gaussian in Figure 2.13. The post modeled in the calculations is the average post, but there is a variation in the size and shape of the posts as seen in quantum dots. This size variation also translates into different charging of posts which in turn additionally broadens the absorption line: posts with different numbers of electrons have energy levels that are modified differently by the charging energy from adding additional electrons. This charging energy effect works to spread the post energies out in addition to the broadening expected from variation in energy levels for posts of different sizes and shapes.

Additionally, the theoretical calculations show that the interpretation of the post states lying much deeper than the quantum well states is incorrect. The post state with the transition that we are observing is actually directly at the Fermi level. The charging energy (< 10 meV) is very close to the intersublevel spacing for the states in the post. Thus, the Fermi level is always quite close to the highest occupied post state. This is a unique situation that occurs as the post charges with additional electrons, and differentiates posts from dots due to their smaller energy level spacing.

A remaining question is how scattering from the highest filled state of the quantum post to the first quantum well subband is possible with the given electron distribution. Based on the capacitance and comparisons of the observed

quantum well energies and transition strengths with theoretical calculations, the well has an electronic sheet density of approximately $2x10^{11}/cm^2$ in the first subband, and $4x10^{10}/cm^2$ in the second subband. With the first subband of the well filled, scattering from the posts to these states should be blocked. However, calculations show that the quantum well matrix does not obey the ideal two dimensional parabolic dispersion relation everywhere. Far from the posts this is a good approximation, but near the posts electrons in the well feel a strong Coulomb repulsion from the six electrons in the posts. This pushes the local level for the well above the Fermi level, leaving open states for the quantum posts electrons to scatter into. The continuous electron gas normally found in a quantum well is perforated by these regions of strong Coulomb repulsion near the posts.

2.3.5 Future Directions

Previously, two dimensional electron gases have been perforated by "antidots." [34, 35] In antidot systems, the perforations in the electron gas are created by etching regular arrays of cylindrical holes near an electron gas, and thus depleting it by the surface field. In quantum post systems described here,

the perforations in the electron gas in the quantum well matrix have a very different origin—they emerge as a consequence of the Coulomb repulsion by the high concentration of electrons in each quantum post. The length scales in the post systems (spacing and radius of perforations) are also significantly smaller than those typically investigated in artificial antidot systems, which are limited by processing restrictions. Normal incidence spectroscopy of the quantum post perforated electron gas system did not reveal any associated resonances, as observed in antidot systems. However, the small size of the posts may push the associated resonances above the experimental frequency range presented here, and their random distribution may also inhomogeneously broaden it enough to push the signal below the noise floor of the experimental setup. Further experimental investigation and calculations beyond the effective medium theory normally used in the antidot systems could prove to be an interesting area of investigation in the quantum post perforated electron gas system.

The development of the quantum post materials system was initially motivated by the goal of creating nanostructures which resonate at terahertz frequencies, with potential applications including terahertz quantum cascade lasers based on a three-dimensionally-confined active region, improved terahertz detectors, and even quantum information processing. With further de-

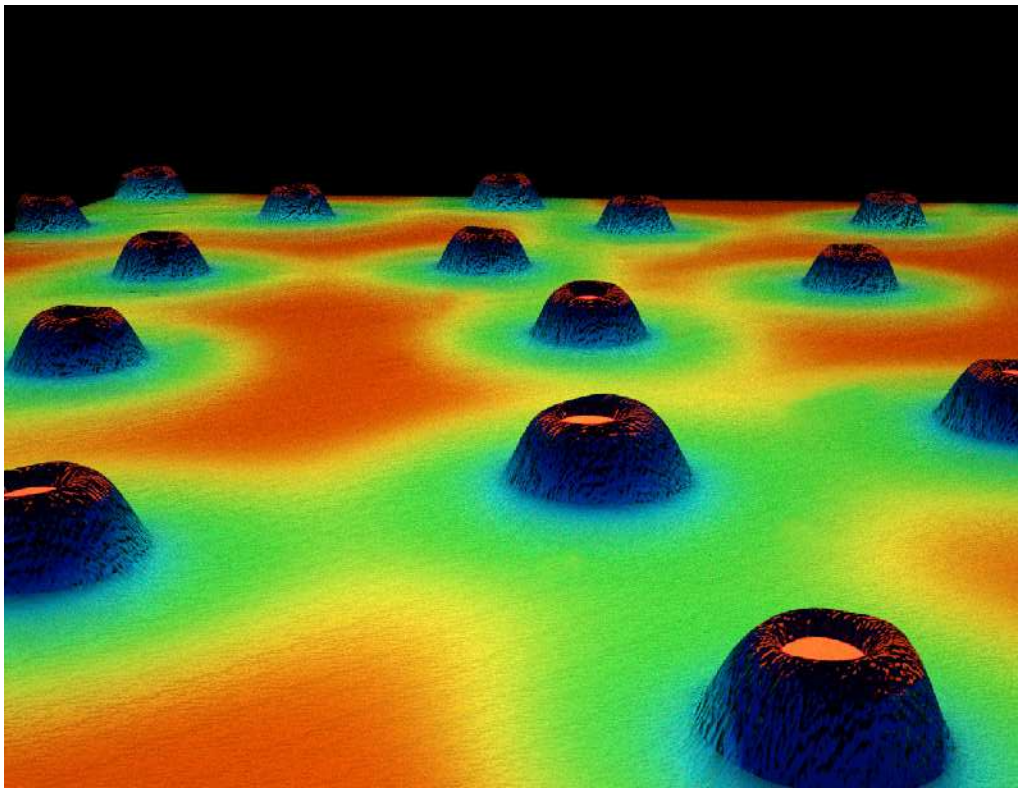

Figure 2.17: Artist's representation of the energy landscape of the quantum well two dimensional electron gas, perforated by the highly charged quantum posts. Higher electron density regions are represented by "hotter" red colors, lower electron density regions are represented with "cooler" blue colors.

velopment, these applications of quantum posts may come to fruition. Chapters 3 and 4 discuss further investigations of the terahertz properties of the quantum posts and their use in practical devices.

Chapter 3

Quantum Posts for Terahertz Quantum Cascade Lasers

3.1 Quantum Cascade Lasers

The first quantum cascade laser (QCL) was demonstrated in 1994 at Bell Labs, operating at mid-IR frequencies.[36] Although intersubband emission was first observed in the terahertz range by Helm *et. al.*,[37] it was seven years before a terahertz QCL was demonstrated by Kohler *et. al.* in Pisa, Italy at the Scuola Normale Superiore.[38] This proved difficult both because of difficulty selectively injecting/extracting charge from the closely spaced energy levels in the active region, and because getting good modal overlap with the active region in the resonant cavity proved difficult at longer wavelengths.[39]

3.1.1 Quantum cascade laser operating principle

Quantum cascade lasers are semiconductor heterostructure devices. They essentially consist of a set of carefully designed quantum wells, engineered to have intersubband transitions at the desired frequency. This set of quantum wells is then repeated, often hundreds of times in a row. Operation involves a single type of carrier traveling through the quantum wells, emitting photons when they pass through the intersubband transition. This is dissimilar to interband lasers such as diode lasers, which operate based on the recombination of electrons and holes across the semiconductor band gap. The carriers (usually electrons) travel entirely within a single band (the conduction band).

Figure 3.1a shows the basic operating principle of the QCL. This design is called the Wannier-Stark ladder, and is the type of structure in which intersubband emission was first observed. It consists of a single quantum well repeated over and over, specially designed to feed directly from the ground state of one well into the excited state of the next well in the cascade via resonant tunneling.

In reality, however, this design is impossible to make into a true laser. In order for a laser to work properly, a population inversion must be maintained. The Wannier-Stark ladder leaves the upper and lower laser states equally populated,

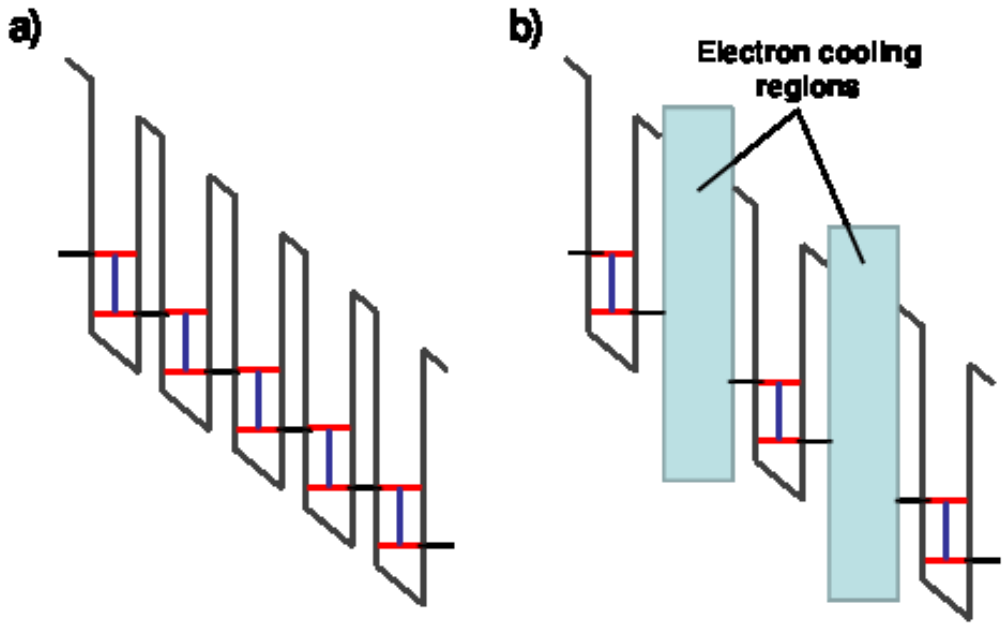

Figure 3.1: (a) The simplest design for a quantum cascade, called the Wannier-Stark ladder. A voltage is applied across the quantum wells, causing the drop in energy across the structure. Tunneling is denoted by black arrows, and radiative emission is denoted by dark blue arrows. This design is unable to maintain a population inversion due to equal tunneling forwards and backwards. (b) The basic design of modern quantum cascade lasers. After the radiative laser transition, a region that quickly depopulates the lower state, "cooling" the electrons and sending them into the upper laser state of the next cascade period.

since resonant tunneling is equally likely to occur forward as it is backward. In order to maintain a population inversion, a design like that shown in Figure 3.1b must be used. Specially regions are designed to clear the bottom laser level and prevent backwards tunneling, thus creating a population inversion. This type of structure is the basis for operation of all modern QCLs, although the details of the electron cooling regions can vary in different designs.

3.1.2 Temperature Dependent Performance

Since the first demonstration of a terahertz QCL, the technology has advanced rapidly, with improvements in design pushing laser operating temperature above 180 K in pulsed operation. One of the main goals of the research has been to push operating temperatures into the range of Peltier coolers ($\sim$ 240 K). This would allow QCLs to truly be THz lasers on a chip, without the need for bulky cryogenic cooling mechanisms. Higher temperature lasing (to ~220K at 3 THz) has been achieved by placing QCLs in high magnetic fields (up to 30 T, see Figure 3.2). This increases the quantization in the electron gas as Landau levels from and provide three dimensional confinement. However, outside of a research setting these fields are impractically large, and another method

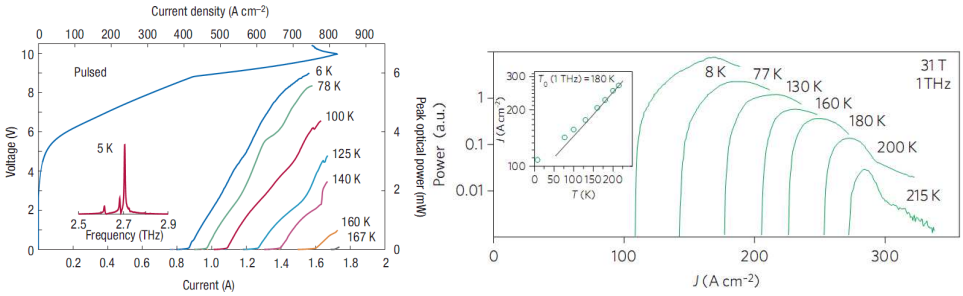

Figure 3.2: The temperature performance of terahertz quantum cascade lasers is improved by introduction of a perpendicular magnetic field, which introduces confinement. [40, 39]

of achieving this same beneficial confinement in a QCL structure is desirable.

Figure 3.3 demonstrates how increasing the degree of confinement improves the temperature performance. For a quantum well providing only one confinement dimension, the electrons can occupy a continuous band of energies, and as the temperature increases, the Fermi distribution widens and electrons occupy higher states in the upper laser band. Eventually, electrons significantly occupy states that are > 36 meV above the lower laser state, the LO phonon energy in GaAs. This makes non-radiative phonon emission a major pathway to move to the lower laser state. This becomes extremely detrimental to operation at higher temperatures. Making a fully three dimensionally confined structure, however, reduces the density of states to delta functions in energy. As the temperature is increased, even though electrons can occupy higher states, if

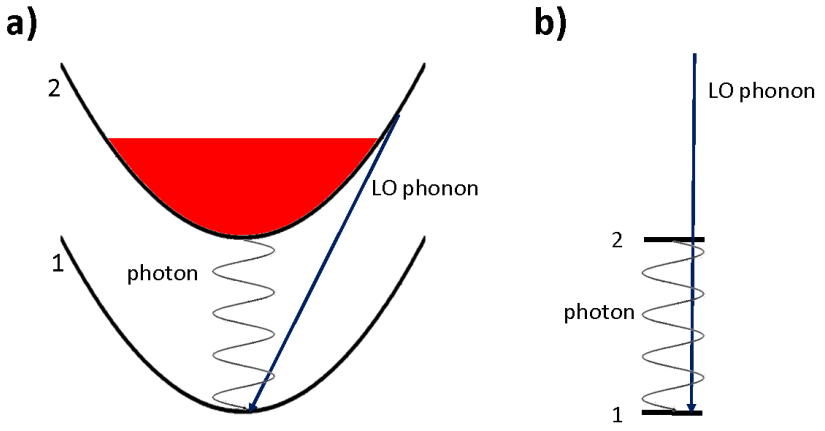

Figure 3.3: a) Parabolic dispersion in a quantum well allows non-radiative transitions via LO phonon emission to become the dominant mechanism for moving to the lower laser state at high temperatures. b) For a fully confined system, the laser states are not resonant with the LO phonon energy, and this decay mechanism is blocked.

the laser state is not resonant with the LO phonon energy, it should not be susceptible to the same non-radiative decay channel as the quantum well.

3.2 Quantum Posts in Cascade Structures

In this chapter, the first steps have been taken to incorporate quantum posts as the active region of a quantum cascade laser structure. Posts act as efficient charge traps because of their lower band gap, and their three dimensional confinement is ideal for the improved temperature performance discussed in the previous section. However, their relatively large conduction band offsets makes

incorporating posts into the cascade structure complicated, because selectively injecting and extracting charge from these structures is difficult. Strain causes the nucleation of quantum posts, so growing a well with high enough indium content to be resonant with post levels while at the same time not introducing quantum dot nucleation or strain dislocations is difficult. The main goal was to design and test a cascade structure that could efficiently inject and extract electrons from the posts.

To test the injection/extraction of charge from the posts, a resonant photocurrent measurement was designed based on stimulated emission of electrons in quantum posts. In normal operation of a quantum cascade laser, current is injected into the active region, and the resulting transport of electrons through the energy level structure results in the emission of light. The structure is designed so that the excited state of the laser transition has the longest lifetime, leading to a population inversion.

For the resonant photocurrent experiment, the process is run in reverse. The active region is biased as in normal operation, so that current is running through the structure. However, the active region is not placed in a resonant cavity, so the device never reaches threshold. An intense source of THz radiation (the UCSB free electron laser) with pulse duration of a few microseconds is then

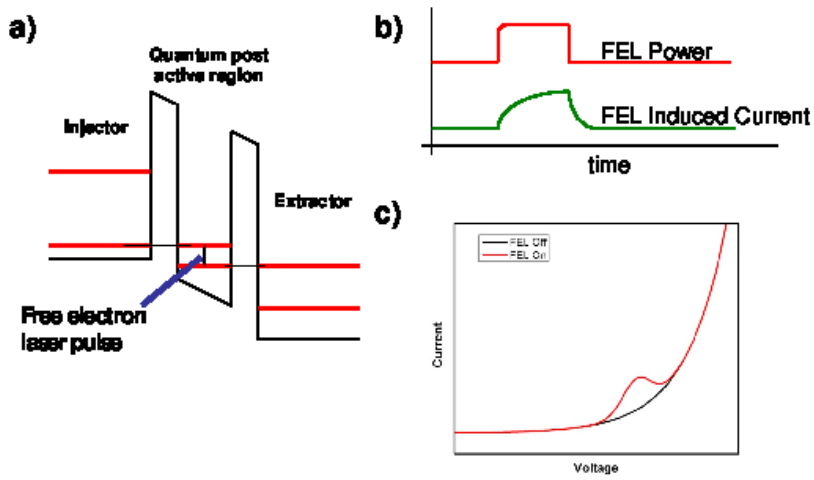

Figure 3.4: The basic operation of the resonant photocurrent experiment. (a) Resonant driving fields induce stimulated emission, increasing the current during the FEL pulse (b). This should result in a different IV curve when the FEL is on and off.

focused onto the active region. When the free electron laser (FEL) frequency is resonant with the laser transition, the lifetime of this transition decreases as the FEL induces stimulated emission. This is observed as a corresponding increase in current during the FEL pulse as charge moves through the cascade structure more quickly.

The experiment took place in two stages. First, the experiment was performed on a working quantum well cascade laser with many periods, as a test of the experimental principle. Second, the experiment was run on the quantum post cascade structures. To simplify the experiment, a single layer of quantum

posts (or a single quantum well for a reference sample) was grown. In current state of the art quantum post growth, no more than a few layers have been attempted. A single layer ensured that any effects of strain buildup or post inhomogeneity between layers would not alter the results of the experiment.

3.2.1 Active Region Design: Direct vs. Indirect

The first design difficulty was injecting charge into the quantum posts. As discussed in the previous section, their states are energetically deep, and growing an InGaAs quantum well layer to match this is difficult because of strain buildup. Instead, it was realized that the results of the capacitance from Chapter 2 demonstrate that the quantum well layer is easier than the posts to charge and is also an excellent way to transfer charge into the posts. The injector quantum well was therefore designed to inject charge into the matrix quantum well of the quantum posts.

In the design of the quantum post cascade structure, the original goal was to use a direct intersublevel transition in the post as the laser transition. The energy of this transition can be engineered during the growth by selection of the height of the posts. However, the lifetime of the first excited state is not

experimentally measured, and is most likely significantly shorter than the time it takes for electrons in the ground state to tunnel into the first extraction quantum well. This would mean that maintaining the population inversion necessary for a laser would be impossible.

Instead an indirect transition design was chosen, similar to the operating design of some conventional (quantum well based) QCLs. The rapid electron decay into the ground state of the post is used as an advantage in this design. The electron decays to the ground state, and the laser transition is then the spatially indirect transition from the post ground state to the lowest band of the first extraction quantum well, as shown in Figure 3.5. The lifetime of this transition should be quite long, both because of its indirect nature and because tunneling from a 0-D to 2-D state is a slow process.

Even though the terahertz transition within the post is no longer being used, it is still advantageous to use posts over dots, since the quantum well matrix is a much easier structure to inject into than the quantum dot wetting layer.[41, 42] In addition, although there is now a quantum well state in the laser transition, the advantage of decreased coupling to LO phonons at higher temperatures is not lost. The upper laser state is a level in the post, whose discrete density of states will not allow electrons to increase their energy continuously and become

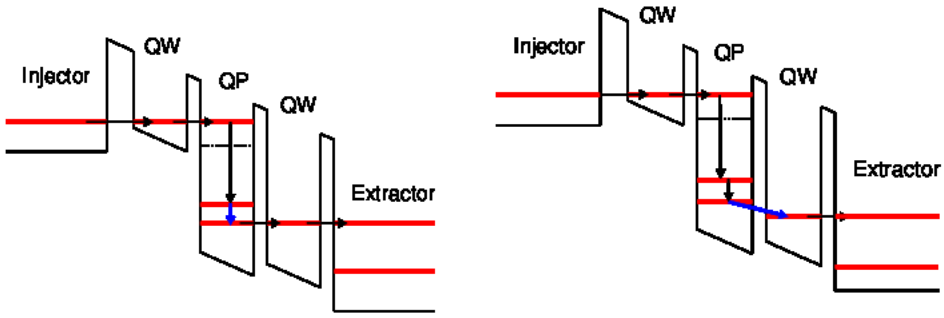

Figure 3.5: Direct (left) and indirect (right) design for the quantum post cascade structure.

resonant with optical phonon energies as the temperature increases.

To confirm that the relative lifetimes of the direct and indirect transitions favor the indirect design, calculations of the transition radiative lifetimes were performed by Craig Pryor.[22] Figure 3.6 shows calculations of lifetimes for the direct lasing scheme with quantum post excited to ground state transitions, as well as the indirect lasing scheme with quantum post ground state to extractor ground state transitions. The calculated times are purely radiative lifetimes, which is of course not practical in a real structure. In the real structure, coupling to phonons can significantly reduce lifetimes. However, the reduction in lifetimes should scale approximately equally for each scheme, so the relative lifetimes for each are still comparable. For the direct scheme, ΔE, the rela-

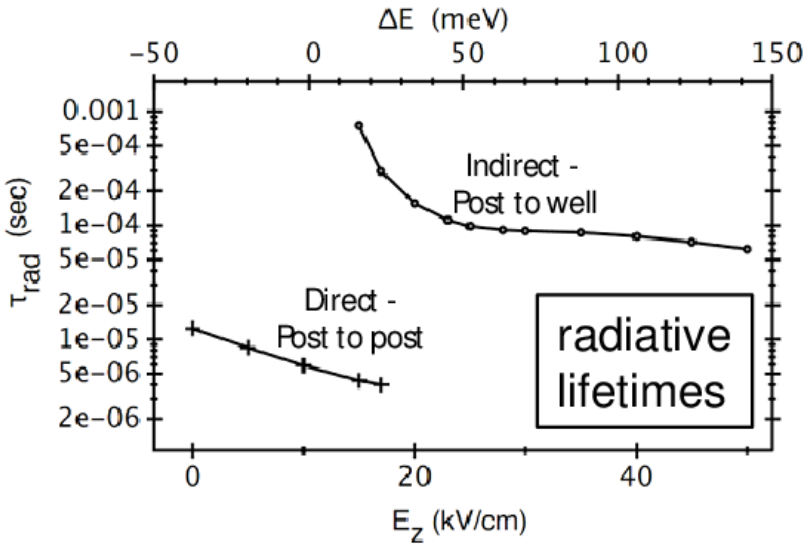

Figure 3.6: Radiative lifetimes for direct and indirect transitions in the single period quantum post cascade. [22]

tive energy difference between the quantum post ground state and extractor ground state, needs to be zero so that electrons can resonantly tunnel out of the quantum post. At this applied bias the lifetime is $6\text{x}10^{-6}$ seconds and the intra-post laser transition energy is 25 meV (energy not shown). For the same laser transition energy in the indirect scheme, one can see that the lifetime for a 25 meV transition is $3\text{x}10^{-4}$ seconds, nearly two orders of magnitude greater than the direct scheme. This shows that the lifetime of the indirect transition is much more favorable for maintaining population inversion. Additionally, the quantum post to extractor transition is the depopulation mechanism for the

direct scheme and at zero energy difference between the quantum post and extractor the lifetimes are very large, over 10^{-3} seconds. This means that population inversion would be impossible to achieve using the direct transition with an indirect laser transition depopulation mechanism.

3.2.2 Resonant Photocurrent Experiment

3.2.2.1 Samples

For the initial experiments on the quantum well based QCL, a working quantum cascade laser operating at 3.25 THz was used, grown and characterized by the QCL group in Vienna. This was based on the surface plasmon waveguide, where a heavily doped layer near the substrate of the sample acts as the bottom terahertz waveguide layer. The surface plasmon design is used rather than the more common metal-metal waveguide design so that light can be coupled into the QCL through the substrate.

For the quantum post single cascade samples, the design shown in Figure 3.7 was used. The layer structure was as follows: on a semi-insulating GaAs substrate, a highly doped n-type GaAs layer (bottom contact) was deposited. This layer was followed by four InGaAs extractor quantum wells, separated by

AlGaAs barriers. The indium concentrations in these four wells were 15%, 20%, 25% and 25% respectively. The indium content in these wells had to be carefully considered, as growing InGaAs layers with high levels of indium quickly causes buildup of strain, eventually resulting in nucleation of quantum dots.[7] A single layer of 30 nm quantum posts (30 nm quantum well in the reference sample) was then grown to serve as the active region. Two $In_{0.1}Ga_{0.9}As$ injector quantum wells separated by AlGaAs/GaAs barriers were grown directly on top of the quantum posts to serve as the injector layers. Finally a layer of highly doped n-type GaAs was deposited to make the top contact layer.

3.2.2.2 Experimental Setup

Both the quantum well and quantum post samples were processed with mesas containing the active region with an ohmic contact on top and an ohmic back contact. This back contact was well removed from the active region to avoid any possible antenna-like effects from the FEL being incident on both contacts at once. The experimental geometry of the sample is shown in Figure 3.8. The facets of the samples were polished at an angle of 15 degrees to increase the THz coupling to the active region. Samples were mounted to a chip carrier with one side removed to couple in the THz light, then the contact

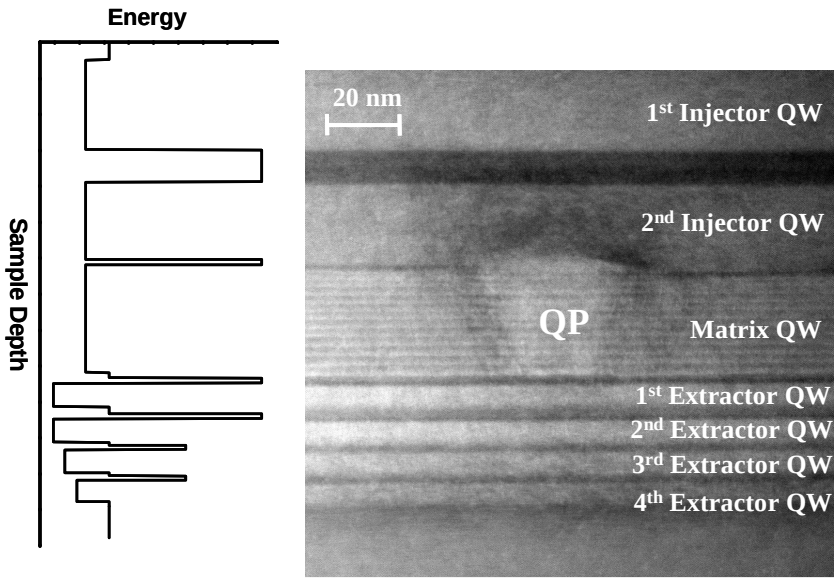

Figure 3.7: Band structure and TEM for the single period quantum post cascade structure.

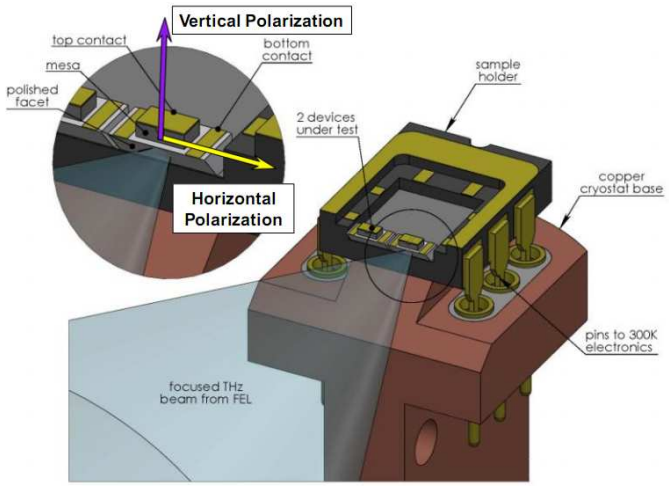

Figure 3.8: The chip carrier with sample mounted for the resonant photocurrent experiment.

pads were wire bonded. The chip carrier was then mounted inside a sample-in-vapor helium flow cryostat and temperatures were maintained at 10K. The sample-in-vapor cryostat was chosen for its large cooling power, as the currents that must be run through the samples are on the order of milliamps and cause significant heating.

Terahertz radiation was provided by the UCSB Free Electron Lasers (FELs): pulsed, narrowband radiation sources tunable between 0.1 and 4 THz, emitting pulses with durations of several microseconds. A small portion of the beam was split off to measure the power of individual pulses with a pyroelectric detector, and the remaining THz power was focused onto the facet of the samples using an

off-axis parabolic mirror (Figure 3.9). The photocurrent response of the system was obtained by measuring the voltage across a resistor of known resistance in series with the sample. Voltage across the resistor was amplified by a voltage pre-amplifier and then measured by an oscilloscope during the FEL pulse. The voltage measured from the test resistor for each FEL pulse was divided by the pyroelectric signal in order to normalize out pulse to pulse fluctuations in THz power. A DC voltage was applied with a Keithley source meter and the photocurrent response was recorded as a function of applied bias. The polarization and power of the THz radiation was controlled by a successive pair of wire grid polarizers.

3.2.3 Experimental Results

3.2.3.1 Quantum cascade laser

The first system investigated was the sample of a quantum well based QCL (multiple cascades) known to produce radiation at 3.25 THz. An increase in the photocurrent at high voltages (>15V) for frequencies near 3.25 THz would be expected as the system moves through the electric field where the proper level alignment of the radiative transition occurs. The system was investigated at a

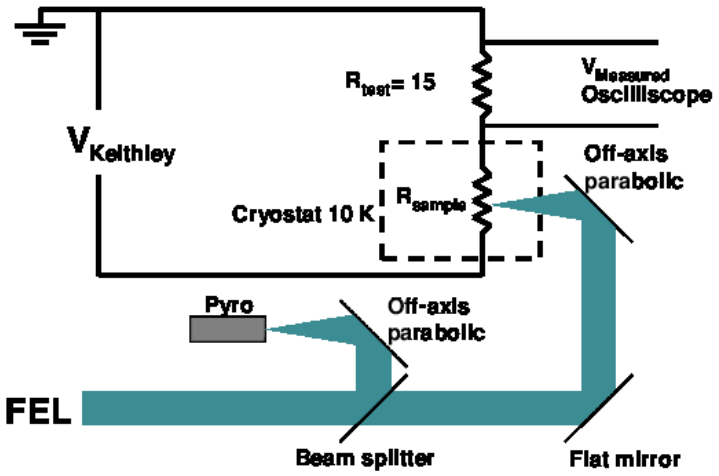

Figure 3.9: The experimental setup for the resonant photocurrent experiment. Photocurrent is monitored via a voltage across a test resistor in series with the sample.

number of different powers for a driving frequency of 3.3 THz (Figure 3.10b). It was found that an overall increase in current occurs for higher THz powers, but this effect is most likely due to increased heating of the carriers and not an effect associated with stimulated emission. Investigation of this sample at different THz frequencies shows similar behavior is present, as is seen in Figure 3.10 a, and strengthens the argument that this is an effect which is caused by heating.

The photocurrent response of this sample at a number of different THz frequencies (Figure 3.11) showed similar response: a large peak at low voltages

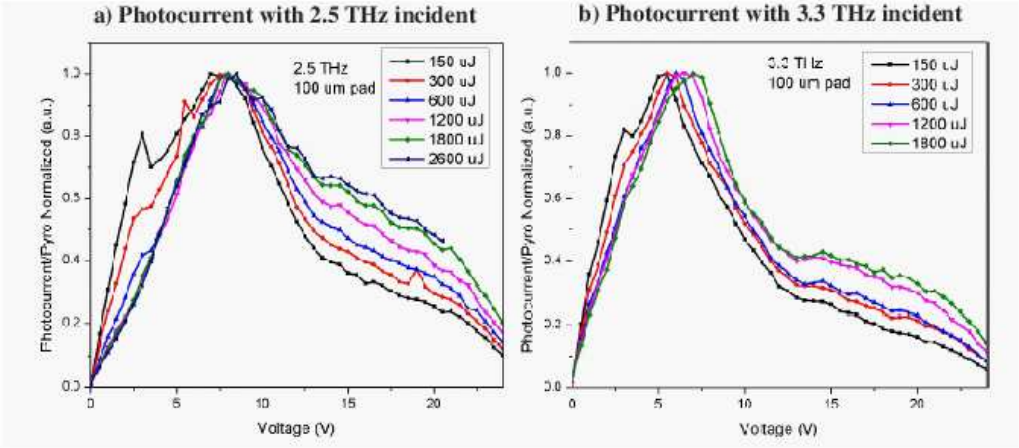

Figure 3.10: Power dependent photocurrent of the quantum cascade laser for two frequencies. All spectra are normalized to their maximum value.

between 2 V and 4 V. However, at larger applied biases, the features that appear are clearly frequency dependent. When the system is irradiated with light at 3.3 THz there is little response at applied biases above 4 V; the photocurrent only decreases as the voltage is increased. The system being driven at 1.5 and 2.75 THz show interesting features above 4 V, with several peaked features. However, the transitions being affected are not the lasing transitions; the THz frequency is far from the lasing frequency. The complexity of the full quantum cascade laser band structure presents a large number of possible explanations for the effects seen in the photocurrent data and prevents a straightforward interpretation of the QCL data. Unfortunately, due to time constraints, the

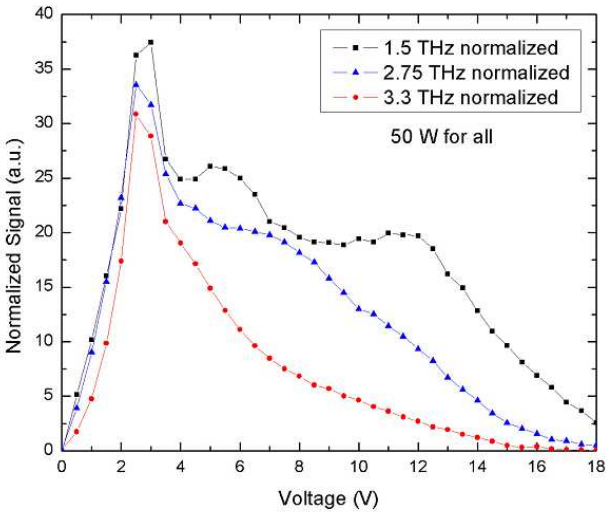

Figure 3.11: For 50 W pump power, the frequency dependent photocurrent response of the quantum cascade laser.

understanding of the THz interaction with the QCL structure is very limited and we are unable to conclusively say that stimulated emission was observed in this structure.

Though the complexity of the full QCL structure prevented a full understanding of the photocurrent results, the quantum post and well samples are a more straightforward system and yielded better results.

3.2.3.2 Single period quantum post and quantum well measurements

The ideal measurement would compare the photocurrent response at different frequencies and should only show a response for frequencies within the gain bandwidth of the QCL. However, as the experiments were performed, it became apparent that this approach fails to take into account the large number of electronic states present in quantum cascade lasers in addition to the upper and lower laser levels. These additional levels have some electronic occupation as current flows through the device, and they will shift as the bias is adjusted. In essence, at most biases there will be some set of levels in the structure that are approximately resonant with the FEL, and which can produce changes in the current via absorption of the radiation, sending the electrons into higher bands in the structure, allowing them to pass by the active region and produce an increase in current.

In the single period cascades, a quantum post cascade structure was compared with an identical reference structure where the quantum post layers were replaced with a 10% indium quantum well identical to the matrix well. In addition to a comparison of quantum well and quantum post structures, pho-

tocurrent vs. voltage curves from vertically and horizontally polarized THz light were measured to help differentiate between signal produced from actual quantized electronic transitions and background signals such as carrier heating. The vertically polarized light aligns along the growth direction and obeys the quantum well selection rules to be able to cause electronic transitions, whereas the light polarized parallel to the planes of the quantum wells should not be able to stimulate any quantum well transitions (Section 1.1.1). Only signals that differ for the two polarizations are of interest for the resonant photocurrent experiment. Any signal that is the same is due to background effects, shown to mainly be heating of carriers in the doped regions (Appendix D).

The current response of the single cascade quantum post (well) system has similar qualitative behavior at many different frequencies (Figure 3.12). First, there was very little response below 3 V (2.5 V) at all THz frequencies. Second, for the quantum post sample at all pump frequencies, an increase and plateau of the current response between 3 V and 4 V was observed. In the well samples there was an increase in the current and an onset of features between 2.5 V and 4.5 V. Finally, all THz frequencies showed a continuous increase in the current response as the applied bias was increased above 4 V (4.5 V).

In the quantum post samples, a difference was observed in the photocurrent

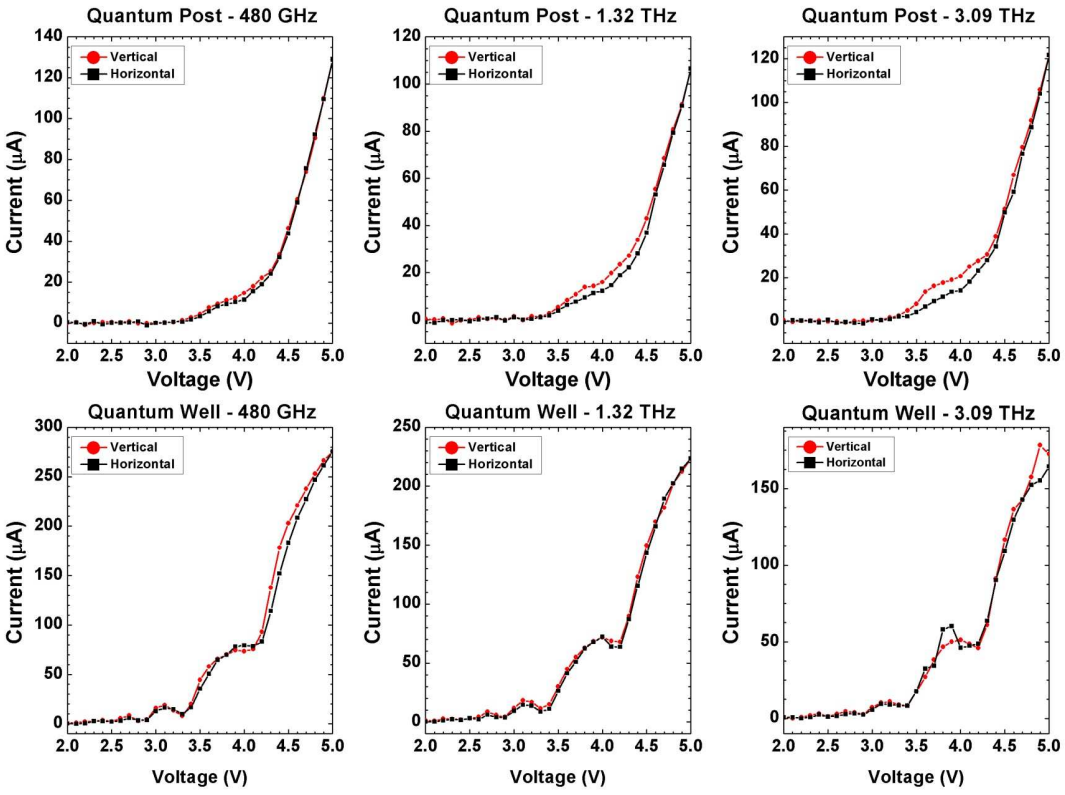

Figure 3.12: Frequency dependent photocurrent response for the single period quantum post and quantum well samples. Vertically polarized light is along the growth direction (z-direction) while the horizontally polarized light is in the plane of the quantum well (x-y direction).

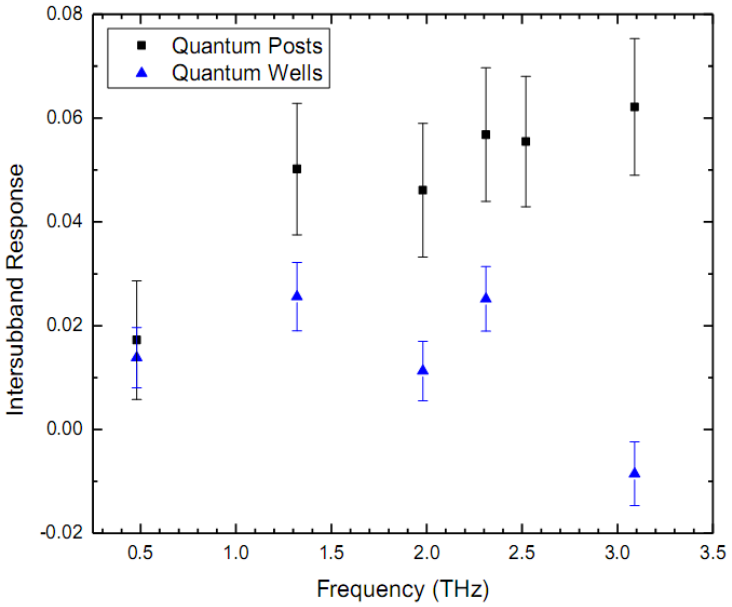

Figure 3.13: Frequency dependent intersubband response for the single period quantum post and quantum well samples.

response from the two polarizations of THz radiation between 3.5 V and 4.5 V. In the quantum well samples, no significant or systematic increase in photocurrent was observed for one polarization compared to the other. In order to quantify this difference, the difference of the vertical and horizontal photocurrent was integrated for both samples, and divided by average photocurrent at high voltages (> 4.5 V) to give a normalized intersubband response:

$$\text{Intersubband response} = \frac{1}{I_{avg}} \int_{V_{min}}^{V_{max}} (I_{vertical} - I_{horizontal}) \tag{3.1}$$

A positive "intersubband response" occurs when the vertical polarization has a larger response than the horizontal polarization, as is expected for a stimulated emission process. This intersubband response is plotted in Figure 3.13 for all the FEL pump frequencies that were accessible. While the response of the quantum well stays constant and close to zero, the quantum post sample response increases with frequency. This increased response over the quantum well reference sample indicates that some process involving the posts is responsible for this increase. However, the actual mechanism for the response is unclear. An emission being resonantly pumped as designed would produce this type of signal, but an absorption from the posts into the well as in Chapter 2

could produce a similar effect. Qualitatively, the results indicate that charge is being injected and extracted from the posts, but to determine the exact mechanism more work is required.

3.2.4 Further directions

A great deal of materials science effort would be required to make a quantum post cascade laser. Their growth is a highly non-equilibrium process, and every growth must be extremely carefully calibrated to even allow quantum dots and posts to nucleate properly. Further standardization of the growth process is the first step that would be necessary to fully explore the quantum post cascade concept. It is still unclear from the results to date whether or not a quantum post cascade is feasible from a device standpoint. However, it is an interesting structure in which to study the injection and extraction of charge from three dimensionally confining nanostructures. Understanding this physics better would lead to optimization of the structures and the design of the injection/extraction cascades. Additionally, the resonant photocurrent method should be investigated further. Unexpected complexities were discovered, but, this measurement still offers the possibility of a powerful technique to test new

concepts for QCLs in materials systems that are far too immature to build a working QCL and observe intersubband emission.

Chapter 4

Ultrafast Carrier Dynamics in InGaAs Quantum Posts

After the terahertz absorption experiments detailed in chapter 2, there were still unanswered questions about the terahertz behavior of the quantum posts. The single electron transitions that were the original goal of the experiments were still unobserved. Additionally, no knowledge of the time scales for basic processes such as charge capture into the structures were known. It was with this in mind that a collaboration with the ultrafast materials science group at the Center for Integrated Nanotechnologies at Los Alamos National Laboratory was formed. Several visits to Los Alamos were made to use an amplified laser system capable of both generating broadband terahertz pulses and optically pumping samples over a large frequency range in the near infrared.

The samples in this chapter consisted simply of two layers of quantum

posts, separated from each other and the surface by a GaAs spacer. No doping was added, and all the charge was generated by ultrafast laser pulses. Three samples were grown: a sample with two layers of 40 nm posts, a sample with two layers of 50 nm posts, and a sample with 2 quantum wells, each 40 nm thick to serve as a reference. Two sets of experiments were performed: pumping into the GaAs to observe the transient photoconductive response with the terahertz probe, and pumping with longer wavelength light below the GaAs band gap and directly into the well and posts to observe their intersubband behavior.

4.1 Terahertz Time Domain Spectroscopy

The main technique used in this section is terahertz time domain spectroscopy (THz-TDS).[43] Broadband pulses of terahertz radiation are created by femtosecond pulses of a near infrared laser. Multiple generation and detection schemes are used for THz-TDS, and considerable work has been performed on this technique in the last 10 years, extending the possible frequencies well into the mid-infrared.

A short ($<$100 fs) centered at 800 nm is split into two paths. The first pulse is used to generate the THz waveform, and the second is sent to a path

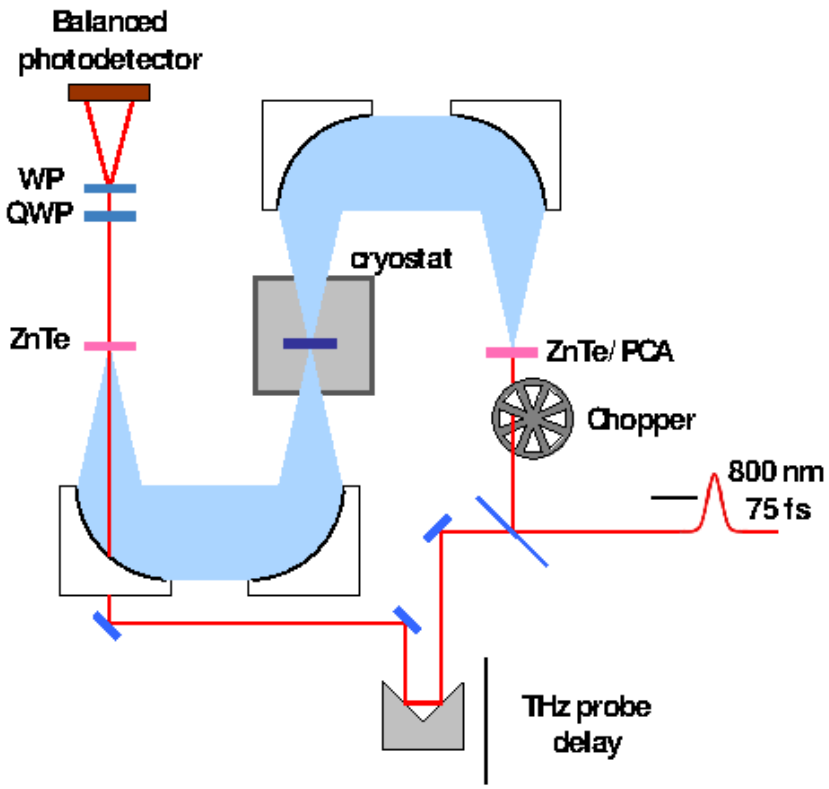

Figure 4.1: A terahertz time domain spectroscopy system, using optical rectification in ZnTe as the terahertz generation mechanism, electro-optic detection in ZnTe, and a Wallaston prism as the beamsplitter.

with variable delay. Depending on the system, a variety of emitters can be used. In this chapter, a ZnTe crystal is used to generate THz pulses via optical rectification. This pulse has a spectral range of ~ 0 to 3 THz. The terahertz light from the ZnTe is collected by an off-axis parabolic mirror, collimating the emitted light. A second off-axis parabolic mirror is used to focus the THz pulse into a small spot on the sample in a cryostat. The transmitted THz pulse is collected and collimated by a third off-axis parabolic mirror, and finally focused onto the detection crystal by a fourth. A second ZnTe crystal is used for the detection. The delayed 800 nm pulse that was sent through the delay path is timed such that the THz pulse and near-infrared pulse arrive simultaneously. ZnTe is a birefringent crystal, and the terahertz waveforms causes a slight change to the birefringence. This rotates the 800 nm pulse slightly.

The rotated pulse is then sent through a quarter waveplate, then a Wollaston prism or polarizing beam splitter, and each polarization is sent to a separate photodiode. These photodiodes are paired, and produce a total current that is proportional to the difference of the signal between them, $I_2 - I_1$. By producing circular polarization at the quarter waveplate when no terahertz is present, the light is an equal superposition of vertical and horizontal polarizations, and the currents from the two photodiodes are equal, producing a difference signal of

zero current. When the terahertz pulse rotates the 800 nm light's polarization, the light after the quarter waveplate is slightly elliptical in polarization, which will result in more intensity on one photodiode, and a corresponding non-zero difference signal. A terahertz waveform is much longer than an ultrafast pulse, so the pulse samples only a small part of the THz waveform. This signal is recorded and the delay is increased slightly, so that the pulse samples slightly later in the THz waveform. The delay is then scanned over the THz pulse, allowing the entire waveform to be measured with time resolution corresponding to the near infrared pulse duration.

4.2 Ultrafast Carrier Capture

For the first set of experiments, the goal was to determine the response of the quantum posts under ultrafast excitation with the pump laser tuned above the band gap of the GaAs. Electron-hole pairs are created directly in the GaAs, and from there can be captured by the quantum well and quantum posts. The terahertz waveform is then sent through the sample as shown in Figure 4.2. In this geometry, the terahertz waveform is partially absorbed by free carriers in the system. The degree to which it is absorbed is related to

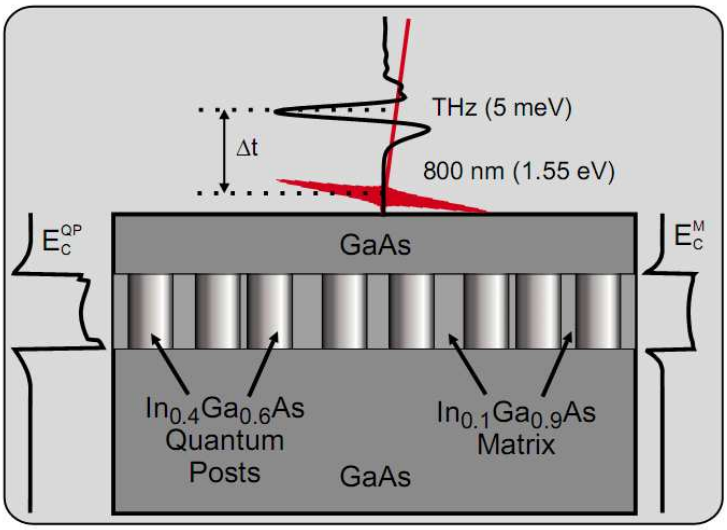

Figure 4.2: Experimental geometry at the sample for the 800 nm pump - terahertz probe experiment. An ultrafast pulse centered at 800 nm is incident on the sample, creating electron-hole pairs in the GaAs. The absorption of the terahertz signal that is measured is then a direct measure of the sample conductivity. [25]

the number of carriers in the sample. Only free carriers will contribute to this absorption, so the change in the electric field is essentially a measurement of the free carrier population as a function of time.[44, 45, 46] While the quantum posts have radial transitions that can couple to the terahertz waveform in the given geometry, the signal from these transitions will be buried under the large signal from free carrier absorption.

4.2.1 Experimental Setup

The experimental setup uses the terahertz time domain setup from Section 4.1, but is now modified to add the 800 nm pump pulse to generate carriers in the sample. This pump pulse can be delayed as well, so that it arrives before or after the terahertz waveform. To carry out the experiment, the transmitted waveform is first measured, to serve both as a normalization, and to find the THz probe delay to sit at while the optical pump is scanned (Figure 4.3). While the THz probe delay remains at this peak, the optical pump is then chopped, and the delay is scanned.

4.2.2 Experimental Results

Figure 4.4 shows the results of the pump scan for the quantum post and quantum well samples for different pump fluences. Zero time delay indicates when the THz pulse and the optical pump pulse arrive at the same time. Positive time delay indicates that the THz pulse is arriving after the optical pump pulse. A larger implies more absorption of the terahertz waveform, meaning that more charge is present in the sample. As the fluence is increased in both samples, the overall signal increases, which is expected as more charge is created

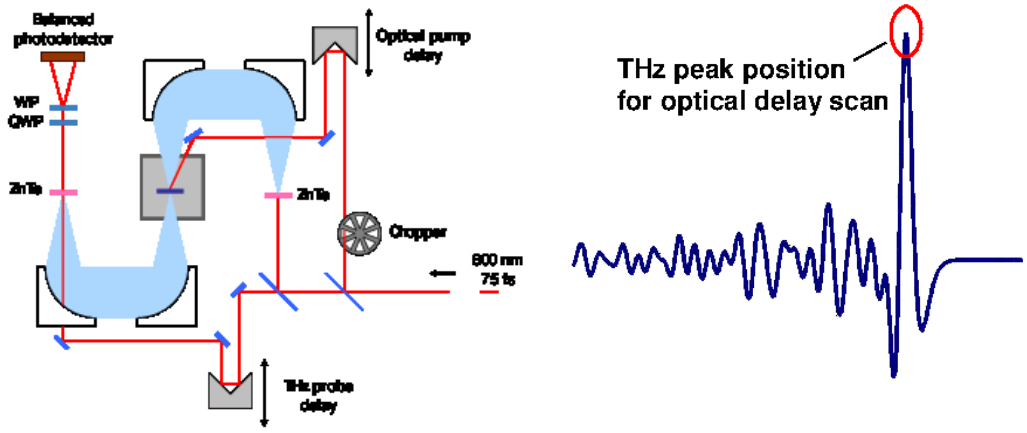

Figure 4.3: (left) Experimental setup for the 800 nm pump - terahertz probe experiment. An 800 nm pulse from a 250 KHz regenerative amplifier, approximately 75 fs in duration was used to both generate and detect the terahertz waveform, and to pump the sample. The sample was placed at normal incidence to the incoming terahertz waveform. (right) Example transmitted waveform, showing the peak delay for the THz probe. The THz probe delay remains at this position for the entire optical pump delay scan.

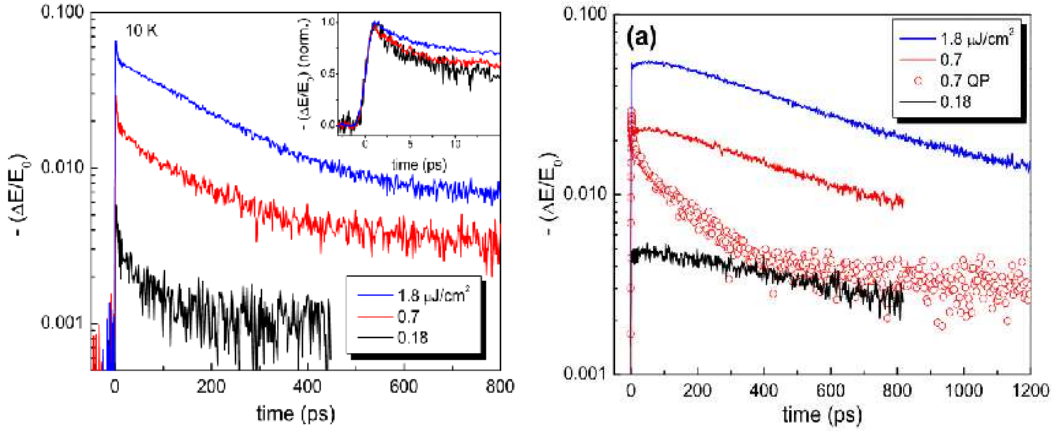

Figure 4.4: Time dependent change in the E-field vs. probe delay after the 800 nm pump pulse in the quantum post (left) and quantum well (right) samples. [25]

and more free carrier absorption occurs.

In the quantum post sample, there are two different timescales present in the response. Looking at the highest fluence (blue) curve, there is clearly a long time-scale delay, lasting for hundreds of picoseconds. In the quantum well reference sample there is a similar long time decay of the signal. This long time scale decay indicates the electron-hole pair recombination time in the bulk of the sample. At shorter time scales in the quantum post sample, there is an initial fast decay component, occurring in the first 5-10 picoseconds. Detail is shown in the inset. The quantum well reference lacks this fast time decay component. This leads to the interpretation that the fast time component is

capture of charge by the quantum posts. Their three-dimensionally confined states will not contribute to the conductivity signal, which is the reason for the rapid decrease. This result indicates that the posts trap charge very quickly, on the order of 10 picoseconds.

4.3 Ultrafast Intersubband Dynamics

For the second set of experiments, the goal was to eliminate the large signal associated with free carrier absorption. This signal is large enough to completely hide any response due to intersublevel transitions in the posts. To do this, the posts must be excited with a pump laser energy well below the band gap of the GaAs, tuned to be resonant with levels in the quantum posts.

Before the posts can be directly pumped, their band gap must be known. For this purpose, time dependent photoluminesence was performed on the 50 nm quantum post sample, shown in Figure 4.5. This indicates that the pump should be tuned between 1000 and $\sim$ 930 nm in order to pump the posts.

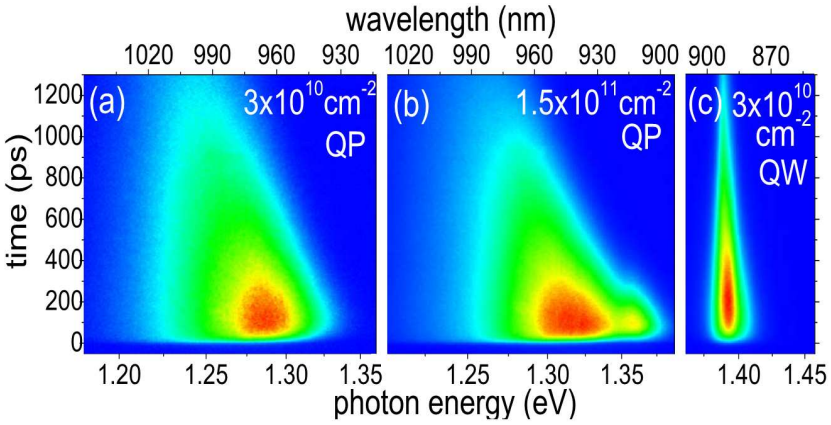

Figure 4.5: Time-resolved photoluminesence from the 50 nm quantum post sample, and the reference quantum well sample. This measurement is used to determine where the quantum posts and well samples should be pumped with the OPA. [25]

4.3.1 Experimental Setup

The experiment is similar to the 800 nm pump carrier capture experiment, but the pump beam is now sent to a UV OPA. The idler of this OPA is used, which allows the wavelength to be converted to the desired range from PL, between 930 and 1000 nm. As in the first experiment, the pump beam is chopped and directed onto the sample, which is now oriented at a 45 degree angle with respect to the THz beam. This allows the THz beam, whose light is polarized parallel to the page in Figure 4.6, to couple to vertical transitions in the quantum posts, which is not possible at normal incidence.

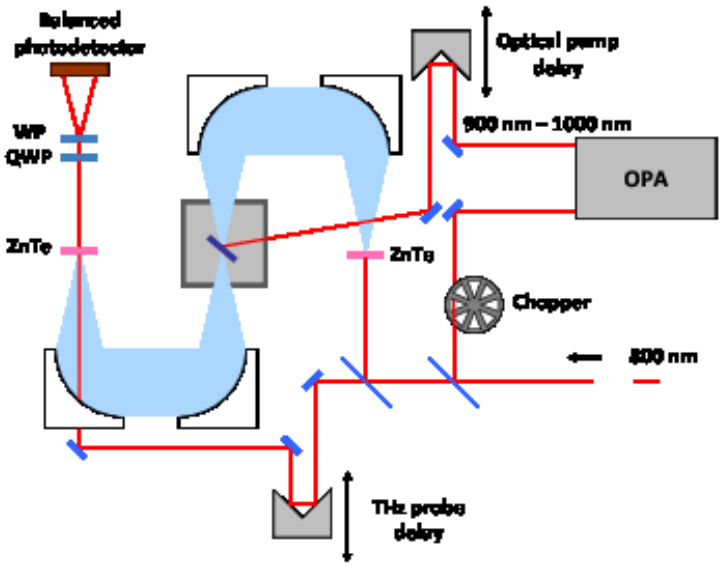

Figure 4.6: Experimental setup for the variable wavelength pump - terahertz probe experiment. The sample was placed at 45 degrees to the incident THz waveform, so that both horizontal and vertical polarization was present at the posts. A UV OPA was pumped with the 800 nm light, and the IR idler beam was used as the pump source for the quantum posts. This could be tuned over a large range, from 1000 nm to <900 nm while still keeping appreciable power levels. The THz waveform is polarized parallel to the plane of the page.

4.3.2 Experimental Results

The results for two pump wavelengths, 950 nm and 1000 nm, are shown in Figure 4.7. The time resolved PL shows that the two wavelengths pump at the high and low end of the post energy levels. Distinctly different behavior is evident for the two pump wavelengths.

For the shorter wavelength, 950 nm, the response starts off very small and spectrally broad for very short time delays after the pump pulse. However, as time goes on, the modulated electric field grows stronger, and the spectrum grows stronger and becomes peaked. Higher frequency components around 1.6 THz grow rapidly, while the lower frequency components initially present below 1 THz disappear at longer time delays. For the 1000 nm pump, the behavior is quite different. For longer time delays, the signal only gets smaller. It starts off spectrally broad and stays this way for longer delays. The overall spectrum decays, with no evidence of any peaked structure forming, as for the 950 nm pump.

The exact mechanism for this behavior is not well understood. The lifetimes of states in the posts are not known, and it is possible that the observed behavior indicates the time it takes for electrons and holes to decay from the

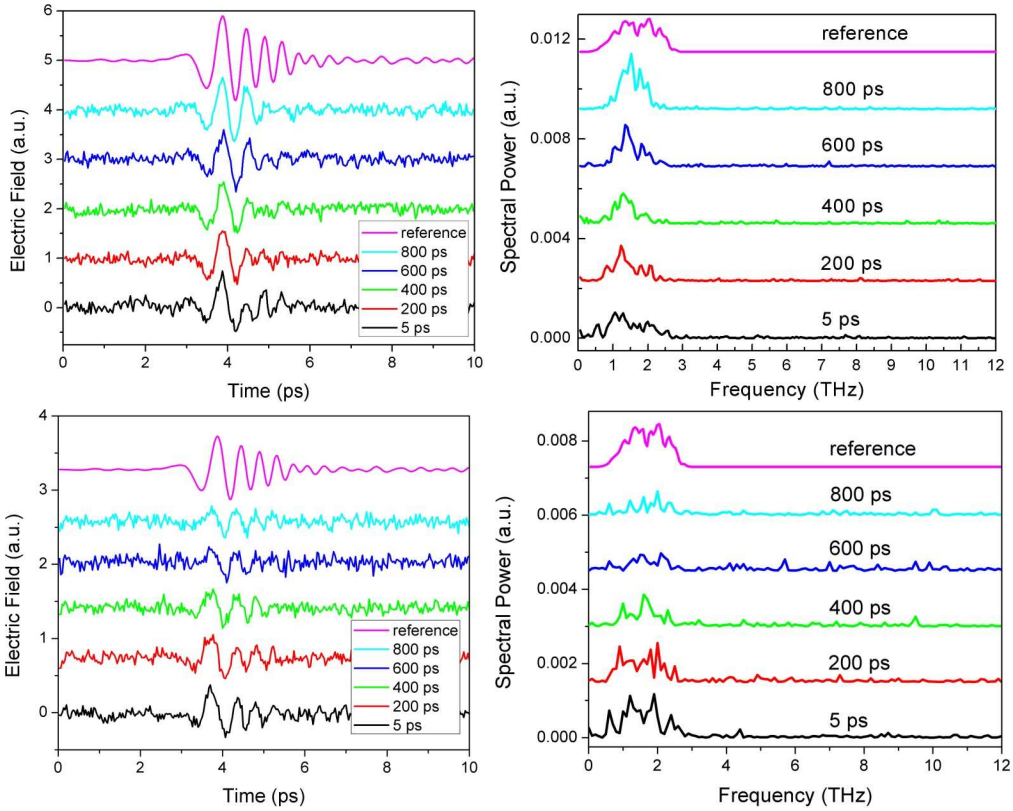

Figure 4.7: Electric field waveforms and their Fourier transforms for 950 nm and 1000 nm pump wavelength. The two pump wavelengths show markedly different spectral characteristics. The shorter wavelength pump produces spectra that increase in spectral intensity as time evolves, growing narrower. The longer wavelength (1000 nm) pump shows only a broad, decaying spectrum.

highest to lowest states in the posts. Another possibility is that the response of the posts is always broad because of the large number of closely spaced states in the posts, combined with their large inhomogeneous broadening. The signal at long time delays for the 950 nm pump could be charge that is able to occupy the well due to Auger processes in the posts. These then produce a strong absorption with a narrower linewidth. When the posts are pumped at lower energies, the Auger processes may be less likely, or less energetically favorable for charge at lower energy states in the posts. This leaves only the broad absorption from the posts, which decays over the 800 ps delay time.

4.3.3 Further Directions

To understand the results of the OPA pumped samples, a further wavelength dependence with intermediate wavelengths connecting the two behaviors would be desirable. Also, it is possible to increase the time delays more with the system. Seeing if the behavior for 950 nm changes at any point as the electron-hole pairs recombine could give further information about the behavior of the sample. Additionally, an important reference scan to determine the origin of each type of behavior is to switch the THz polarization to be polarized entirely

in the plane of the well, rather than half perpendicular to the well, half parallel to it. A polarization dependent measurement would distinguish between effects coming from intersubband transitions and those associated with possible free carrier absorption in the well.

Chapter 5

Period Doubling Bifurcations in Asymmetric Quantum Wells: Theory and Simulations

Period doubling bifurcations are dramatic changes in the response of driven dynamical systems such as the damped harmonic oscillator. For most values of the driving force and damping the response of the system occurs at the same frequency as the drive. However, for certain combinations of the driving force and damping, the system can undergo a period doubling bifurcation, and exhibit a response at half of the driving frequency.

For a single electron in a quantum well, a period doubling bifurcation is not possible, and the charge will always respond with the frequency of the electric field. The Schrodinger equation for this particle is linear, and period doubling bifurcations require a nonlinearity in the equations of motion. How-

ever, when many electrons are present in a well, non-linearity is introduced in the form of electron-electron interactions. It has already been seen (Section 1.1.1) that these effects can dramatically alter the intersubband absorption behavior of a quantum well through the depolarization shift. The similar energy scales of the Coulomb repulsion forces and the intersubband spacing make this non-linearity especially strong for quantum wells with terahertz intersubband energies. For specially designed, asymmetric quantum wells, this nonlinearity can have a significant effect on the equations of motion and produce period doubling bifurcations.[47, 48, 49]

This effect was first predicted by B. Galdrikian and B. Birnir [27] in 1994 at UCSB. They modeled the response of an asymmetric well under strong CW driving fields from the UCSB free electron laser. When the well was driven below the intersubband transition frequency, a complex response was predicted, including cascades of period doubling bifurcations that could eventually take the system to a chaotic response regime as the electric field strength was increased. Here, the same theory is used to design an asymmetric well with single bifurcations occurring at fields much lower than those investigated by Galdrikian and Birnir, and over a larger parameter range. The well is designed to be optimized for the frequencies and powers available at the free electron

lasers at UCSB and in Dresden, Germany. The simulations leading to this new, optimized well design are discussed in this chapter, while chapter 6 discusses preliminary efforts to experimentally observe period doubling.

5.1 Period Doubling Theory and Previous Calculations

Period doubling bifurcations in quantum wells were first theoretically discussed by Brian Galdrikian and Bjorn Birnir here at UCSB. The system they investigated was an asymmetric quantum well with terahertz intersubband transitions, driven with intense CW terahertz electric fields.

Under static conditions, the potential energy and eigenstates of the well can be calculated as described in Section 1.1.1. The potential in a quantum well is complicated by the addition of charge, which creates a new potential $V(z) = V_0(z) + V_{e-e}(z)$, where the term $V_{e-e}(z)$ takes into account the change in the well potential due to the interaction of charge.

When an AC electric field is then applied to the well, the potential must of course be modified. The electric field itself adds a potential $V_{E-field} =$

$eEz\sin(\omega t)$. However, this time varying electric field redistributes charge in the well, creating a time dependent electron interaction potential. The total potential is then:

$$V(t) = \delta v(z,t) + eEz\sin(\omega t) \tag{5.1}$$

where $\delta v(z,t)$ is the time varying electron-electron interaction potential. In order to solve for the equations of motion for charge in a well with this time varying potential, Galdrikian and Birnir moved to the density matrix formalism. They first approximated the asymmetric well as a two level well, ignoring higher subbands. For an asymmetric quantum well with a single barrier, this is usually valid, as the first two states are usually energetically quite close together, and the third state is pushed much higher in energy (much larger than typical energies of the terahertz driving photons).

The density matrix is then:

$$\rho = \begin{pmatrix} \rho_{00} & \rho_{01} \\ \rho_{10} & \rho_{11} \end{pmatrix} \tag{5.2}$$

In 5.2, ρ_{00} and ρ_{11} represent the fraction population of the ground and first excited state of the well, normalized such that $\rho_{00} + \rho_{11} = 1$. The off-

diagonal terms can create coupling between the two states. The density matrix formalism is powerful in some cases, as the expectation value of an observable A of the system can easily be found using $\langle A \rangle = tr\,(\rho A)$. The time evolution of the density matrix can be found using the time evolution of the Schrodinger equation:

$$\partial\rho/\partial t = -(i/\hbar)\,[H\,(t)\,,\rho\,(t)] - R\,[\rho\,(t) - \rho_0] \tag{5.3}$$

where R is a matrix that introduces dissipation into the system, and ρ_0 is the density matrix in thermal equilibrium.[50] If the time dependent Hamiltonian $H\,(t) = 0$, the relaxation matrix in Equation 5.3 will bring ρ back to the thermal equilibrium state ρ_0. The components of R are $R_{00} = R_{11} = \Gamma_1$, the energy relaxation rate in the quantum well, and $R_{10} = R_{01} = \Gamma_2$, the energy dephasing rate. Galdrikian and Birnir calculated the response of the two-level asymmetric quantum well to a strong terahertz driving field, using Equations 5.1 and 5.3, to obtain the equations of motion:

$$\dot{\Delta} = (4/\hbar)\,V_{10}(t)\,\mathrm{Im}\rho_{10} - \Gamma_1\,(\Delta - \Delta_0) \tag{5.4}$$

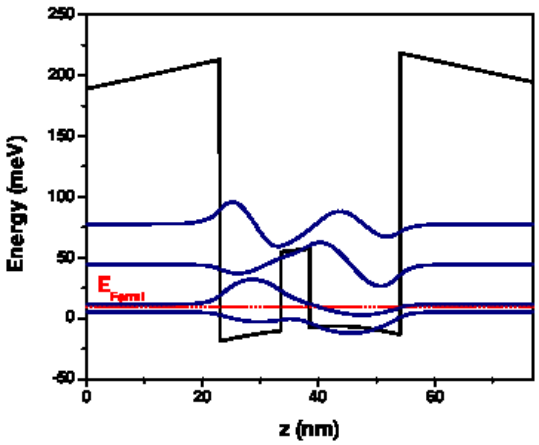

Figure 5.1: The original design of the the asymmetric well from B. Galdrikian and B. Birnir. The sample for this calculation is charged with $1.5\text{x}10^{11}/\text{cm}^2$. The intersubband spacing between the ground and first excited state is 6.2 meV, while the first to second excited state energy is 32.9 meV, ensuring that the two state approximation is valid at the relevant low temperatures.

$$\dot{\rho_{10}} = -i\left[\omega_{10}\rho_{10} + (\zeta/\hbar)\, V_{10}\right] - \Gamma_2\rho_{10} - (i/\hbar)\, V_{10}\,(t)\,\Delta \tag{5.5}$$

with the potential matrix element $V_{10}\,(t)$:

$$V_{10}\,(t) = eEz_{10}sin\,(\omega t) + \alpha\hbar\omega_{10}\left[\text{Re}\rho_{10}\,(t) - (\zeta/4)\,(\Delta - \Delta_0)\right] \tag{5.6}$$

where $\Delta = \rho_{00} - \rho_{11}$, Δ_0 is the population difference in thermal equilibrium, $\alpha = 8\pi e^2 N_s S_{1010}/\kappa\omega_{10}$ is the depolarization shift introduced in Section 1.1.1, and $\zeta = (z_{00} - z_{11})\,/z_{10}$ characterizes the asymmetry of the well.

These equations of motion are complex, but an important thing to note is the source of the nonlinearity that produces period doubling. In Equation 5.5, the last term is $(i/\hbar)\, V_{10}(t)\, \Delta$, which will produce a term $\alpha\zeta\, (i\omega_{10}/4)\, \Delta^2$, which is a source of nonlinearity in the equations of motion. This term illustrates the fact that the depolarization shift AND the asymmetry of the well are both required to produce this nonlinear term. These parameters must be controlled very precisely during the design of the asymmetric well in order for a period doubling bifurcation to occur.

The well that Galdrikian and Birnir designed is shown in Figure 5.1. An asymmetric step in the well produces two closely spaced states at low energies, significantly separated from the upper states in order to satisfy the two state approximation. The response of the well was then simulated over hundreds of periods of the drive field cycle, using Equations 5.4 and 5.5. This time dependence of the density matrix was then used to compute the expectation value of the charge density, $\langle z \rangle$. At each electric field strength, $\langle z \rangle$ is sampled once per drive cycle for several hundred drive cycles. For motion with the period of the driving radiation, all the sample points should lie on top of each other. However, if a period doubling bifurcation occurs, there should be a component at half the drive frequency, so if the points are sampled they should

now only lie on top of each other once every two cycles, and two points will be produced. (Figure 5.2).

When charge responds to the drive at half the frequency, this creates an electric dipole oscillating at this subharmonic frequency. This oscillating dipole radiates at this half frequency, which is then the observable quantity in the experiment. The characteristic of a period doubling bifurcation is a subharmonic signal that occurs over a limited range of driving electric fields.

B. Galdrikian drove the original well design at 500 GHz, which produced the complicated bifurcation behavior shown in Figure 5.3. For this drive frequency, well below the frequency of the intersubband transition (1.5 THz), cascades of period doubling bifurcations can occur, eventually leading to chaotic behavior. The bifurcation regions produce emission at an increasing number of subharmonics as the number of period doubling bifurcations increases, until the emission finally becomes completely broadband when the bifurcation diagram shows chaotic behavior.

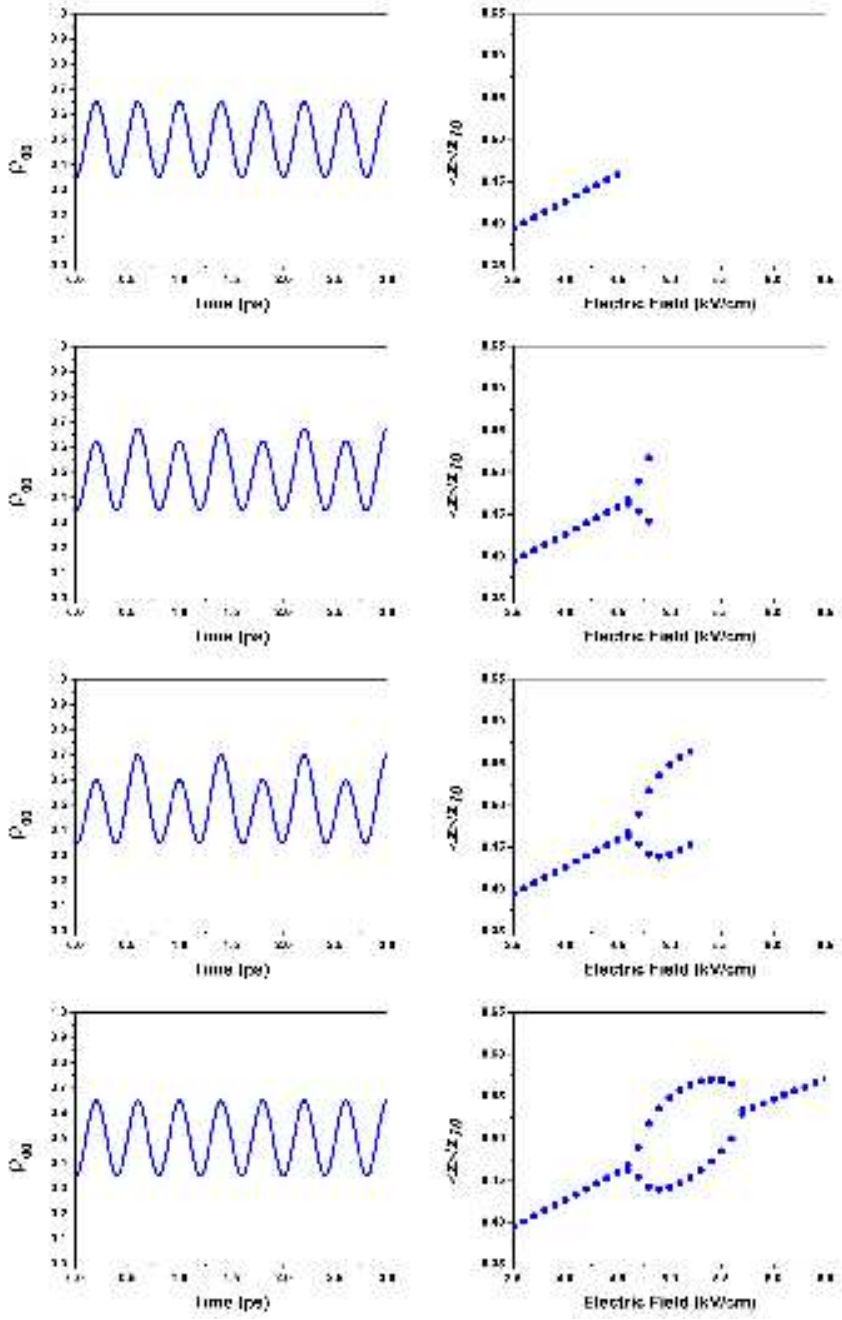

Figure 5.2: ρ_{00} and the associated mapping of $\langle z \rangle / z_{10}$ as a period doubling bifurcation occurs.

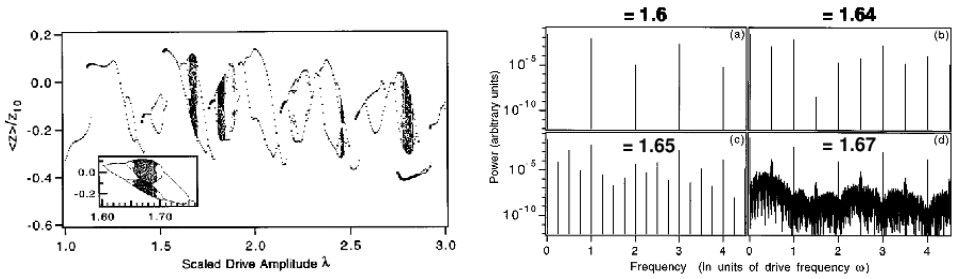

Figure 5.3: Bifurcation diagram (left) and associated emission power (right) for B. Galdrikian's well design. λ is a unitless parameter that scales directly with the electric field. For this well, $\lambda = 1 \approx 10$ kV/cm.[27]

5.2 Redesign of Optimal Samples

The sample design of Galdrikian and Birnir is not optimal for experimental observation of period doubling. In their paper, they drive the well at 500 GHz, which produces more interesting bifurcation behavior in their sample. However, electric fields of well over 10 kV/cm are required in order to observe the predicted behavior. Achieving these field strengths at 500 GHz is not possible at the UCSB FEL, as the diffraction limited spot size is too large to achieve these fields at the powers the FEL can produce. The FEL in Dresden can produce higher peak powers, but the lower frequency limit is 1.2 THz.

Modeling this initial well design under higher frequency drive shows that period doubling bifurcations can occur at lower electric fields (Figure 5.4), but they are still at the high end of the UCSB FEL's capabilities. With this in mind,

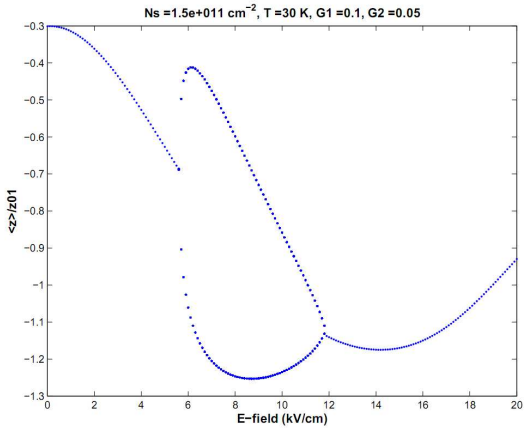

Figure 5.4: The period doubling bifurcation in B. Galdrikian's sample design at 103 cm-1. The electric fields required to reach the period doubling bifurcation are high for the UCSB FEL, and the electric fields to move past the bifurcation are not possible even with optimal coupling and focusing at UCSB.

we set out to design a new sample optimized for frequencies where high power densities could be achieved, both at UCSB's FEL and the FEL in Dresden. The goals in the redesign of this sample were: 1) To optimize the period doubling response for 84 cm-1, a frequency with high power levels at both FELs, 2) To minimize the terahertz electric field strength required to produce a bifurcation, 3) To find a sample design where period doubling bifurcations occur over a large range of sample parameters, making the phenomenon more robust to the real variations that are possible in an experiment.

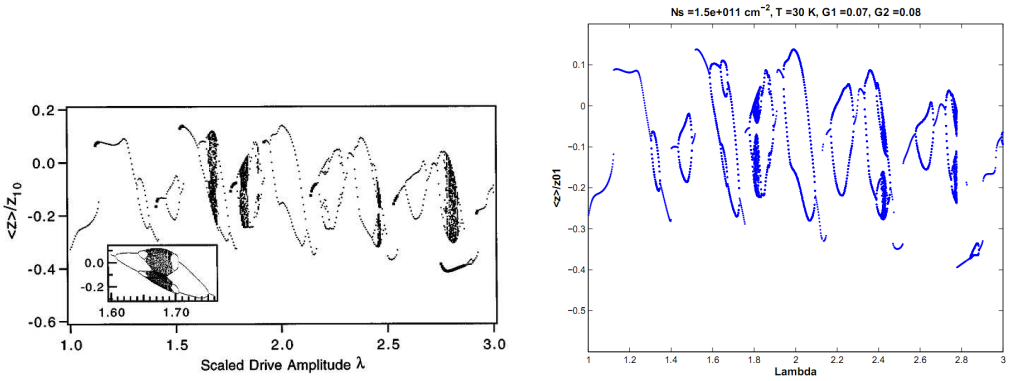

Figure 5.5: The original bifurcation diagram from [27] (left), and the reproduced bifurcation diagram using the new bifurcation code.

5.2.1 Simulations

The first step in the process was to produce a computer code capable of solving the exact states of a given quantum well, then simulating the well's period doubling response. B. Galdrikian wrote a Schrodinger-Poisson code during his graduate career to solve for the exact states and energies for a quantum well. This code was moved from Mac to Windows, then combined in C with code I wrote to solve the differential equations of motion from section 5.1. Notes on this code are in Appendix E.

The first step was to verify the code by reproducing B. Galdrikian's original results, which is shown in Figure 5.5.

Once this check was performed, the next step was to perform simulations

over a large parameter range. Figure 5.6 shows the set of parameters that were varied in the simulations. The simulations were set up to solve for the wave functions and energies of a given well, then simulate its behavior under strong terahertz driving fields at 84, 103 and 110 cm^{-1} (three frequencies the FELs at UCSB and Dresden are both capable of producing with high power). If the well produced a bifurcation, the electric field where the bifurcation first occurred was recorded. The goal was to produce bifurcations at the minimum electric field below 10 kV/cm, the maximum estimated field under optimal conditions at UCSB.

These simulations were used to produce diagrams of the bifurcating electric fields for various well designs, as shown in Figure 5.7. This shows the simulation for a well width of 40 nm. The position and height of the asymmetric step is varied, all for constant temperature and values for $\Gamma_1 = 0.1$ and $\Gamma_2 = 0.05$. In order to ensure the two state approximation from the theory was valid, it was required that the spacing between the first and second subband in the well be less than four times the first and third subband spacing, i.e. $4E_{12} < E_{13}$.

The simulations indicated that moving the intersubband spacing towards lower frequencies than the 31 nm well in B. Galdrikian's work was favorable for period doubling. This is accomplished by making the well wide. An ex-

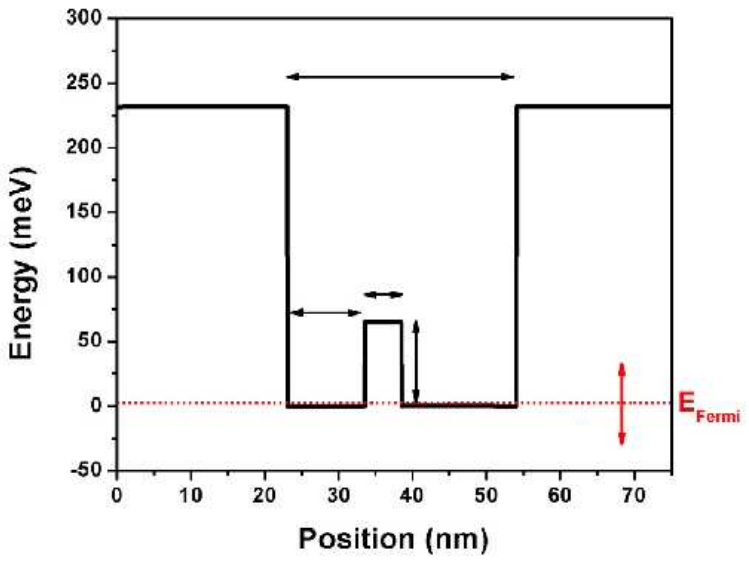

Figure 5.6: Parameters that were varied in the search for the ideal period doubling well. In addition to the width, step height, step width, and step position shown, the total charge density N_s, the dissipation parameters Γ_1 and Γ_2, and the temperature were also varied.

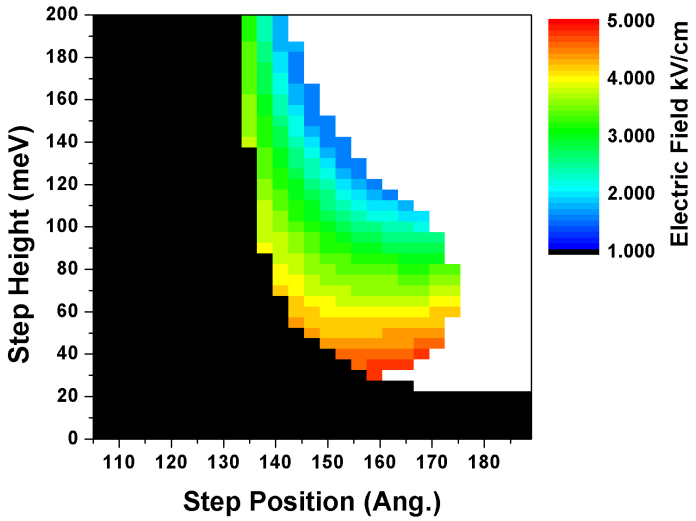

Figure 5.7: A simulation of a 40 nm quantum well, at 30 K with $\Gamma_1 = 0.1$ and $\Gamma_2 = 0.05$, for various step heights and step positions. Black regions of the plot do not satisfy the two state requirement ($E_{13} = 4E_{12}$), while white regions do not produce bifurcations below 10 kV/cm.

ample of the comparisons performed are shown in Figure 5.8. For an 84 cm^{-1} pump frequency and 3 nm step width, the bifurcation diagrams for increasing well widths are plotted. Already, it is apparent that wider wells near 385 and 410 Angstroms are producing the widest range of wells with bifurcations. Conditions become more favorable when the intersubband spacing is lower due to the fact that the depolarization shift becomes larger. From Equation 1.16 we know that lower intersubband spacings increase the depolarization parameter α, which is key in the nonlinearities of the period doubling equations of motion. It was also found that the drive frequency that would produce bifurcations in these structures was 84 cm^{-1}, which is where most of the experiments in Chapter 6 were performed.

Moving in on the wide well region, the optimal step size was then explored. Figure 5.9 shows the results when three step sizes are compared for the 385 Angstrom well. For wide wells such as this, it was consistently found that the best bifurcation diagrams were produced for step widths of 2 nm. After more exploration of the parameter space, it was found that the optimal well and step width were 40 nm and 2 nm, respectively.

With these parameters, the charge density was then varied, shown in Figure 5.10. The goal of this was to choose a step height and position that would bi-

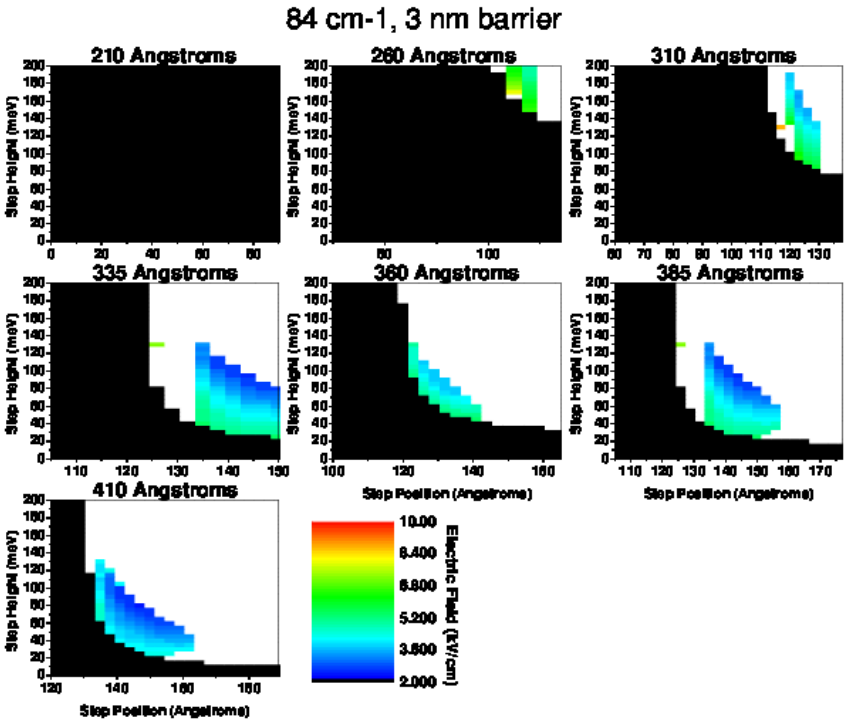

Figure 5.8: Bifurcation maps for various well widths, each with a 3nm thick barrier and pumped at 84 cm-1.

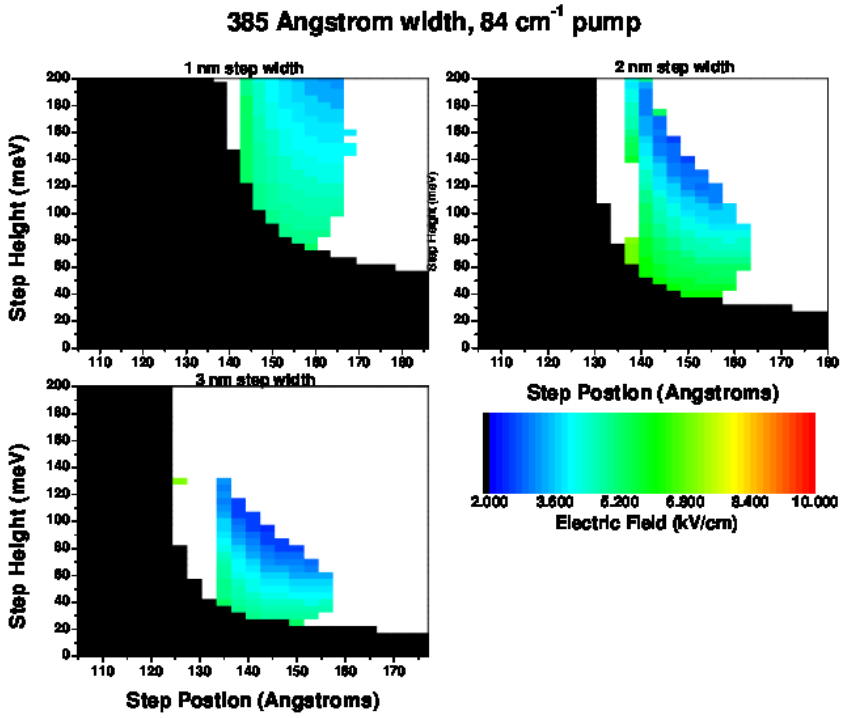

Figure 5.9: For a 385 Angstrom well, three step widths were tried. 2 nm was chosen as the ideal, because it produced the largest area of bifurcation with low electric field strengths required.

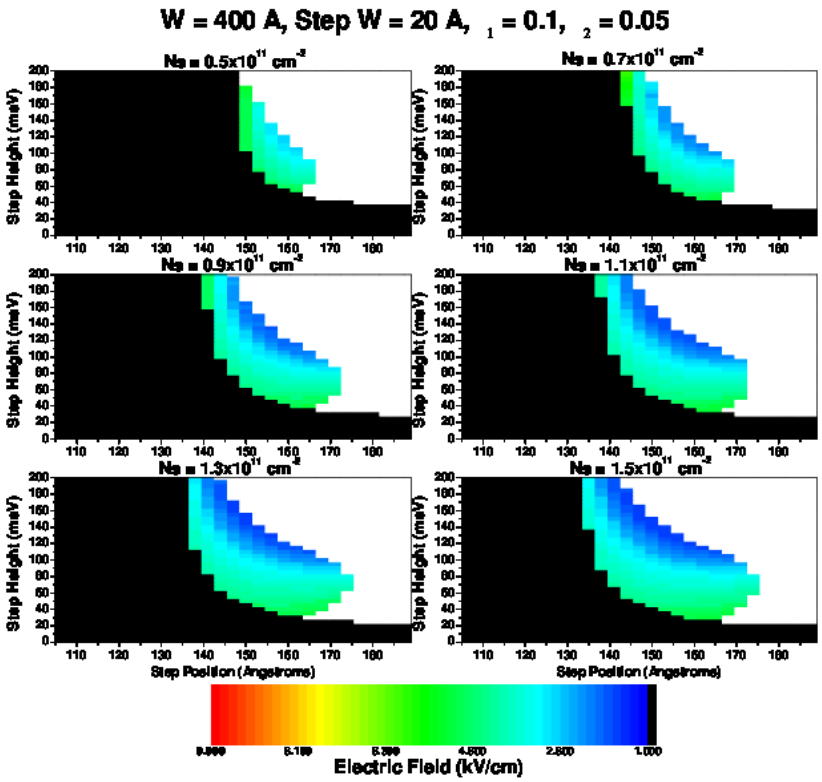

Figure 5.10: Charge density variation maps.

furcate at a number of charge densities. A step position of 150 Angstroms, and height of 100 meV (13% Aluminum) were chosen based on these simulations.

Finally, the sample was simulated for different values of Γ_1 and Γ_2, shown in Figure 5.11). The values of $\Gamma_{1,2}$ for the real well could vary, so this simulation was important to get a realistic idea of the bifurcation's robustness to different relaxation rates. The chosen sample (shown by red lines) produces a bifurcation

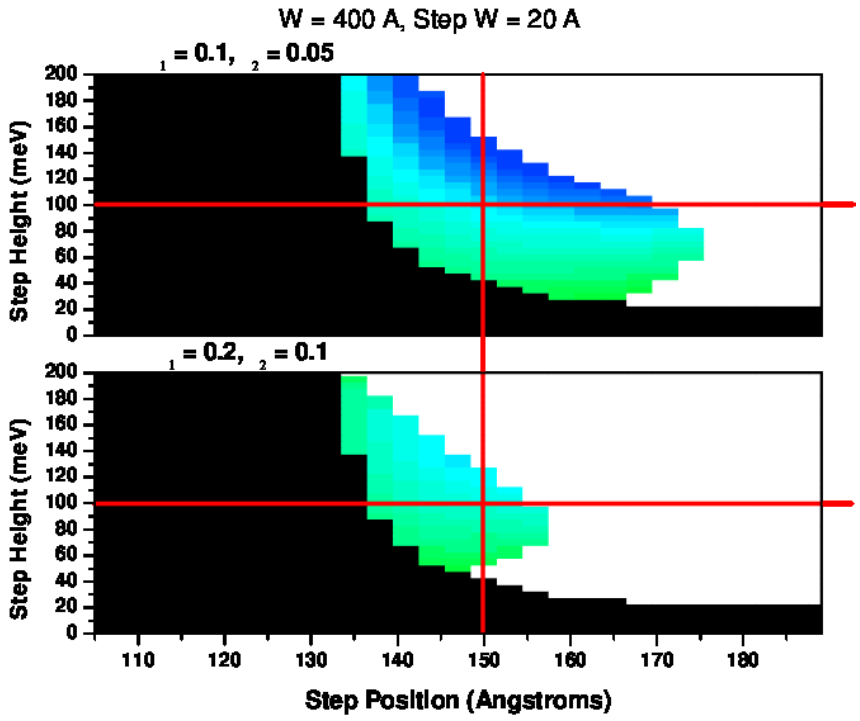

Figure 5.11: Gamma variation map.

for both simulated values of $\Gamma_{1,2}$.

5.2.2 New well design

The band structure and associated electron states for the final design, along with the bifurcation diagram, are shown in Figure 5.12.

Once found, this design was then further simulated at a large variety of charge densities and temperatures. One of the biggest unknown factors in the

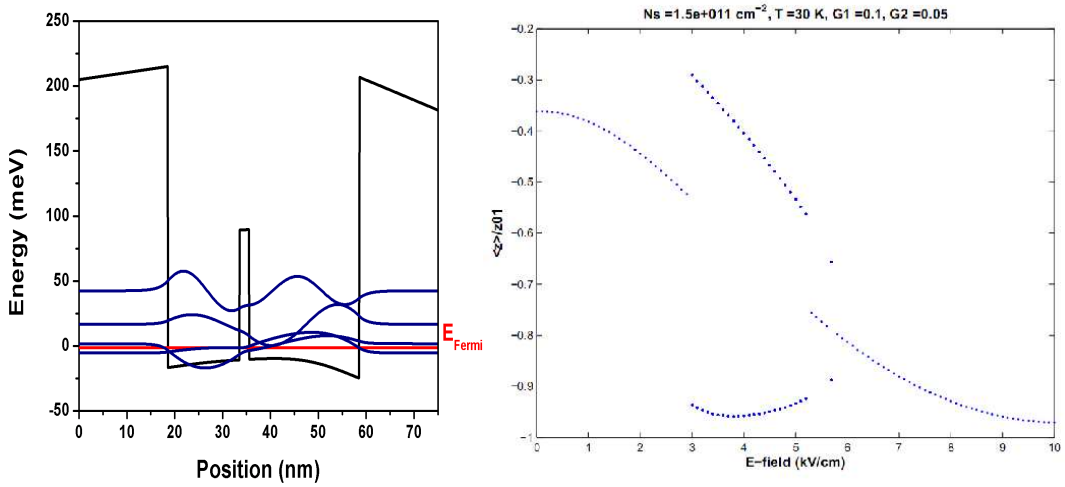

Figure 5.12: The newly designed period doubling sample structure, with a charge density of 1.5x10^{11}/cm^2. The total well width is 40 nm. The asymmetric barrier is placed 15 nm from the well edge, and is 2 nm thick, with ~13% AlGaAs making the barrier $\sim$ 100 meV.

experiment is the temperature of the electrons when illuminated with the FEL. While the sample itself is cooled to 4 K, the electrons themselves can have a much higher temperature if they are excited by intense THz fields. Temperature dependent simulations of the sample (Figure 5.13) show that bifurcations can be expected over a large temperature range. Additionally, bifurcation diagrams at a number of sheet charge densities in the well were performed. It has been shown [51] that as the charge density decreases, Γ_2 also decreases, which is favorable for period doubling.

In reality, practical limitations during growth make the exact structure

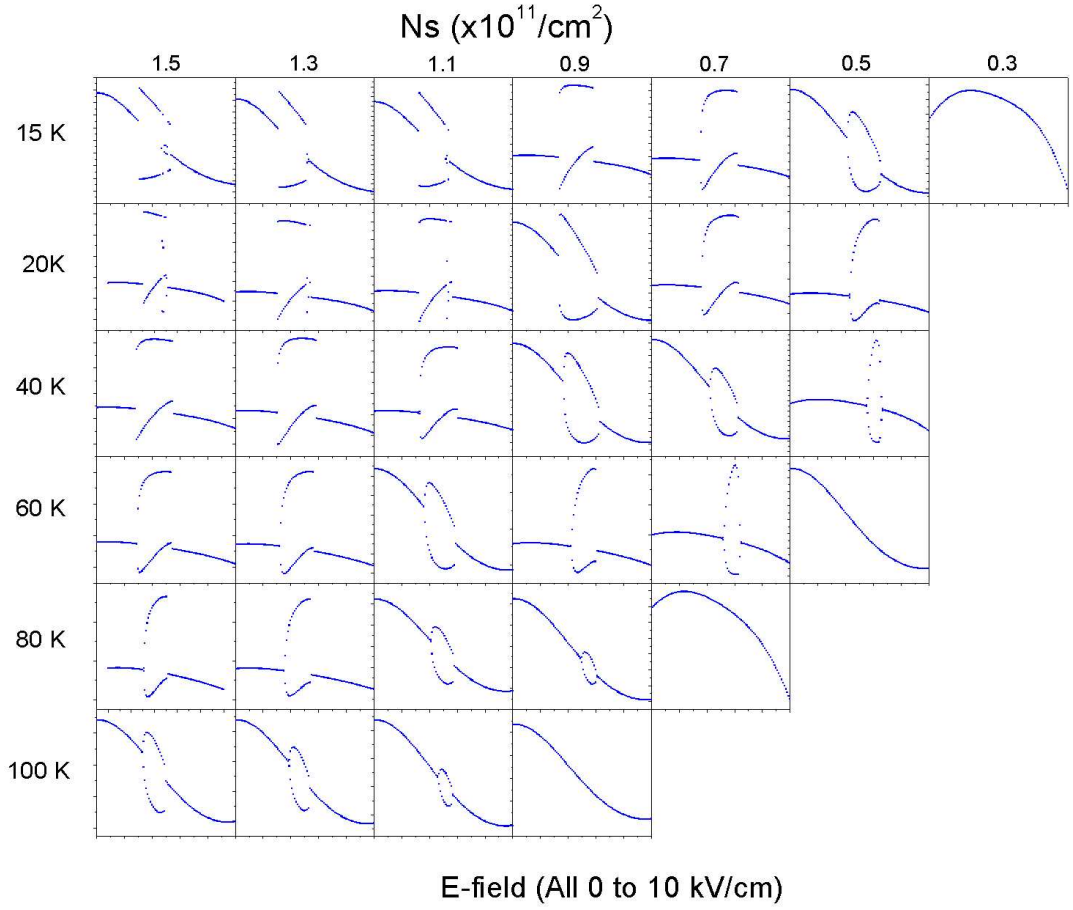

Figure 5.13: Temperature and charge dependent bifurcation simulations of the new sample design.

of Figure 5.12 difficult to grow. During MBE growth, the temperature of the Aluminum cell determines the x value for $Al_xGa_{1-x}As$. To make the well deep enough to produce well confined states, $x = 0.3$ is used for the barriers, producing barriers approximately 230 meV in height. The small asymmetric step in the well, however, is only 100 meV, corresponding to an aluminum content of $\sim 13\%$. Changing the temperature of the cell enough to produce $x = 0.13$ takes a significant amount of time, in which the GaAs of the well becomes dirty due to the background particle levels of the chamber. To avoid this, the grower had to approximate the 2 nm thick, 13% barrier by two smaller AlGaAs layers with 30% aluminum content, which average out to 13% over the 2 nm spacing. On the scale of the electron wave functions, which are spread across the 40 nm well, this should look very similar to a 2 nm step of the appropriate aluminum content.

5.2.3 Sample structure

The well itself was placed in a special structure designed to allow for independent control of the charge density and electric field across the sample. In a sample with just a doped active quantum well and front Schottky contact, the

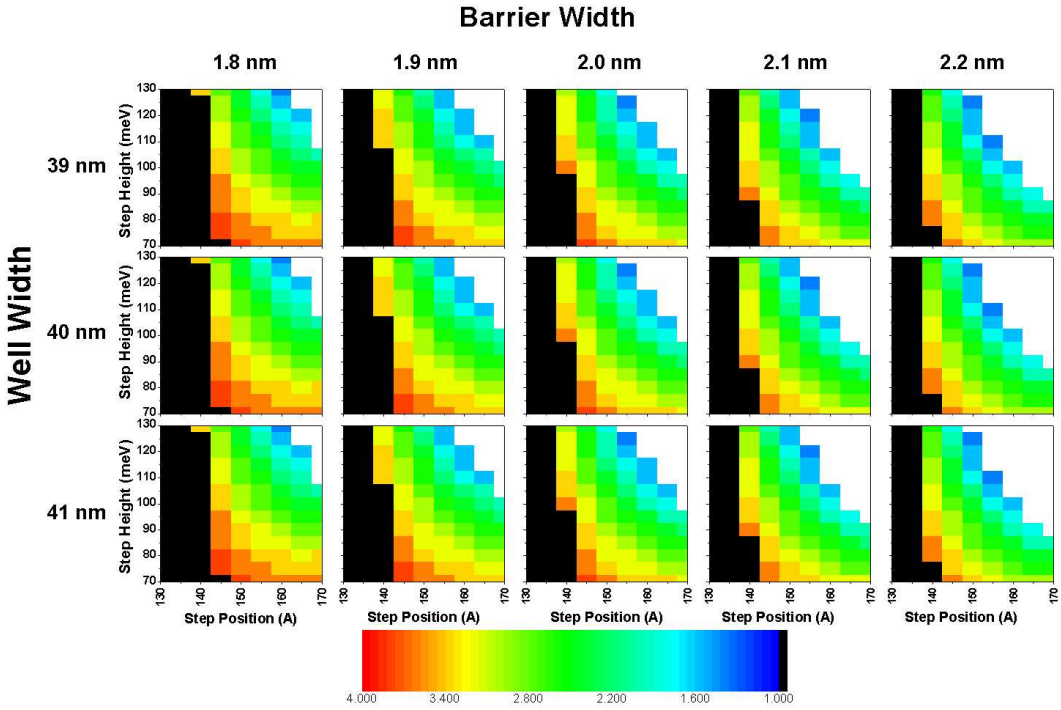

Figure 5.14: Final simulations of the period doubling sample before growth, to ensure that small possible variations during growth leave a large enough margin of error so that period doubling can still be expected to occur.

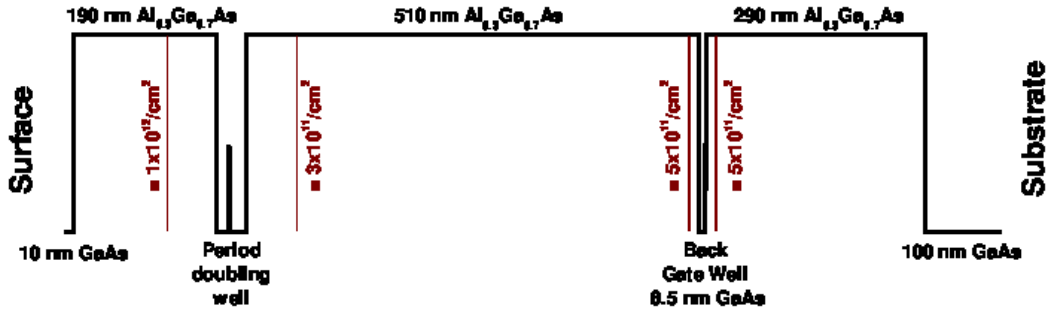

Figure 5.15: Sample structure, including a back gate well to independently change the electric field across the active well and its charge density.

charge density and electric field are altered simultaneously with applied voltage and cannot be separately controlled. For most voltages, the transition is Stark shifted away from the simulated flat band conditions, producing a well with both the incorrect electronic spacing and a broader transition. This means that the well will have a fixed charge density at flat band, and most of the flat band charge density states simulated in Figure 5.13 will not be accessible.

To increase the available range of charge densities accessible at flat band conditions, a second doped well was added below the first (Figure 5.15). This well can be independently contacted and biased, and used to alter the flat band electric field. [52]

Finally, simulations of the sample structure were performed for different DC electric fields to simulate the effect of an applied bias (Figure 5.16). For

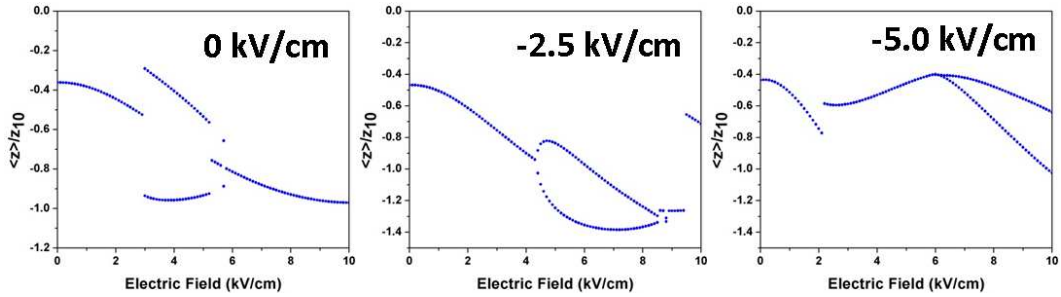

Figure 5.16: Bifurcation diagrams for several applied electric fields, using the new well structure at 30 K and $1.5 \text{x} 10^{11}/\text{cm}^2$ electron density.

modest electric fields, the period doubling bifurcations still occur, albeit at higher AC field strengths. For the sample structure in Figure 5.15, applying negative biases at the front Schottky contact (reverse bias) is acceptable, but large positive biases past flat band conditions (forward bias) will begin to draw current across the sample. Due to the asymmetry, only negative electric fields produce bifurcation diagrams, while positive electric fields destroy them. Thus, the smaller side of the asymmetric well was placed closer to the surface of the sample, so that the negative applied bias on the Schottky gate would produce the proper electric fields across the well.

5.3 Continuous wave vs. pulsed measurements

The simulations described so far have all assumed that the electric field is a continuous wave. For the FEL at UCSB, this is a good approximation. Pulses last for between 1 and 3 microseconds, which at 2.5 THz would correspond to $2.5 - 7.5$ million cycles. The simulations come to a steady state response behavior within approximately 100 cycles, so for all intents and purposes they are CW pulses if the measurement is made only during the pulse. From the perspective of reproducing the simulations, these pulses are ideal. However, the FEL at UCSB has the disadvantage of a low repetition rate (1 Hz) and poor power stability.

The FEL at Dresden has a very high repetition rate (13 MHz) and good power stability. However, the pulses are much different than those at UCSB. It produces short pulses, whose durations are $\sim$ 15 picoseconds. For finding a period doubling signal, this laser has distinct advantages over the UCSB FEL, but the response to these short pulses were unknown. To determine this behavior, further simulations were performed with short pulses like those at the FEL in Dresden.

Figure 5.17 shows the results of simulations with Gaussian pulses of varying

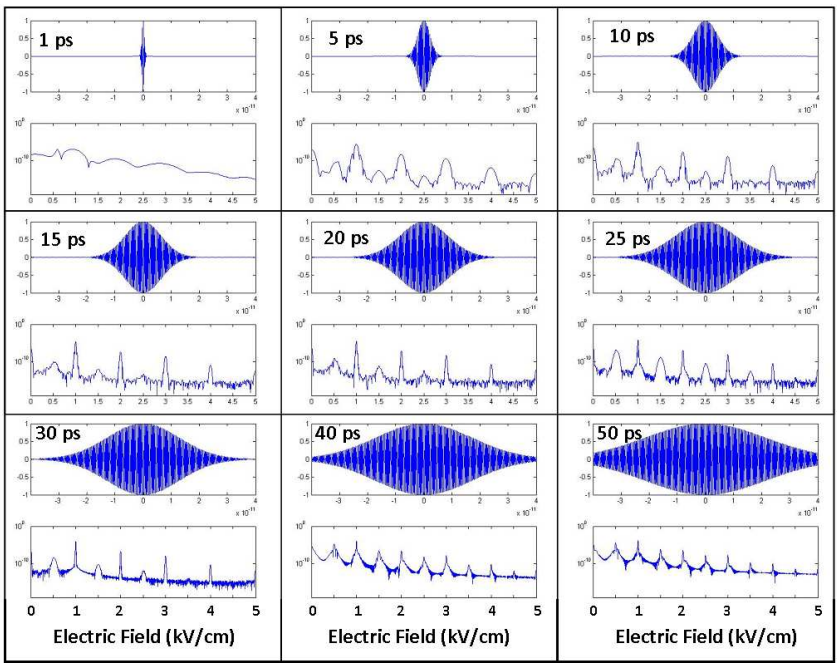

Figure 5.17: Simulations of short pulses to see the response expected at the Dresden FEL. All simulations have peak electric field values of 4 kV/cm, $\Gamma_1 = 0.1$, $\Gamma_2 = 0.05$, $N_s = 1.5\text{x}10^{11}/\text{cm}^2$, T = 30 K.

lengths. Top panels show the electric fields of the pulses with the corresponding pulse durations. The bottom panels of each figure show the emitted power. The short pulses produce subharmonic emission just as the long CW pulses, but the emission is much broader in frequency response. This corresponds to the increased pulse bandwidth for the short pulses. This check shows that the short pulses at Dresden can be used.

Chapter 6

Initial Searches for Period Doubling Bifurcations in Quantum Wells

After the extensive calculations performed in Chapter 5, a sample following the new design was grown. A previous sample using the design modeled by B. Galdrikian had been grown in 1996, and experiments to search for period doubling bifurcations were performed on both samples. The new sample was grown according to the new design structure of Figure 5.12. The 1996 sample was grown prior to the development of the back gated sample design, and consists of only the quantum well active region, a barrier, and a front Schottky gate.

Unfortunately, the full functionality of the back gate quantum well was never realized in the new sample, due to difficulties during processing. Both

samples lacked the ability to independently adjust the charge density and electric field. After the period doubling experiments were performed, it was discovered by the clean room staff that for the normal nitrogen flow rates used, the thermal annealer was miscalibrated, leading to extremely high temperatures at the sample ($>$ 100 C over the targeted annealing temperature). This caused contacts to the active quantum well layer to spike through the AlGaAs barrier into the backgate quantum well, leaving the two layers shorted and making it impossible to apply independent bias to the two wells.

6.1 Capacitance

As in Chapter 2, capacitance was the main tool used to investigate the charging of the sample. The charging of the two samples are shown in Figures 6.1 and 6.2.

For the new sample design, charging of the asymmetric quantum well begins at -0.6 V. Before this charging occurs, there is a large background capacitance. This is due to the fact that the back gate quantum well is shorted to the active quantum well, but is more heavily doped and further from the surface. Within the range of voltages before reverse breakdown of the diode structure occurs,

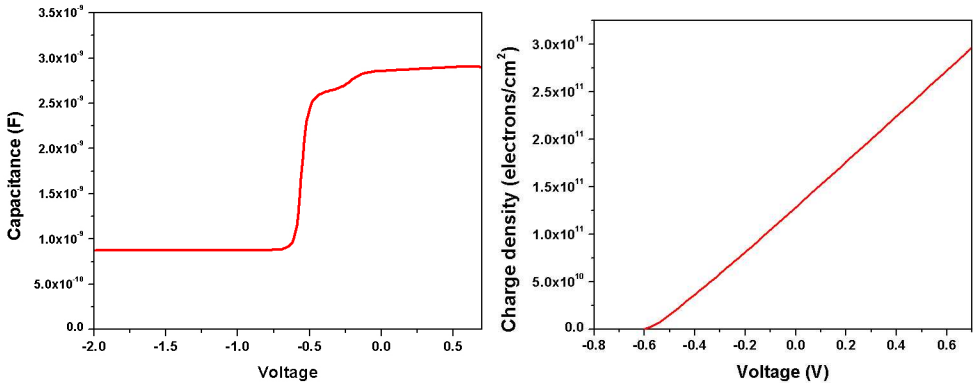

Figure 6.1: Capacitance and integrated charge density for the newly designed sample.

Figure 6.2: Capacitance and integrated charge density for the older sample design.

it was impossible to deplete this backgate well.

For the older well design, the onset of capacitance occurs near -1.0 V. However, without the backgate, there is no large background capacitance. In both samples, the capacitance shows a slight additional rise after the onset of charging. This is thought to be the charge density and electric field where a large fraction of the charge in the asymmetric well shifts to the other side of the small step closer to the surface of the sample, causing a slight increase in capacitance.

6.2 Intersubband spectroscopy

Intersubband spectroscopy was performed on the sample to verify that the transition occurred at the proper frequency. The spectroscopy was performed in a THz time domain system similar to that shown in Figure 4.1. A photoconductive antenna was used in place of the ZnTe generation crystal, and the laser was a Ti:Sapph oscillator putting 300 mW average power on the antenna. The emitter was DC biased with 4 Volts, and the voltage on the sample was modulated as for the experiments in Chapter 2. This produced a signal that is only due to the modulation of the THz electric field waveform, which could than be Fourier transformed directly to the absorption.

6.2.1 New sample

As expected from calculations including the depolarization shift of the absorption, an absorption slightly above 1 THz was detected in the new sample design. The absorption is shown in Figure 6.3. The results showed a slightly shifting frequency for the transition as the D.C. electric field Stark shifted the transition energy. This shift reaches a minimum frequency at 0.1 V applied bias, where the transition also shows the narrowest linewidth, indicating this

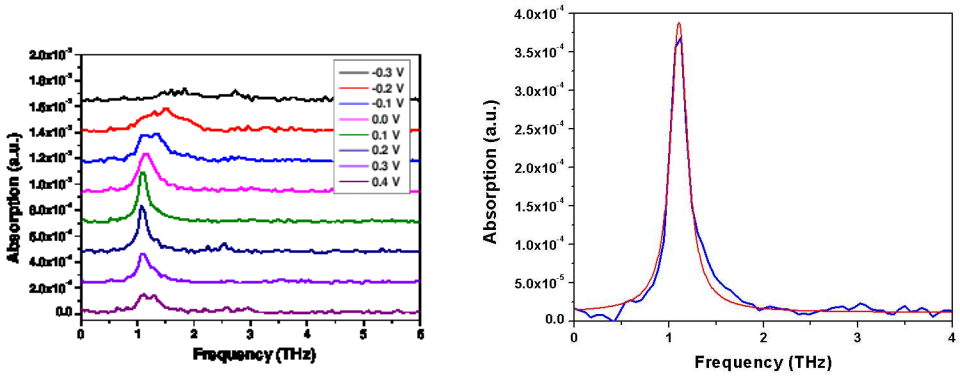

Figure 6.3: Waterfall plot of the absorption as a function of voltage for the new sample design (left). The absorption for 0.1 V, which showed the narrowest linewidth, is shown along with a Lorentzian fit. The half width-half max of this peak corresponds directly to Γ_2, which was 0.08 for this sample.

is the voltage where flatband conditions are achieved in the well. A Lorentzian fit of the absorption at 0.1 V shows a half-width half max corresponding to $\Gamma_2 = 0.08$, which should show bifurcations according to simulations.

6.2.2 B. Galdrikian Sample

Figure 6.4 shows the intersubband absorption from the sample design of B. Galdrikian. For the narrower well, the transition is shifted to higher frequencies as expected. Additionally, it seems to show a larger range of transition tunability than the new sample design, for reasons that are not clear. This is possibly because the signal to noise for this measurement was significantly

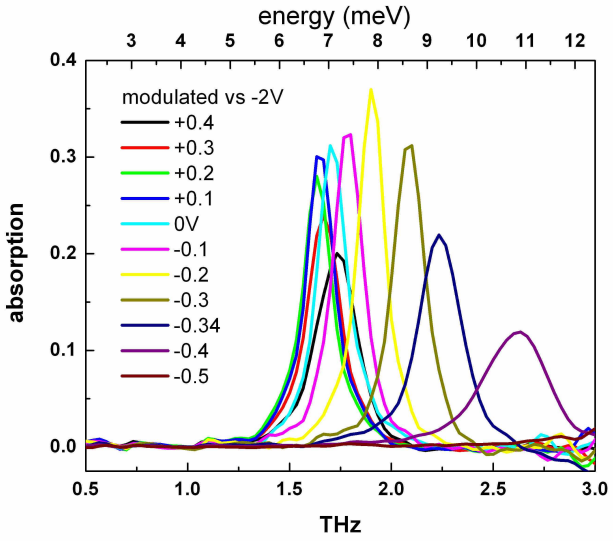

Figure 6.4: Absorption of the older sample design as a function of applied bias. Measurement performed by D. Stehr and collaborators at the HZDR in Dresden.

improved, and the shifted absorption for the new sample design was below the noise floor.

6.3 UCSB FEL Results

The experimental setup at the UCSB FEL is shown in Figure 6.5. The FEL is tuned to 84 cm^{-1} (2.5 THz), and sent through two polarizers, which can be variably cross-polarized to control the transmitted power of the FEL. The maximum power available at UCSB at the output port of the FEL was

$\sim$ 1 kW, and about 700 W at the input to the cryostat. The FEL was then focused by an off-axis parabolic mirror onto the sample, which was placed at a 45 degree angle in a helium-in-vapor cryostat. A silicon hemisphere was mechanically pressed on the back of the sample, and the FEL focused onto the silicon. The silicon allowed the FEL to achieve a smaller diffraction limited spot, increasing the electric field at a given power, which is necessary to achieve the required power densities for period doubling at UCSB. The light coming out of the sample, which should consist of the main laser line plus a small period doubled signal, was collected by another off-axis parabolic. This light was sent through two special QMC filters that attenuate 2.5 THz by a factor of 200 each, while passing 95% of the light at the period doubled frequency, 1.25 THz. This was designed to produce a total attenuation of $4x10^4$, which was enough filtration to prevent overload of the bolometer. The bolometer signal and pyro signal were recorded with an oscilloscope.

For the experiment at UCSB, the FEL was focused (in free space) to a spot of approximately 300 μm diameter. With this spot size, plus the additional focusing power of the Si lens, powers of a few hundred watts at the cryostat entrance could produce the required electric fields (details of the electric field calculations can be found in Appendix B). Two major difficulties presented

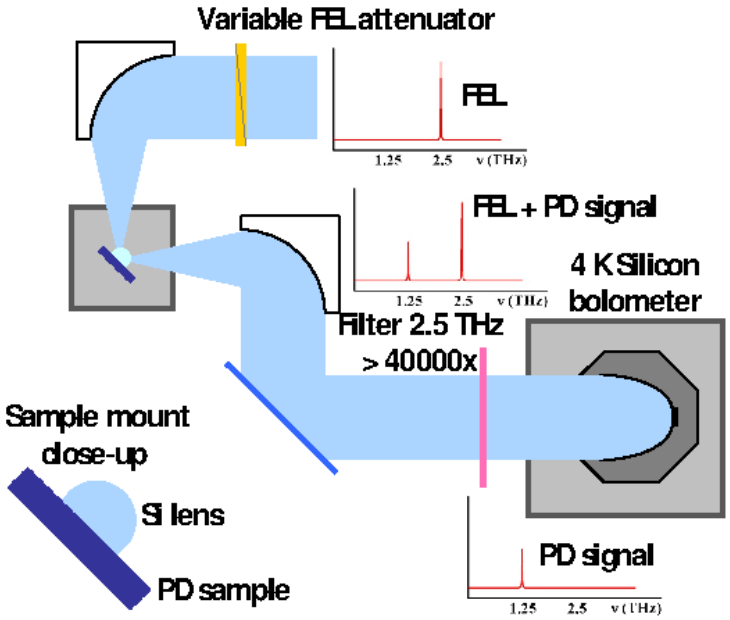

Figure 6.5: The experimental setup at UCSB. The experiment is done in reflection geometry, with a silicon lens to focus the FEL to a smaller diffraction limited spot, increasing the power density and associated electric field strength.

themselves for the UCSB experiment. The first was that the reflection geometry is difficult to align so that the focal spot occurs just at the active layer. A pinhole must be used in transmission to ensure that the focal spot is properly positioned each time the experiment is run. The second major difficulty performing the experiment at the UCSB FEL was the poor stability of the laser. Power fluctuations of 10% from pulse to pulse were typical, while over periods of 10 minutes the FEL would not stably lase. Several experimental days were spent searching for the period doubling signal, but the slow repetition rate (1 Hertz) and the power instability combined to give a low signal to noise, and no signal with the expected power dependence for period doubling was observed.

The main achievement of the FEL experiments at UCSB was to test the components of the system that would be used at the FEL in Dresden, which is far more stable and can achieve a larger power range. The QMC filters were tested, and it was verified that their specifications were accurate. Attenuation of each filter was slightly higher than the factor of 200 given; two filters combined gave a total of 50,000x attenuation, corresponding to $\sim$ 220x for each filter.

6.4 Dresden FEL Results

The FEL in Dresden produces much different pulses than the UCSB FEL. Each pulse is much shorter, on the order of 20 ps as compared to 1-3 μs at UCSB. This produces a pulse that is also less narrow in bandwidth, usually with a full width half max of approximately 2 μm. The repetition rate of the laser is 13 MHz, much higher than the 1 Hz repetition rate at UCSB. This results in much higher average powers, extending to the range of Watts, as opposed to the 1 mW average power at the UCSB FEL. A 13 MHz repetition rate means that the beam can be optically chopped, and lock-in detection can be used. This gives a huge advantage in signal to noise over the FEL at UCSB.

The experimental setup for the FEL at Dresden is similar to UCSB, but the geometry of the experiment is changed from reflection to transmission. Power levels at the UCSB FEL required that the Si lens be used to increase the focusing and thus the power density. At Dresden, peak powers of over 10 kW can be achieved, making the increased focusing unnecessary. The transmission mode experiment is easier to align, as the transmission signal can just be maximized. The FEL beam is passing through the sample, which is 2 mm thick, so the focus just needs to occur within that 2 mm rather than the complicated focus

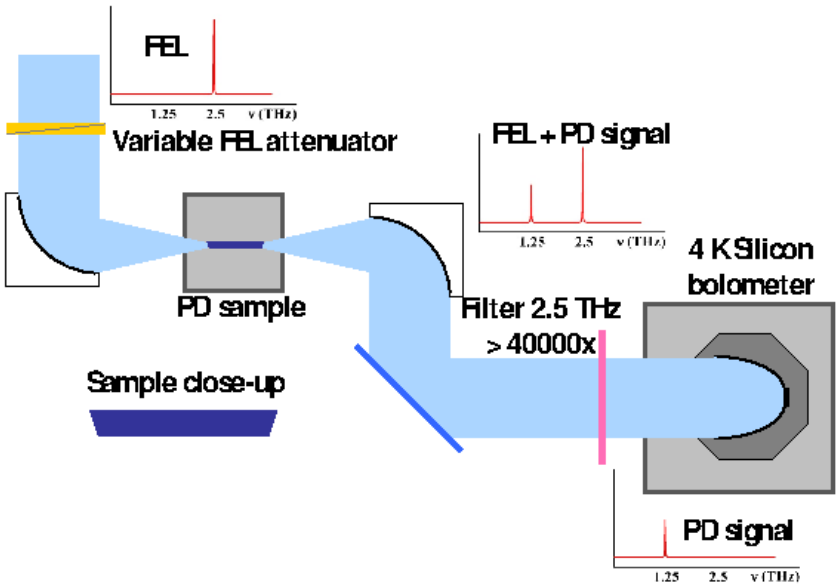

Figure 6.6: The experimental setup at Dresden. The setup is similar, except the higher powers of the Dresden FEL make it unnecessary to use the Si lens in the reflection geometry, so simpler transmission experiment is performed.

alignment necessary at UCSB.

The FEL is attenuated by calibrated attenuators in the beamline, and then focused by an off-axis parabolic mirror into the side facet of the sample. The facet is polished to a 15 degree angle, which has been shown to increase the coupling for previous experiments in this geometry. The transmitted signal is then collected by another off-axis, the 2.5 THz laser line is filtered out, and the signal is detected by a Si bolometer.

The beam size of the Dresden FEL is approximately 2 cm, which limits the

focal spot size, due to the reduced numerical aperture. The minimum spot size that was achieved was 500 μm, which is sufficiently tight focusing to achieve the required electric fields with the increased power levels available.

Modulation of the beam was achieved in two ways: mechanically with a chopper, and by voltage modulation of the sample as for the intersubband absorption experiments. Voltage modulation gave greatly increased signal to noise, and the results presented here are all for voltage modulated samples.

6.4.1 THz absorption

The first experiment that was performed was an absorption measurement. The FEL was run at 2.5 THz, and voltage dependent absorption of the 2.5 THz light was performed. Figures 6.3 and 6.4 show that both samples will absorb this frequency for certain voltage ranges.

The absorption for B. Galdrikian's sample (Figure 6.7) shows two distinct peaks. The peak at -0.3 V is present for all power levels. This peak corresponds to absorption from the lowest subband to the second subband. At 113 mW average FEL power, a second absorption peak appears at -0.6 V. Using the intersubband absorption data (Figure 6.4), one can see that the transition is

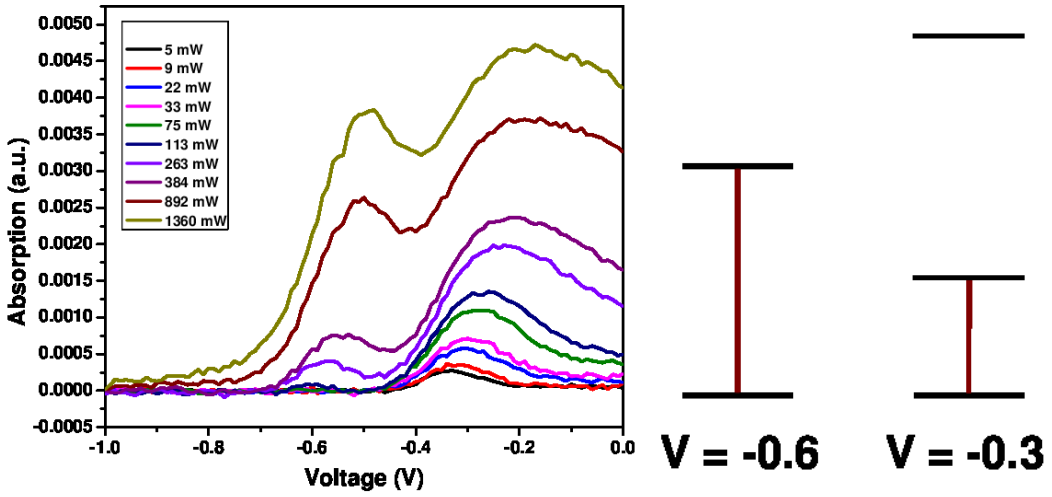

Figure 6.7: Absorption of the 2.5 THz FEL for B. Galdrikian's sample design, with the associated band energies and absorption mechanisms.

Stark shifted to high frequencies near 5 THz at this voltage. This means that the peak at -0.6 corresponds to a two-photon absorption process, still from the first to second subband.

In the new sample design, the absorption results were more complicated. As the voltage increases, the transition Stark shifts towards the minimum frequency of $\sim$ 1.1 THz near 0.1 V. Above this voltage, the transition Stark shifts to higher frequencies, although the intersubband absorption spectra are not high enough signal to noise to determine the full spectral absorption shift. The first peak that appears at -0.3 V appears to be associated with the Stark shifted absorption from the first to second well subbands. However, the second peak

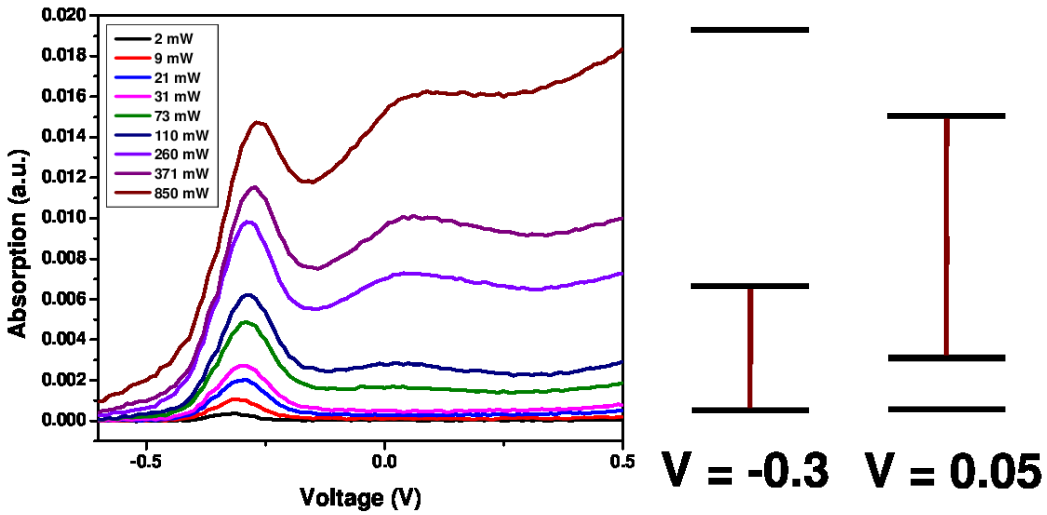

Figure 6.8: Absorption of 2.5 THz light for the new sample design, with the associated band energies and absorption mechanisms.

appearing at 0.05 V at 73 mW cannot be two photon absorption from the first to second subbands as in B. Galdrikian's sample, since the intersubband frequency is near 1.1 THz at this voltage. Instead the absorption must be a two-photon absorption from the second to third subbands, which calculations show are separated by 5 THz near flat band conditions. From Figure 6.1, it can be seen that the charge density at this voltage is approximately $1.5\text{x}10^{11}/\text{cm}^2$. In GaAs, the constant density of states gives $\sim 2.6\text{x}10^{10}/\text{cm}^2$ per meV, meaning that the Fermi level is 5.75 meV above the first subband, while the 1-2 subband energy spacing is only 4.2 meV. This means that the second subband has actually started to fill by this voltage, and a 2-3 subband two-photon absorption

matches the intersubband spacing and charge density.

6.4.2 THz Intersubband Emission

After the absorption measurements, the next step was to look for the period doubling emission, by putting in the QMC 60 cm^{-1}edge filters. A full range of powers were looked at for both samples, with high levels of averaging, but no signal indicating a period doubling bifurcation was observed.

For new sample design, the period doubling experiment was tried in several configurations. First, the voltage on the sample was modulated as before. Chopping the FEL was tried as well, but despite trying many powers and averaging extensively for both setups, no period doubling signal was observed. Additionally, the average power was reduced by covering 5/6 of the chopper holes, to reduce the average power on the sample and thereby reduce any possible detrimental effects due to heating, but again no period doubling signal was observed. The older sample design was probed similarly, but at 103 cm^{-1}, where period doubling is predicted to occur for this sample, also with null results.

While period doubling was not observed, an emission signal whose source is

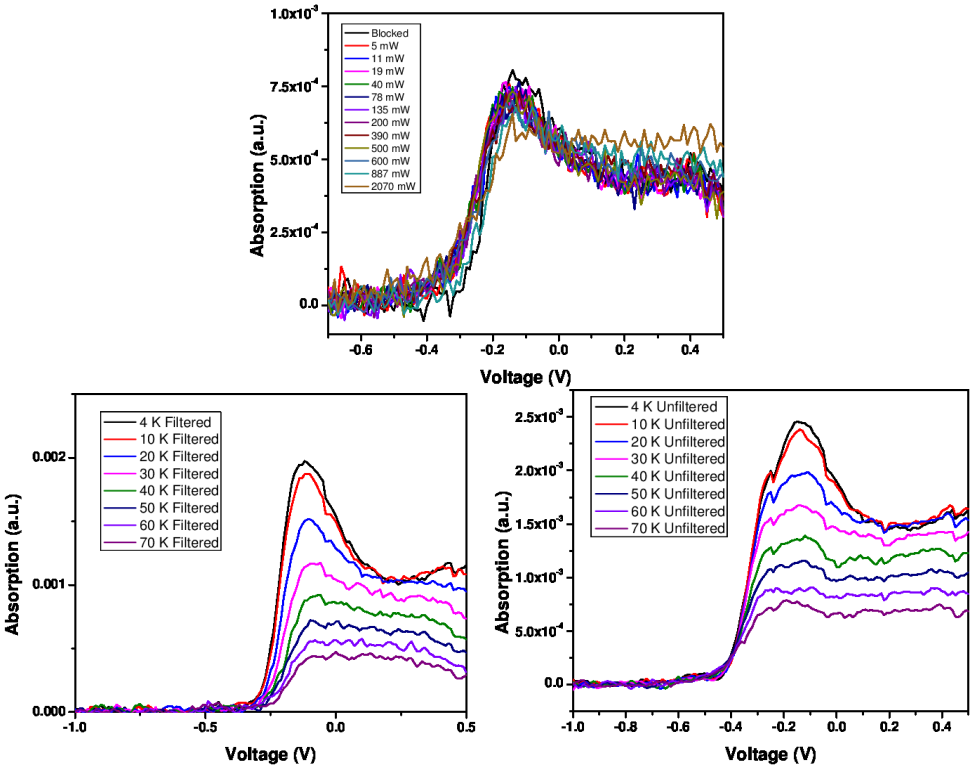

Figure 6.9: Emission with the FEL focused on the sample. (top) Temperature dependent emission of the new sample design, with and without the QMC 60 cm^{-1} filters, with the FEL blocked. (bottom) Small dips seen in the unfiltered spectra were due to slight miscalibrations of the AC voltage source, and occurred when the source was switching ranges. Conditions were optimized between the power dependent scans (top) and the temperature dependent scans (bottom), resulting in the greatly increased signal to noise.

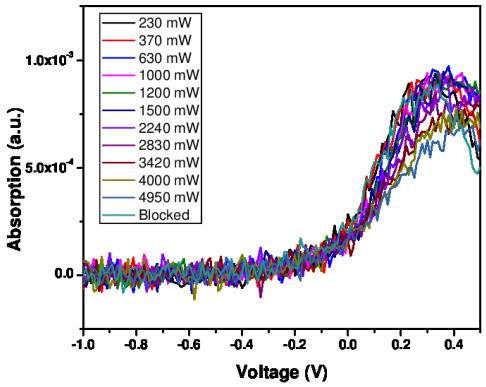

Figure 6.10: Emission of B. Galdrikian's sample as a function of the applied FEL power. The decreased emission for very high powers is most likely due to heating of the sample.

still unclear was observed, seen for the new and older sample designs in Figures 6.9 and 6.10, respectively. The first instinct was to associate this signal with period doubling, but as can be seen from the power dependence, the signal is present when the FEL is blocked as well. As the pump power of the FEL is increased, there is a change in the emission. To further investigate this effect, temperature dependent measurements of the emission were performed for the new sample design. Comparing the two spectra, the change in signal at higher powers seems to be associated with heating of the sample at high average FEL powers. Further discussion of the emission is found in Appendix C.

6.4.3 Discussion and future experiments

The period doubling experiments at Dresden show with reasonable certainty that period doubling emission is not present for either sample. The experiment is sensitive enough to observe emission signals in the sub-picowatt range. If the period doubled emission is below this signal level, it may not be possible to observe and distinguish it easily from the power-independent emission.

There are several possibilities that could explain why period doubling was not observed. First, of course, is that the theory incorrectly describes the system, and the effect does not actually exist. The depolarization effect that is responsible for the nonlinearity of the system is calculated as a perturbative effect, which may not be valid for such strong driving fields. As the population of a state is significantly altered by strong drive, it has been shown that the depolarization shift is significantly reduced. [28] This was shown in an experiment with a resonant drive field, however, and here the driving field is significantly off resonance from the transition. The calculations show that the population is changing less than $\sim 10\%$ because of the off resonant drive.

A second possibility is that the high average power is causing significant heating of the electrons. This would increase the dissipation in the system,

possibly bringing it to a regime where period doubling cannot occur. This is a difficult problem to overcome, as the repetition rate of the laser cannot be reduced. The only way to improve this would be to grow a sample with a narrower absorption linewidth so that heating does not bring the sample above the dissipation limits for observation of period doubling.

Another possibility is that subharmonic emission occurs, but domains form in the electron gas, each with its own phase. If the phases are randomly distributed, this would lead to deconstructive interference, leaving a reduced or completely canceled emission signal.

When the emission signal was not observed in the experiment in Dresden, we performed calculations that show that the period doubling effect can be observed in absorption as well. When the bifurcation occurs, the absorption increases in a step-like manner, and decreases again when the bifurcation is complete. This is logical, since the energy for the predicted subharmonic emission must come from the absorbed field. Formation of domains with different phase would not be a problem in the absorption, since the absorbed photon is seen a reduced signal at the detector no matter what phase of period doubling oscillation it produces. Additionally, the absorbed signal should always be larger than the emitted, since some dissipation of energy occurs between the

absorption and emission.

As mentioned above, the two-photon absorption present in the new sample design occurs at the same voltage where a period doubling bifurcation would occur. This two photon absorption would most likely dwarf any period doubled signal, and would certainly be indistinguishable from it. To eliminate this two-photon absorption and search for any period doubling related absorption present, the second subband must be unfilled. To do this, a sample with a working back gate, where flatband conditions can be reached at reduced charge density, is necessary.

Additionally, the absorption experiment should be carried out on B. Galdrikian's sample design, using 103 cm^{-1} as the pump frequency, where period doubling is expected to occur most robustly for this sample. This sample should not have a two-photon absorption at this frequency for flat band conditions, and may be the ideal candidate for a period doubling absorption. While the phenomenon of period doubling is still unobserved, future prospects for experiments to display the effect remain strong.

Bibliography

[1] John H. Davies. *The Physics of Low-Dimensional Semiconductors.* Cambridge University Press, 1998.

[2] M. Helm. *Intersubband physics in quantum wells: physics and device applications I.* Academic Press, 2000.

[3] S. J. Allen, D. C. Tsui, and B. Vinter. On the absorption of infrared radiation by electrons in semiconductor inversion layers. *Solid State Communications*, 20(4):425 – 428, 1976.

[4] R. C. Ashoori. Electrons in artificial atoms. *Nature*, 379:413, 1996.

[5] M. Fricke, A. Lorke, J. P. Kotthaus, G. Medeiros-Ribeiro, and P. M. Petroff. Shell structure and electron-electron interaction in self-assembled inas quantum dots. *EPL (Europhysics Letters)*, 36(3):197, 1996.

[6] R. J. Warburton, B. T. Miller, C. S. Dürr, C. Bödefeld, K. Karrai, J. P. Kotthaus, G. Medeiros-Ribeiro, P. M. Petroff, and S. Huant. Coulomb interactions in small charge-tunable quantum dots: A simple model. *Phys. Rev. B*, 58(24):16221–16231, Dec 1998.

[7] Pierre Petroff. Epitaxial growth and electronic structure of self-assembled quantum dots. In *Single Quantum Dots*, volume 90 of *Topics in Applied Physics*, pages 1–24. Springer Berlin / Heidelberg, 2003.

[8] F. Bras, P. Boucaud, S. Sauvage, G. Fishman, and J.-M. Gerard. Temperature dependence of intersublevel absorption in inas/gaas self-assembled quantum dots. *Applied Physics Letters*, 80(24):4620 –4622, jun 2002.

[9] B. A. Carpenter, E. A. Zibik, M. L. Sadowski, L. R. Wilson, D. M. Whittaker, J. W. Cockburn, M. S. Skolnick, M. Potemski, M. J. Steer, and M. Hopkinson. Intraband magnetospectroscopy of singly and doubly charged n-type self-assembled quantum dots. *Phys. Rev. B*, 74(16):161302, Oct 2006.

[10] H.J. Krenner, C. Pryor, J. He, J.P. Zhang, Y. Wu, C.M. Morris, M.S. Sherwin, and P.M. Petroff. Growth and optical properties of self-assembled

ingaas quantum posts. *Physica E: Low-dimensional Systems and Nanostructures*, 40(6):1785 – 1789, 2008. 13th International Conference on Modulated Semiconductor Structures.

[11] Hubert J. Krenner, Craig E. Pryor, Jun He, and Pierre M. Petroff. A semiconductor exciton memory cell based on a single quantum nanostructure. *Nano Letters*, 8(6):1750–1755, 2008. PMID: 18500845.

[12] E. A. Zibik, T. Grange, B. A. Carpenter, N. E. Porter, R. Ferreira, G. Bastard, D. Stehr, S. Winnerl, M. Helm, H. Y. Liu, M. S. Skolnick, and L. R. Wilson. Long lifetimes of quantum-dot intersublevel transitions in the terahertz range. *Nature Materials*, 8:803, 2009.

[13] J. He, R. Nötzel, P. Offermans, P. M. Koenraad, Q. Gong, G. J. Hamhuis, T. J. Eijkemans, and J. H. Wolter. Formation of columnar (in,ga)as quantum dots on gaas(100). *Applied Physics Letters*, 85(14):2771–2773, 2004.

[14] J. He, H. J. Krenner, C. Pryor, J. P. Zhang, Y. Wu, D. G. Allen, C. M. Morris, M. S. Sherwin, and P. M. Petroff. Growth, structural, and optical properties of self-assembled (in,ga)as quantum posts on gaas. *Nano Letters*, 7(3):802–806, 2007.

[15] Hubert J. Krenner and Pierre M. Petroff. Quantum posts with tailored structural, electronic and optical properties for optoelectronic and quantum electronic device applications. *Solid State Communications*, 149(35-36):1386 – 1394, 2009. Fundamental Phenomena and Applications of Quantum Dots.

[16] Stefan Volk, Florian J. R. Schullein, Florian Knall, Dirk Reuter, Andreas D. Wieck, Tuan A. Truong, Hyochul Kim, Pierre M. Petroff, Achim Wixforth, and Hubert J. Krenner. Enhanced sequential carrier capture into individual quantum dots and quantum posts controlled by surface acoustic waves. *Nano Letters*, 10(9):3399–3407, 2010.

[17] Christopher M. Morris, Dominik Stehr, Hyochul Kim, Tuan-Anh Truong, Craig Pryor, Pierre M. Petroff, and Mark S. Sherwin. Terahertz ionization of highly charged quantum posts in a perforated electron gas. *Nano Letters*, Articles ASAP(0), 2011.

[18] H. Sakaki, G. Yusa, T. Someya, Y. Ohno, T. Noda, H. Akiyama, Y. Kadoya, and H. Noge. Transport properties of two-dimensional electron gas in algaas/gaas selectively doped heterojunctions with embedded inas quantum dots. *Applied Physics Letters*, 67(23):3444–3446, 1995.

[19] E. Ribeiro, E. Müller, T. Heinzel, H. Auderset, K. Ensslin, G. Medeiros-Ribeiro, and P. M. Petroff. Inas self-assembled quantum dots as controllable scattering centers near a two-dimensional electron gas. *Phys. Rev. B*, 58(3):1506–1511, Jul 1998.

[20] B. T. Miller, W. Hansen, S. Manus, R. J. Luyken, A. Lorke, J. P. Kotthaus, S. Huant, G. Medeiros-Ribeiro, and P. M. Petroff. Few-electron ground states of charge-tunable self-assembled quantum dots. *Phys. Rev. B*, 56(11):6764–6769, Sep 1997.

[21] G. Medeiros-Ribeiro, D. Leonard, and P. M. Petroff. Electron and hole energy levels in inas self-assembled quantum dots. *Applied Physics Letters*, 66(14):1767–1769, 1995.

[22] Craig E. Pryor. Calculations of quantum posts.

[23] G. Medeiros-Ribeiro, F. G. Pikus, P. M. Petroff, and A. L. Efros. Single-electron charging and coulomb interaction in inas self-assembled quantum dot arrays. *Phys. Rev. B*, 55(3):1568–1573, Jan 1997.

[24] Gregory Snider. 1-d poisson solver.

[25] D. Stehr, C. M. Morris, D. Talbayev, M. Wagner, H. C. Kim, A. J. Taylor,

H. Schneider, P. M. Petroff, and M. S. Sherwin. Ultrafast carrier capture in ingaas quantum posts. *Applied Physics Letters*, 95(25):251105, 2009.

[26] Tsuneya Ando, Alan B. Fowler, and Frank Stern. Electronic properties of two-dimensional systems. *Rev. Mod. Phys.*, 54(2):437–672, Apr 1982.

[27] B. Galdrikian. *Nonlinear and nonperturbative dynamics in quantum wells.* PhD thesis, UCSB, 1994.

[28] K. Craig, B. Galdrikian, J. N. Heyman, A. G. Markelz, J. B. Williams, M. S. Sherwin, K. Campman, P. F. Hopkins, and A. C. Gossard. Undressing a collective intersubband excitation in a quantum well. *Phys. Rev. Lett.*, 76(13):2382–2385, Mar 1996.

[29] Craig Pryor. Eight-band calculations of strained inas/gaas quantum dots compared with one-, four-, and six-band approximations. *Phys. Rev. B*, 57(12):7190–7195, Mar 1998.

[30] Craig Pryor. Geometry and material parameter dependence of inas/gaas quantum dot electronic structure. *Phys. Rev. B*, 60(4):2869–2874, Jul 1999.

[31] I. Vurgaftman, J. R. Meyer, and L. R. Ram-Mohan. Band parameters

for iii-v compound semiconductors and their alloys. *Journal of Applied Physics*, 89(11):5815–5875, 2001.

[32] I. R. Sellers, D. J. Mowbray, T. J. Badcock, J.-P. R. Wells, P. J. Phillips, D. A. Carder, H. Y. Liu, K. M. Groom, and M. Hopkinson. Infrared modulated interlevel spectroscopy of 1.3??m self-assembled quantum dot lasers using a free electron laser. *Applied Physics Letters*, 88(8):081108, 2006.

[33] Eui-Tae Kim, Anupam Madhukar, Zhengmao Ye, and Joe C. Campbell. High detectivity inas quantum dot infrared photodetectors. *Applied Physics Letters*, 84(17):3277–3279, 2004.

[34] K. Kern, D. Heitmann, P. Grambow, Y. H. Zhang, and K. Ploog. Collective excitations in antidots. *Phys. Rev. Lett.*, 66(12):1618–1621, Mar 1991.

[35] M. Hochgräfe, R. Krahne, Ch. Heyn, and D. Heitmann. Anticyclotron motion in antidot arrays. *Phys. Rev. B*, 60(15):10680–10682, Oct 1999.

[36] Jerome Faist, Federico Capasso, Deborah L. Sivco, Carlo Sirtori, Al-

bert L. Hutchinson, and Alfred Y. Cho. Quantum cascade laser. *Science*, 264(5158):553–556, 1994.

[37] M. Helm, E. Colas, P. England, F. DeRosa, and S. J. Allen. Observation of grating?induced intersubband emission from gaas/algaas superlattices. *Applied Physics Letters*, 53(18):1714–1716, 1988.

[38] Rudeger Kohler, Alessandro Tredicucci, Fabio Beltram, Harvey E. Beere, Edmund H. Linfield, A. Giles Davies, David A. Ritchie, Rita C. Iotti, and Fausto Rossi. Terahertz semiconductor-heterostructure laser. *Nature*, 417(6885):156–159, May 2002.

[39] B. S. Williams. Terahertz quantum-cascade lasers. *Nature Photonics*, 1:517–525, 2007.

[40] A. Wade, G. Federov, D. Smirnov, S. Kumar, B.S. Williams, Q. Hu, and J. L. Reno. Magnetic-field-assisted terahertz quantum cascade laser operating up to 225 k. *Nature Photonics*, 3:41–45, 2008.

[41] M. Sugawara, K. Mukai, Y. Nakata, K. Otsubo, and H. Ishilkawa. Performance and physics of quantum-dot lasers with self-assembled columnar-

shaped and 1.3- mu;m emitting ingaas quantum dots. *Selected Topics in Quantum Electronics, IEEE Journal of*, 6(3):462 –474, may/jun 2000.

[42] Hyochul Kim, Matthew T. Rakher, Dirk Bouwmeester, and Pierre M. Petroff. Electrically pumped quantum post vertical cavity surface emitting lasers. *Applied Physics Letters*, 94(13):131104, 2009.

[43] Charles A. Schmuttenmaer. Exploring dynamics in the far-infrared with terahertz spectroscopy. *Chemical Reviews*, 104(4):1759–1780, 2004. PMID: 15080711.

[44] Matthew C. Beard, Gordon M. Turner, and Charles A. Schmuttenmaer. Transient photoconductivity in gaas as measured by time-resolved terahertz spectroscopy. *Phys. Rev. B*, 62(23):15764–15777, Dec 2000.

[45] D. G. Cooke, F. A. Hegmann, Yu. I. Mazur, Zh. M. Wang, W. Black, H. Wen, G. J. Salamo, T. D. Mishima, G. D. Lian, and M. B. Johnson. Ultrafast carrier capture dynamics in ingaas/gaas quantum wires. 103(2):023710, 2008.

[46] D. Turchinovich, K. Pierz, and P. Uhd Jepsen. Inas/gaas quantum dots as

efficient free carrier deep traps. *physica status solidi (c)*, 0(5):1556–1559, 2003.

[47] A. A. Batista, B. Birnir, and M. S. Sherwin. Subharmonic generation in a driven asymmetric quantum well. *Phys. Rev. B*, 61(22):15108–15113, Jun 2000.

[48] Adriano A. Batista, P. I. Tamborenea, Bjorn Birnir, Mark S. Sherwin, and D. S. Citrin. Nonlinear dynamics in far-infrared driven quantum-well intersubband transitions. *Phys. Rev. B*, 66(19):195325, Nov 2002.

[49] Adriano A. Batista, Bjorn Birnir, P. I. Tamborenea, and D. S. Citrin. Period-doubling and hopf bifurcations in far-infrared driven quantum well intersubband transitions. *Phys. Rev. B*, 68(3):035307, Jul 2003.

[50] Karl Blum. *Density Matrix Theory and Applications*. Plenum Press, 1981.

[51] J. B. Williams, K. Craig, M. S. Sherwin, K. Campman, and A. C. Gossard. Measurements of far-infrared intersubband absorption linewidths in gaas/algaas quantum wells as a function of temperature and charge density. *Physica E: Low-dimensional Systems and Nanostructures*, 2(1-4):177 – 180, 1998.

[52] J. W. Williams. *Dissaption of THz frequency intersubband plasmons in quantum wells*. PhD thesis, UCSB, 2000.

Appendix A

Processing Details

The processing for the resonant photocurrent experiment and the period doubling experiment are similar for many steps. Two different processes were used with AZ 5214E resist, both of which worked for the general processing steps. The anneal for a two layer structure in the period doubling sample was never perfected. The process used for the period doubling samples is preferable for lithography, as it caused fewer problems during liftoff.

Quantum Post FTIR Samples

1. Cleave sample to 1 cm x 2.5 mm. Clean with acetone, isopropanol, 3 minutes in sonicator at low power levels (3/10).

2. Spin on AZ5214E photoresist at 6000 rpm for 30 seconds. Solvent bake

at 115 C for 60 seconds.

3. Cover 1/3 of sample with aluminum foil shield. Flood expose for 5 minutes.

4. Develop with AZ 400K 1:4 for 60 seconds. Further development time can be used to get rid of any remaining photoresist around the edges of the sample. However, leaving a small edge bead was sometimes benificial. Covering the sample from edge to edge with aluminum sometimes caused the sample to be leaky under reverese bias.

5. To avoid aluminum covering the side facet and causing a short between the back gate n-doped layer and the Schottky aluminum front contact, the sample must be glued to a mount during evaporation. A glass slide was used during the processing of the QP FTIR samples. AZ 5214E was used to glue the sample to the glass slide, then the same resist was used to cover the side walls carefully, being sure not to cover the to surface. Then the glass slide and glued sample were heated for 60 minutes at 90 C to evaporate the solvents from the resist.

6. Evaporation: 2000-3000 Angstroms of aluminum by e-beam evaporation.

The evaporator should be pumped to 2e-6 torr before beginning.

7. Liftoff: The long bake to glue the sample down hardens the resist. A longer than normal liftoff is needed usually. The sample should be soaked in acetone for 1 hour or more. Any remaining photoresist after this can be brushed off gently with a small paintbrush.

8. Solvent clean as in step 1.

9. Indium: Make two small scratches in the 1/3 of the sample uncovered by aluminum. Small pieces of indium are then mechanically pressed into these scratches. Heat the sample for 60 seconds at 410 C in the strip annealer to make the contacts.

Resonant Photocurrent Experiment Samples

1. Cleave approximately 1 cm x 1 cm sample. Clean with acetone, isopropanol, 3 minutes in sonicator at low power levels (3/10).

2. Spin on AZ 5214 photoresist at 6000 rpm for 30 seconds. Solvent bake at 115 C for 60 seconds.

3. Mesa level lithography. The mask created requires image reversal for this step. Expose for 25 seconds. Bake at 115 C for 60 seconds to image reverse. Next is a 60 second flood exposure. This is then developed for 50 seconds in AZ 400K 1:4 developer.

4. The etch comes next. The etch used is 1:8:160 $H_2SO_4 : H_2O_2 : H_2O$. Mix for 30 seconds. This should produce an etch rate of approximately 5 Angstroms/second. However, the etch rate is variable, and can be up to 8 Angstroms/second if the mixing ratios are a little off, so it is best to etch in several smaller steps. The Dektak is used to monitor the etch for the correct depth.

5. Rinse the photoresist with acetone, isopropanol, and water.

6. Next, the lithography for the contacts is performed. The top and bottom contacts are both ohmic contacts. This is the same image reversal lithography performed in step 3.

7. The deposition of the top contacts is: 150/300/150/2000 of Ge/Au/Ni/Au. This is then annealed in the rapid thermal annealer for 45 seconds at 430 C.

Period Doubling Processing

The processing for this sample never fully worked. It was discovered after the trip to Dresden that the calibration for the rapid thermal annealer was significantly off, which meant all the samples were annealed at a temperature that was far too high. This caused a short between the back contact quantum well and the active region quantum well. The processing for this sample is exactly as detailed in Jon Williams's thesis, with a few differences.

1. Image reversal lithography: AZ5214E resist. Spin on at 6000 rpm for 30 seconds. Bake for 60 seconds at 95 C to get out the solvents. 5 seconds initial exposure. Image reversal bake for 60 seconds at 110 C. Flood expose for 60 seconds. Develop in AZ MIF 300.

2. Etch: 1:8:160 $H_2SO_4 : H_2O_2 : H_2O$ as in the section for the resonant photocurrent experiment. First, an etch is done on the region for the contacts for the quantum well and the back gate, 100 nm. Then an additional 640 nm is etch towards the quantum well back gate. It may be necessary to etch closer to the contacts than 100 nm.

3. The anneal is still not worked out. The best advice is to slowly increase

the temperature of the anneal, with constant time. I have tried 30 second anneals, starting at 370 C. After each anneal at constant temperature, check the resistance. It will hopefully be in the kilo-ohm level, with the resistance between the quantum well and back gate contact being larger.

Appendix B

Period Doubling Electric Field Calculations

We start with the Poynting vector,

$$\mathbf{S} = \mathbf{E} \times \mathbf{H} \tag{B.1}$$

In the materials here, $\mu_r = 1$, so the $\mathbf{H}$ field is just $\mathbf{H} = \mathbf{B}/\mu_0$, and the Poynting vector is:

$$\mathbf{S} = \mathbf{E} \times \mathbf{B}/\mu_0 \tag{B.2}$$

We assume a plane wave form for the electric field waves, given by:

$$\mathbf{E} = \mathrm{E}_0 \cos\left(\mathrm{kz} - \omega \mathrm{t}\right) \hat{\mathbf{x}} \tag{B.3}$$

$$\mathbf{B} = \mathrm{B}_0 \cos\left(\mathrm{kz} - \omega \mathrm{t}\right) \hat{\mathbf{y}} \tag{B.4}$$

For plane waves, using Maxwell's equations gives us the constant B_0 in terms of the electric field E_0

$$\nabla \times \mathbf{E} = -\frac{\partial \mathbf{B}}{\partial \mathrm{t}} \rightarrow \mathrm{B}_0 = \mathrm{E}_0 \mathrm{k}/\omega = \mathrm{E}_0 \mathrm{n}/\mathrm{c} \tag{B.5}$$

To determine the average power, we can average over a period of the wave, getting:

$$|\langle \mathbf{S} \rangle| = \frac{\mathrm{E}_0^2 \mathrm{n}}{\mu_0 \mathrm{c}} \left\langle \cos^2\left(\mathrm{kz} - \omega \mathrm{t}\right) \right\rangle = \frac{E_0^2 n}{2\mu_0 c} = P/A \tag{B.6}$$

The electric field for a given power and spot size can then be calculated:

$$P/A = \frac{E_0^2 c}{2\mu_0 n} \rightarrow E_0 = \sqrt{\frac{2\mu_0 c}{n}\frac{P}{A}} = \sqrt{\frac{2\mu_0 \epsilon_0 c}{\epsilon_0 n}\frac{P}{A}} = \sqrt{\frac{2}{\epsilon_0 c n}\frac{P}{A}} \tag{B.7}$$

Appendix C

Period Doubling Emission Analysis

Polarization tests showed that the emission is polarized along the growth direction, as would be expected for an emission associated with an intersubband transition. However, these measurements are taken with a square wave pulse, so essentially the emission occurs at a constant voltage. In this situation, it is not clear where the energy for such an emission would come from. Several tests were performed by DC biasing the sample and placing an optical chopper in various locations in the beam path. When the chopper is placed between the sample and the bolometer, a large DC signal is observed, as well as the emission. The DC signal most likely comes from the difference in black body emission from the 300 K chopper blades and 4 K sample. The fact that the emission is there in this geometry seems to suggest that the observed signal is really an emission from the sample, and not merely the modulation of black

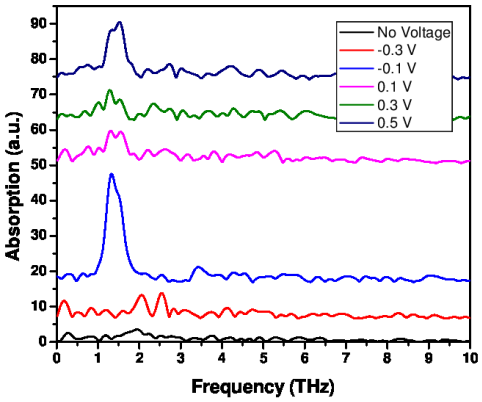

Figure C.1: Emission spectra for the new sample design, taken using an FTIR without the 60 cm^{-1} filters.

body radiation passing through the sample. As another check on this, the chopper blade was placed at the entrance to the cryostat, and no signal was observed.

The emission from the new sample design was investigated spectrally using an FTIR, with the emission spectra shown in Figure C.1. Due to the low signal level of the emission, obtaining spectra with good signal to noise was difficult. However, the spectra seem to at least indicate that the emission is somehow associated with the intersubband transition, as the linewidth is narrow. Further investigation of this effect would be necessary to speculate on the origin of the emission signal.

However, while the source of the signal is unclear, observation of the emis-

sion, but not the period doubling signal means that a limit can be set on the strength of period doubling emission. At the level of averaging and signal to noise present when the power dependent scans were taken, any period doubling signal would need to be less than the noise level, approximately 1x10^{-4} V signal on the lock-in. To establish a power level, this signal must first be backed out of the lock-in, which gives the RMS voltage, and assumes a sine wave instead of the square wave that is being used for modulation. This gives us a real noise level of 1.1x10^{-4} V. Given the bolometer response of 2.4x10^{5} V/W and factoring in the gain setting of 1000, the power corresponding to 1.1x10^{-4} V is = 1.1x10^{-4} W/2.4x10^{8} V/W = 4.6x10^{-13} W. Any signal at the level of 0.46 pW or greater should be observable in the experiment.

Appendix D

Resonant Photocurrent Data Analysis

The data shown in Figure D.1 has been modified from the raw data to allow for proper comparison between the horizontal and vertical polarizations. Our ability to control the power on the samples is limited by the attenuation scheme and the pulse to pulse power fluctuations of the Free Electron Laser. Lack of control over the THz power makes it very difficult to apply the exact same amount of power at the two separate polarizations. Slight differences in the power lead to differences in the photocurrent from separate polarizations of THz light, particularly at high voltages, as can be seen in Figure D.1a.

We believe that the large photocurrents at high voltages are caused by heating of the carriers from the THz beam, an effect which should be polarization independent and should be of equal magnitude for both polarizations if driven

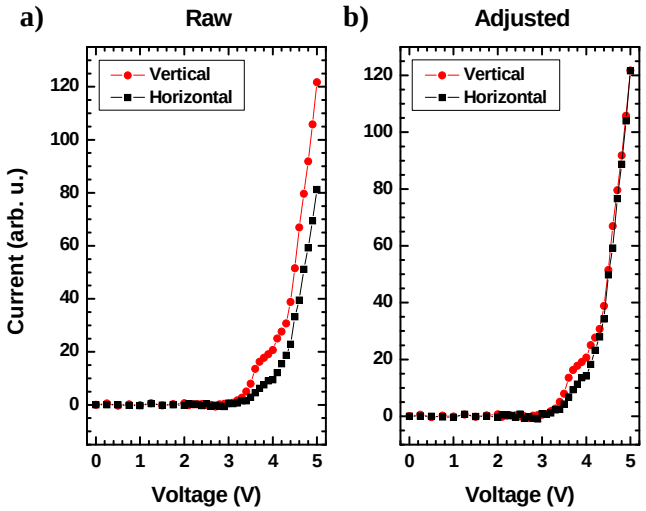

Figure D.1: Calibration of the vertical and horizontal photocurrent for the intersubband response. The photocurrent at large voltages is assumed to be due to heating and is matched, thereby taking into account any difference in coupling of the two polarizations into the sample.

at equal power. Figure D.2 shows the photocurrent response as a function of voltage which is applied only across the back gate (no current through the quantum well or post structure). There are no quantum transitions to interact with in this system and any signal which is seen is attributed to heating effects. We find that the heating response from both polarizations is equal and that the magnitude of the photocurrent in the back contact is consistent with the magnitude of photocurrent seen at high voltages in the quantum well and post samples. This is a strong indication that the photocurrents seen at high voltage ($>$4 V) are induced by heating.

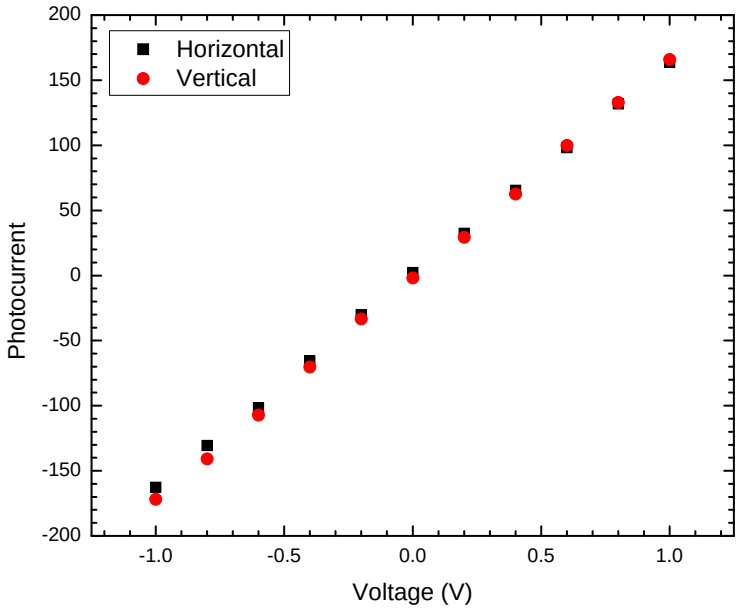

Figure D.2: Heating of the contacts induces photocurrent. This measurement was taken applying the FEL in the space between two back contact pads, thus heating the electrons and causing the photocurrent.

Under the assumption that the majority of the photocurrent at high voltage is induced by heating, these photocurrents are indicative of the power incident on the system and can be used to normalize the measured curves. We expect that the response from equal applied THz powers at separate polarizations should be the same in this high voltage regime and scale our data accordingly. The curve shown in Figure D.1b is produced by adjusting all of the data at one polarization by a scaling factor such that the high voltage photocurrent response is the same for both polarizations. If the difference between the two polarizations is integrated to show the response associated with the quantum transitions, as is done for the "intersubband response" in Figure 3.13, any offset at high voltages must be eliminated in order to normalize the powers incident on the systems. For this reason, the integrated difference between polarizations is performed on the adjusted data as opposed to the raw data in order to create the "intersubband response" plot.

Appendix E

Period Doubling C Code

Several versions of the code were written, to perform different tasks associated with the period doubling simulations. However, they all have the same code running as a backbone, only implementing it slightly differently depending on if the goal was to create single bifurcation diagrams or simulate large sets of wells. For each implementation, there is a separate folder, and the main project file is called PD_Well. Dev C++ was used as the compiler, available free online.

The part of the code that solves the well energy structure and states was written by Brian Galdrikian. They were originally written for Mac, and the code initializing most variables was contained in the Mac specific section of the code. I added initializations for the variables I wanted to use.

Files

integrator.cpp Integrates the period doubling equations, the top level.

integrator.h Holds the functions that actually define the differential equation, and the Runge-Kutta integrator.

main_run.cpp The code that actually decides which wells to run and what to output. This is the top level of the project code.

param_reader.cpp Reads in parameters from a file set up to provide the inputs necessary for the quantum well solver. Most of these variables are now entered in quantum_well_new.h.

quantum_well_functions.h Function declarations.

quantum_well_new.h Defines constants, programming simplifications, and some functions.

solve.cpp The main code responsible for solving the well. Brian Galdrikian is responsible for most of this code.

solve_functions.cpp Contains the functions necessary to solve for the wavefunctions and energies of the well.

support_functions.cpp A few more equations that support solve.cpp

TDEVAL.cpp Matrix manipulations for solving the well.

TINVIT.cpp Matrix manipulations for solving the well.

well_creator.cpp Creates a well with the specified width, step height, step width, etc, to be used in solve.cpp.

Futher File Explanations

integrator.cpp

This file contains the top level of the period doubling differential equation solver. The only function is lam_bif. This function sets up the proper constants and arrays for the integration. Time and electric field vectors are defined. The electric fields are converted to the original λ used in B. Galdrikian's period doubling paper. At each time step, the $trace\,(\rho z)$ is calculated. oderk5pdeff is called to actually compute the value of the differential equations at the next time step. The time vector is defined by the number of cycles and the resolution desired within those cycles. The actual sampling to determine if a bifurcation

has occured does not start until cycle_sample_start. The variables related to the timing are defined in quantum_well_new.h.

integrator.h

frhs() defines the differential equations to be solved. There are three differential equations, to account for the fact that ρ_{10} is imaginary. The constants passed in the array c[] are defined in main_run.cpp.

rho_intialize() finds the thermal equilibrium charge densities in the ground and excited states. Details can be found in Brian Galdrikian's PhD thesis.

oderk5pdeff() is the Runge-Kutta solver for the differential equations. This code is adapted from Numerical Recipes in C++. The constants are defined in quantum_well_new.h, and are also from Numerical Recipes.

The older version of this function was designed to reduce the number of multiplications necessary, but did not seem to increase the speed of calculations, so was not used.

main_run.cpp

This is the top level code that actually takes care of opening files, calling the functions that do the calculations, and defining some of the constants that are specific to a calculation for a well. The main execution of the program occurs on three lines. First, well_creator() is called to create the well specified by the constants above. Solve() is called to produce the energies and wavefunctions for the given well parameters. Finally, lam_bif is called to solve the well and determine the bifurcating electric field.

param_reader.cpp

This is largely unused now, but a few of the variables are still grabbed from it. It reads the parameters that are required for Brian Galdrikian's well solver, assigning them to the proper variable names.

dz_Angs The spacing for grid points in the well, in Angstroms. Currently, this must always be 1 Angstrom.

T The temperature, in Kelvin.

mass_ratio The effective mass of the electron in the material being used.

kappa The dielectric constant of the material being worked with.

bnum The number of points in the input grid for the well.

ns Number of states to be used in the well.

omegaI For the susceptibility calculation, the lower frequency limit. This does not work in the current version of the code.

omegaF Higer frequency limit for the same.

Ga1 gamma 1 in the period doubling calculation.

Ga2 gamma 2 in the period doubling calculation.

quantum_well_new.h

The main space for defining constants used by many different sections of the code.

struct parameters holds most of the variables used by solve that the user can input.

After this many different parameters and notations used in the solve code are entered. Most of the numbering is done from 1 to N in the solve code instead of 0 to N-1, by using the replacements defined here.

Finally, constants used throughout the program are defined.

solve.cpp

This is the main code that solves for the states of the well and the associated energies. Old code associated with the Mac version is usually still there, but commented out. Many of the variables are defined close to the top. The spacing required for this calculation is 1 Angstrom. This can be changed, but it is assumed throughout the program, and changing it could involve chasing down all the places where 1 Anstrom spacing is assumed.

solve_functions.cpp

This defines the working of the functions that do most of the work solving for the potential energy and wavefuctions/energies for the well. These were all written by Brian Galdrikian, and have been proven to work. It is not recommended that they be modified without a thorough understanding of their workings.

support_functions.cpp

A few support functions, these do background work for the algorithms in solve.cpp.

TDEVAL.cpp and TINVIT.cpp These are both matrix manipulation functions, optimized for dealing with matrices quickly in the solution of the well and its states. These should not be altered.

well_creator.cpp

This sets up the well that will be solved, based on the basic inputs. w is the width of the well in Anstroms, barrier_height is the height in meV of the barriers that define the sides of the total well (here around 230 meV for 30% AlGaAs), step_w is the width in Angstroms of the asymmetric step, step_pos is the position of the left side of the barrier from the left side of the well in Angstroms (not the center of the barrier), step_h is the height in meV of the asymmetric barrier in the well, nz is the number of points in the grid (needs to be larger than the width of the well in Angstroms by a decent amount, potential is the array that will hold the created potential energy of the well, and well_edge_index and well_center_index are the positions of the edge of

the well and center. These last two are integers, which is part of the structure set up based on the fact that 1 Angstrom is the only size spacing that works for this well.